# ANALYSIS AND DESIGN OF DIELECTRIC-LENS ANTENNAS AND PLANAR MULTIPLIER CIRCUITS FOR MILLIMETER-WAVE APPLICATIONS

by

Daniel F. Filipovic

# ANALYSIS AND DESIGN OF DIELECTRIC-LENS ANTENNAS AND PLANAR MULTIPLIER CIRCUITS FOR MILLIMETER-WAVE APPLICATIONS

by

Daniel F. Filipovic

A dissertation submitted in partial fulfillment
of the requirements for the degree of
Doctor of Philosophy
(Electrical Engineering)
in The University of Michigan
1995

Doctoral Committee:

Associate Professor Gabriel M. Rebeiz, Chairperson
Professor Fawwaz T. Ulaby
Associate Professor Kim A. Winick
Research Scientist Jack R. East

To my family

# ACKNOWLEDGEMENTS

I would like to thank my advisor Professor Gabriel Rebeiz, who provided me with the opportunity to do this research. Over the years he has provided much guidance, and an open ear to listen to whatever crazy ideas I might think of. I also want to thank each member of my committee for their comments and suggestions, and their willingness to be on my commitee on such short notice.

I would like to thank Phil Marsh, Dr. Brian Kormanyos, and Sanjay Raman, for their friendship and support this past year. Phil is one of the most sincere people I have ever met, and well as one of the most intelligent. Whenever I encountered a technical problem in the cleanroom, he would always seem to know the solution, and would also be willing to share it. I will miss our long lunches in which we brainstormed our way through revelations in philosophy, politics, and of course, engineering. I would like to thank Brian for his friendship, particularly during my summer at Hughes. I hope his honesty and aptitude create great success for him in the future. I would like to thank Sanjay for his friendship this past year. I hope his remaining time in graduate school is fruitful, and he attains the career opportunities that he wants afterwards. I would also like to thank Dr. George Eleftheriades for his friendship and support in my early years of graduate school. In addition, George always amazed me with his deep theoretical insights. I have also enjoyed working with Dr. Chen-Yu Chi, Gildas Gauthier, Gerald Haennig, Dr. Tom Budka, Dr. Steve Gearhart, Alain Courtay, and Steve Robertson.

I would like to thank Dr. Walid Ali-Ahmad for fabricating the terahertz reflector, and Dr. Steve Gearhart for introducing me to fabrication, and walking me through the double-slot fabrication. I would like to thank Bob Brunner for giving me the opportunity of an internship at Hughes during my graduate studies, and making the active multiplier possible. Special thanks goes to Dr. Richard Bradley, who fabricated the fixtures required for the MMIC project, and contributed a significant amount of his personal time for the measurement of the multiplier chips. Although we didn't quite meet our goals, I hope I have introduced a methodology which in future iterations will produce great success. I also wish to acknowledge the generous financial support I have received during my entire graduate studies from the *NASA-Center for Space Terahertz Technology.*

The friendship of Heidi Sponseller, Tom Gyarmati, Wayne Adam, and Ted Allen are much appreciated and were vital to my well-being during graduate school. I will miss all the things we did during my stay at Cambridge House.

Finally, I would like to express gratitude to my family for the love and support they have constantly provided.

# PREFACE

In this thesis, integrated antennas and frequency multipliers are designed, fabricated, and tested at microwave, millimeter-wave, and submillimeter-wave frequencies. A double-dipole antenna is fabricated for submillimeter-wave applications, and is successfully tested at 250 GHz and 2.5 THz. A new type of antenna/lens system is presented, the extended-hemispherical dielectric lens. A complete characterization of coupling efficiencies and radiation patterns of the extended-hemispherical dielectric lens is presented for an on-axis element. Also, off-axis calculations are presented, showing all important parameters versus off-axis displacement: scan angle, directivity, Gaussicity, and reflection loss. Experimental pattern measurements of imaging arrays at 250 GHz are included, and show excellent agreement with the theory. Some design rules are discussed for imaging arrays on dielectric lens antennas.

A X7 DHBT frequency multiplier is presented which has low spurious harmonics for a 1 GHz input frequency. A novel frequency multiplier is also presented which is designed to operate in a varactor mode with good conversion loss ( $> 8$ dB), yet with a wide bandwidth. A MIC version is successfully tested at an output frequency of 6-10 GHz. A MMIC version is designed, fabricated, and tested at an output frequency of 60-90 GHz.

# TABLE OF CONTENTS

# LIST OF FIGURES

Figure

# LIST OF TABLES

# LIST OF APPENDICES

Appendix

# CHAPTER I

# INTRODUCTION

The millimeter-wave frequency range is defined from 30 GHz to 300 GHz, and the submillimeter-wave frequency range is defined from 300 GHz to 3 THz. These frequencies have certain properties which result in an advantage over infrared and microwave frequencies. An immediate advantage over microwave frequencies is the smaller wavelengths. This translates into both smaller circuits and smaller antennas, which means that millimeter-wave systems can be fabricated using integrated circuit techniques. The shorter wavelengths also result in a higher resolution for a given size aperture, which is useful for imaging and radar applications. Another advantage over microwave frequencies is the availability of greater bandwidths. As the communications spectrum at microwave frequencies becomes increasingly crowded, millimeter-wave systems provide a source of fresh spectrum, and are sure to be used in the not too distant future in the emerging areas of Personal Communication Systems (PCS) [56, 51] and Personal Communications Networks (PCN) [6, 55]. Certain bands of millimeter-wave frequencies also have low attenuation in smoke or adverse weather conditions such as fog or rain [7]. This characteristic, coupled with the ability for high resolution, has traditionally interested the military and science sectors for remote sensing and imaging applications [7]. Recently, there has been much interest

in the development of low-cost millimeter-wave systems for commercial applications such as automobile automatic cruise control [15, 74], Intelligent Vehicle Highway Systems (IVHS) [68, 77], and aircraft landing systems [36]. Millimeter-wave systems are also useful for the observation of spectral lines of a variety of chemical compounds. They are therefore used in radio astronomy to map out the chemical composition of the galactic system [24], and for the enviromental monitoring of certain molecular contents in the earth's atmosphere [82, 46].

Recent advances in millimeter-wave technology promise to further their widespread use. The biggest advance in millimeter-waves in the last decade has been in the area of monolithic antenna and circuit design. For example, it is now possible to fabricate millimeter and even submillimeter Schottky diodes using an entirely monolithic approach [50]. It is therefore possible to build Schottky diodes directly into a planar circuit and/or antenna, yielding low-cost integrated mixers/receivers [34, 54], and frequency multipliers [14, 43]. Very recently, monolithic low-noise amplifier chips at W-band frequencies have become increasingly available [55, 79]. This provides a much needed component for the design of low-noise communications and radar modules. Finally, in the past decade there has been significant development at millimeter-wave frequencies of an often overlooked component: the planar antenna. Integrated circuit techniques combined with antennas have provided integrated Vivaldi antennas [70], integrated horn antennas [66], and the dielectric lens antenna [28].

## 1.1 Overview of Thesis

This thesis deals with two specific components that are necessary in a millimeter-wave receiver (Fig. 1.1): the antenna, and the frequency multiplier. The antenna is the first and most important component of any millimeter-wave system. Its function

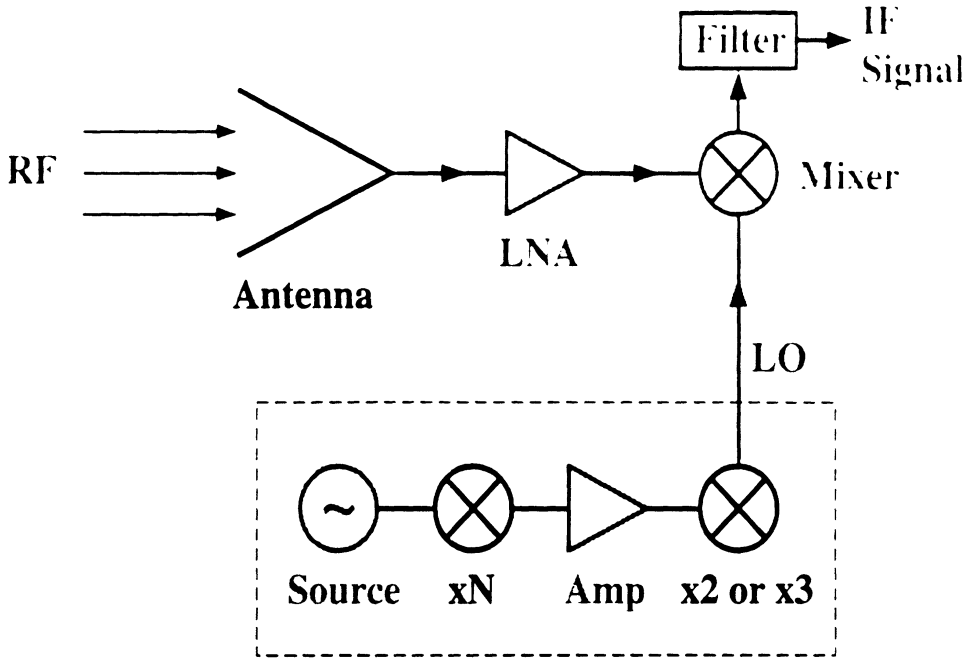


Figure 1.1: Block diagram of a millimeter-wave receiver. The dark areas represent the subjects of this thesis.

is to collect the RF power with an efficiency as close as possible to the diffraction limit of a given size area (aperture efficiency), and with as little associated losses (conductor loss, dielectric loss, etc.) as possible. The RF power collected is usually very small, and the antenna is therefore followed by a low-noise amplifier (LNA) to increase the signal power. The RF signal is then mixed with a stable local oscillator (LO) signal to produce an intermediate frequency (IF) signal bearing some type of information, such as a communication signal or a radar signal. The quality of the signal to noise ratio will determine the amount of information that can be recovered from the signal [64]. The noise will be directly affected not only by the efficiency of the antenna, but also by the spectral quality of the local oscillator. A good local oscillator signal must be sufficiently strong and have very low phase noise. This can be achieved with a waveguide mounted Gunn oscillator, but is expensive and non-planar. A less expensive alternative is to begin with a very low phase noise oscillator

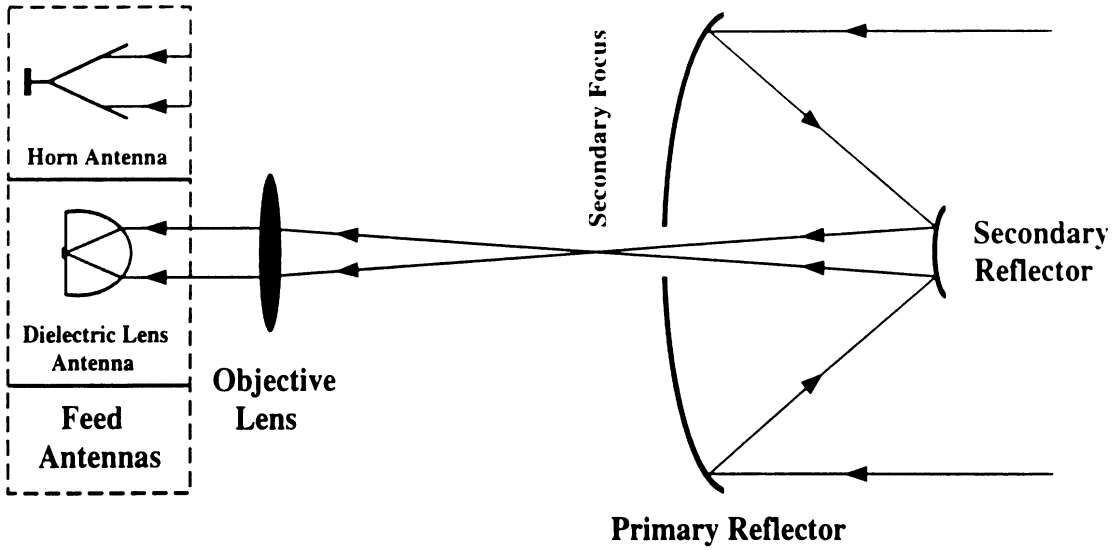


Figure 1.2: A feed antenna coupled to a Cassegrain reflector system.

(crystal-based or utilizing a dielectric resonator) at a lower frequency, and then use a cascade of frequency multipliers and amplifiers up to the desired LO frequency.

A typical configuration for a complete receiver system for remote sensing or radioastronomical use at millimeter-wave frequencies is shown in Figure 1.2. Here, a Cassegrain reflector is coupled through an objective lens to the feed antenna/receiver system shown in Figure 1.1. The radiation patterns of the feed antenna must couple with maximum efficiency to the quasi-optical system in order to maximize the signal-to-noise ratio, which is particularly important when detecting the faint signals in radioastronomical applications. Traditionally, the feed antenna utilized has been a machined waveguide horn [17, 21] or a machined corner-cube antenna [89, 25]. The machined waveguide horn is usually used up to frequencies of 600 GHz, where the cost of manufacturing the horn is not too excessive and the feasibility of using planar E-plane circuits is possible. The waveguide horn can produce radiation patterns which couple efficiently to a quasi-optical system, but due to the manufacturing cost are not practical for imaging applications. For frequencies higher than 600 GHz (in-

cluding terahertz frequencies), a corner-cube antenna has traditionally been used, which is coupled together with a whisker-contacted diode. The corner-cube antenna is a simple design, however, it does not couple with maximum efficiency to a quasi-optical system. Recently, integrated horn antennas that are fabricated in silicon have been introduced [66], and have successfully demonstrated high coupling efficiency radiation patterns up to 2.5 THz. However, this approach uses thin dielectric membranes and it will be difficult to implement monolithically integrated circuits on them. Integrated corner-cube antennas have also been introduced [32], but suffer from the same constraints as the integrated horn antenna, and have thus not replaced the traditional whisker-contacted corner-cube. Recently, the development of an entirely different type of feed antenna has matured, which can now offer the possibility of high efficiency coupling to a quasi-optical system, the ease of arraying elements for imaging, and the simplicity of monolithically integrating circuits, all in a low-cost design: the dielectric lens antenna.

## 1.2 Integrated Antennas and Dielectric Lenses

Millimeter-waves antennas can be designed using the traditional techniques used at microwave frequencies. For example, antennas can be printed on a dielectric substrate. At millimeter-waves, the substrate should be very thin, or else the antenna will suffer from power loss into substrate modes and could also have poor radiation patterns [65, 70]. The thickness required to avoid substrate mode power loss is typically less than $.02\lambda_d$ for dipoles and $.04\lambda_d$ for slot antennas [3]. One way to synthesize a thin substrate is to place the antenna on a very thin dielectric membrane [4, 32], which is typically between 1 to 3 $\mu$m thick. The membranes are integrated on a silicon or GaAs wafer and the antennas radiate as if suspended in free-space,

yielding a high-efficiency antenna. Following this idea, Chapter 2 presents a novel antenna for submillimeter-wave and terahertz frequency applications: the integrated double-dipole antenna for high-gain integrated reflector illumination.

Since planar antennas integrated on thin dielectric membranes are, in general, thin and fragile, they are limited to specialized applications, such as low-noise radio-astronomical receivers. Another technique to avoid substrate modes is based on an idea from the optical domain, and was introduced by Rutledge and Muha in 1981 [71]: the dielectric lens. The planar antenna (presumably on a thick substrate) is placed directly on the back of a dielectric lens. If the dielectric constant of the lens is close to that of the antenna substrate, then substrate modes will not exist. Additionally, antennas placed on dielectric lenses tend to radiate most of their power into the dielectric lens side, which can then be focused by the lens surface. The ratio of powers between the dielectric and air is approximately $\epsilon_r^{3/2}$ for elementary slot and dipole-type antennas, where $\epsilon_r$ is the relative dielectric constant of the lens. For an $\epsilon_r$ of 12-13 (silicon or GaAs), this means that 2% of the power is radiated into the air-side for an elementary antenna. The dielectric lens is an attractive solution for millimeter-wave antennas, since it provides mechanical rigidity and a thermal heat sink. In addition, dielectric lenses can produce high quality Gaussian-beams which are useful for efficient coupling to a quasi-optical system.

Dielectric lenses can be hemispherical, hyperhemispherical, or ellipsoidal (Fig. 1.3), and many researchers have placed various antennas on these lenses for receiver applications. Log-periodic [19], spiral [20], double-slot, and double-dipole antennas have been successfully used on quartz and silicon dielectric lenses from 30 GHz to 600 GHz [12, 41, 76, 87]. The hyperhemispherical lens is a hemispherical lens with an attached extension length of R/n, where n is the index of refraction of the

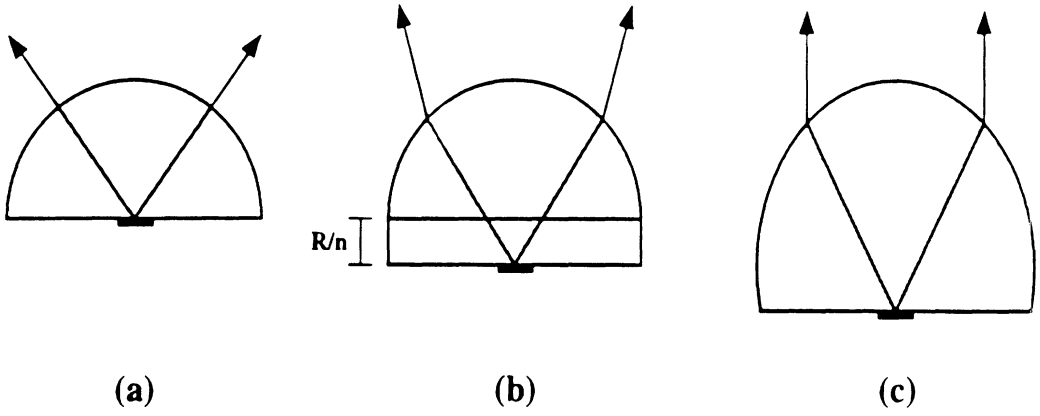


Figure 1.3: Different types of dielectric lens configurations: (a) hemispherical, (b) hyperhemispherical, and (c) elliptical.

lens, and R is the radius of the lens. The hyperhemispherical lens was borrowed into the millimeter-wave field from optics [70, 71] and it was found that radiation patterns from these lenses were broad and even multi-lobed in some cases. The hyperhemispherical lens is aplanatic, implying the absence of spherical abberations [10]. This implies that if an optical system is designed such that all the rays are being focused to a point, the hyperhemispherical lens can be added to the system and all the rays will still focus to a point (Fig. 1.4). This can also be expressed in mathematical form by the *sine condition*, which is derived from the geometry of the hyperhemisperical lens [70]:

$$\sin \theta_1 / \sin \theta_0 = n_1 \tag{1.1}$$

The $f$-number of the objective lens alone is:

$$f_0\text{-number} = 1/(2\sin \theta_0) \tag{1.2}$$

whereas the $f$-number at the hyperhemispherical lens is:

$$f_1\text{-number} = 1/(2\sin \theta_1) \tag{1.3}$$

Therefore, the hyperhemispherical lens has reduced the $f$-number that is required of the feed antenna. In antenna terms, the hyperhemispherically shaped dielectric lens

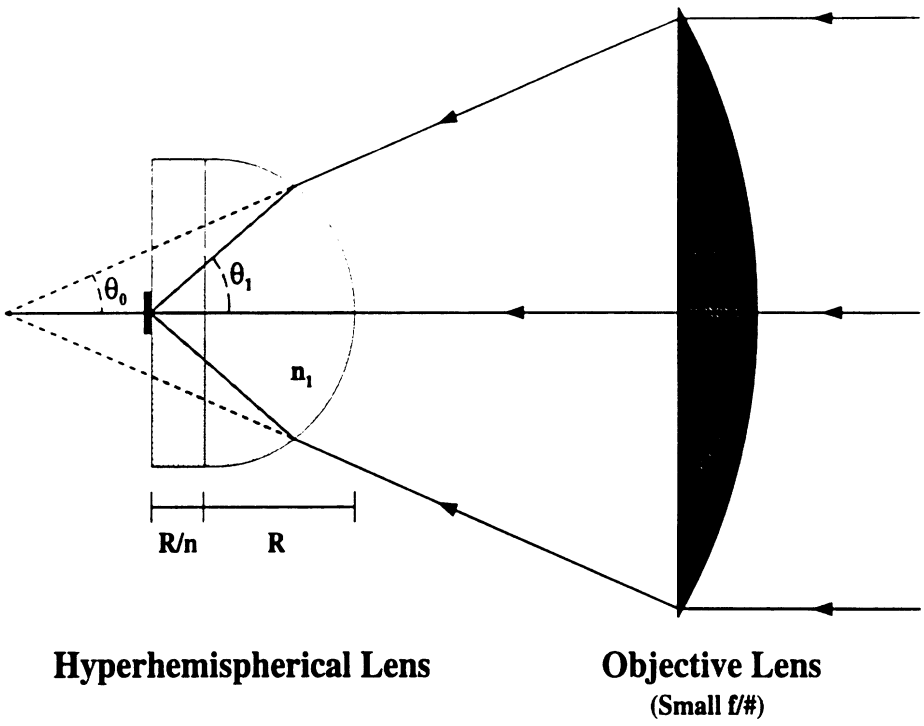


Figure 1.4: The hyperhemispherical lens combined with an objective lens.

bends the rays radiated by the integrated antenna towards the broadside direction, thereby sharpening the pattern and effectively increasing the gain of the integrated antenna by $n^2$. The hyperhemispherical lens is capable of coupling well to a Gaussian-beam system, but couples well to a converging beam and not to a planar equiphase front.

On the other hand, any antenna placed at the focus of the elliptical lens will result in a far-field pattern with a main-beam that is diffraction limited by the aperture of the elliptical lens. In a ray analysis, an elliptical dielectric lens with a point source at its more distant focus refracts the emitted rays so that they emerge parallel to each other [39] (Fig. 1.5). The diffraction-limited patterns have been verified for log-periodic and spiral antennas [80], and also for a simple dipole antenna [1], a double-dipole antenna [75] and a double-slot antenna [27]. The main difference in the measured patterns between these antennas is in the sidelobe and cross-polarization

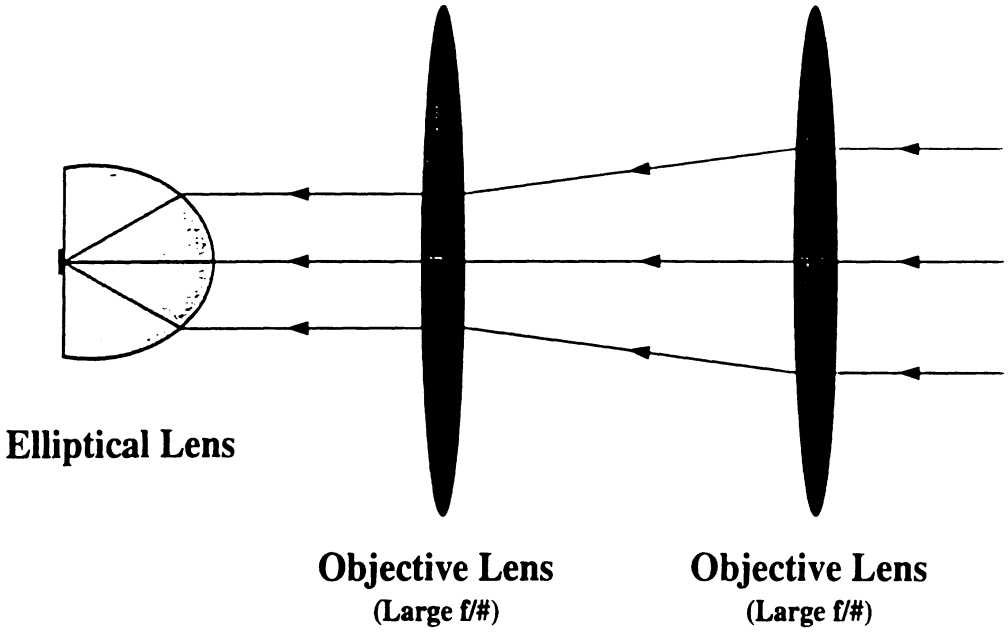


Figure 1.5: The elliptical lens combined with an objective lens system.

levels. The elliptical lens is compatible with a large $f$-number imaging system due to the potential of achieving very narrow beam patterns. The elliptical lens couples well to a Gaussian-beam at its minimum waist, where there is a planar equiphase front.

## 1.3 Extended Hemispherical Lenses

An extended hemispherical lens is a hemispherical lens (with radius R), and an attached rectangular extension length L (Fig. 1.6). It should be noted that the hyperhemispherical lens is a special case of the extended hemispherical lens. As discussed in section 1.2, an integrated antenna placed on the dielectric lens will preferentially radiate most of its power into the lens. It was found experimentally by Büttgenbach in 1992 that by varying the extension length L, the directivity of the far-field patterns emanating from the lens could be controlled [12]. In particular, Büttgenbach found that near diffraction-limited patterns could be achieved at a posi-

tion after the hyperhemispherical point [13] and just before the synthesized elliptical point. Büttgenbach's observations were confined to a few radiation patterns, and did not provide a full characterization of the lens. In order to implement the lens in a quasi-optical system for maximum efficiency, a more rigorous understanding of extended hemispherical lenses is necessary. The need for a full characterization of the extended hemispherical lens prompted us to develop a ray-optics/field-integration formulation to solve for its radiation properties with a varying extension length.

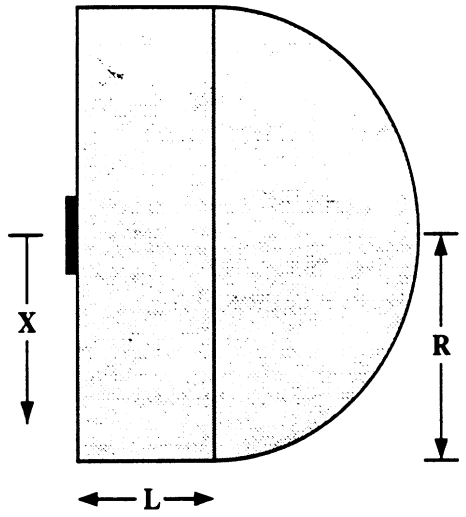


Figure 1.6: The extended hemispherical lens system.

Chapter 3 presents a full characterization of silicon ($\epsilon_r$=11.7) and fused quartz ($\epsilon_r$=3.8) extended hemispherical lens. It is shown from a geometrical interpretation that there exists a specific extension length that effectively synthesizes an elliptical lens. Universal design curves are presented for these two dielectric constants, including the directivity and maximum "Gaussicity" as a function of the extension length. The term "Gaussicity" is defined as the coupling efficiency of a far-field pattern of an antenna to the far-field pattern of a Gaussian-beam. The total power coupling into the antenna, termed the "Gaussian-coupling efficiency", is the product of the Gaussicity and all losses (lens-air reflection loss, dielectric loss, backside loss, etc.).

The calculation of these losses for silicon and quartz lenses is included in Chapter 3. Chapter 3 also presents the experimental results at three different extension lengths, one near the hyperhemispherical position, one near a synthesized elliptical position, and one at an intermediate position between these two positions. The directivities were measured at these positions, and a simple quasi-optical Gaussian-coupling experiment was designed for verification of the Gaussian-coupling efficiencies.

The extended hemispherical system is very practical, since it results in an antenna/lens system which couples to a wide range of quasi-optical systems simply by varying the extension length behind the hemispherical position. In addition to varying the extension length, it is possible to displace the feed antenna on the back of the lens by a distance X from its centered position. The resulting far-field pattern will scan away from boresight. Therefore, an array of antennas can be designed, with each antenna pointing at a different position in space. This would be very useful for imaging applications, where a snapshot photo could be taken of a scene at millimeter-wave frequencies. The off-axis performance of the extended hemispherical lens was analyzed and is presented in Chapter 4. Using once again a ray-optics/field-integration formulation, the directivities and Gaussian-coupling efficiencies are investigated for an element placed off-axis at different extension lengths. Both a silicon and fused quartz lens are considered. Chapter 4 presents important parameters and design curves necessary for the design of off-axis systems: scan angle, directivity, Gaussicity, and reflection loss versus extension length and off-axis displacement.

## 1.4 Balanced Frequency Multipliers

As described earlier, monolithic technology has advanced rapidly in the past decade, providing a variety of millimeter and submillimeter-wave circuits and anten-

nas. However, the component which has not kept pace with these advancements is the local oscillator (LO). Tubes and lasing-type sources can provide much millimeter-wave power, but are large, expensive, and not reliable enough for space-based applications [63]. Solid-state sources can be classified into two categories: two-terminal or three-terminal devices. Low-noise Gunn and Impatt oscillators, which are two-terminal devices, are limited to about 150 GHz [56]. There has also been tremendous advancements in three-terminal technology (submicron pseudomorphic InP HEMT) in the last decade, pushing the frequency limit to well over 100 GHz [67]. However, for a LO source which is low-noise, compact, and rugged (possibly space-qualified), the most viable approach is to still use a low-frequency oscillator in cascade with a series of frequency multipliers and amplifiers (Fig. 1.7), with the amplifiers limited to W-Band frequencies. For frequencies below 100 GHz, the low frequency oscillator is typically a crystal-based oscillator or a dielectric-resonator oscillator (DRO) with a transistor. For frequencies exceeding 100 GHz, the oscillator may be a Gunn oscillator followed by waveguide multipliers providing a low noise source. For a more detailed description of the state of the art, see [11].

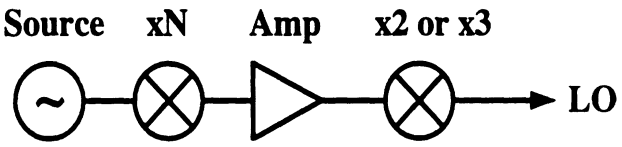


Figure 1.7: Local Oscillator Chain.

Active frequency multipliers, based on three-terminal devices, are an effective means to achieve frequency multiplication at the start of the multiplication chain. Passive devices such as Schottky diodes or step-recovery diodes can be used, but require high input powers (> 15 dBm) and typically have high conversion losses, resulting in the need for both pre-amplification and post-amplification. On the other

band, active frequency multipliers require small input powers (-2 dBm to 6 dBm) and have high conversion efficiencies, and in some cases, even have conversion gain. Active frequency multipliers are already used throughout the satellite industry at frequencies below 5 GHz. However, these designs usually use conventional BJT devices and are constrained to operate at less than 5 GHz due to the low $f_T$ of these devices. For operation at higher microwave or low millimeter-wave frequencies, it is necessary to use a higher frequency bipolar device, such as a double-heterojunction BJT (DHBT). In this case, the distributed effects become important and it is necessary to first develop a technique to derive a non-linear model of the DHBT, and then simulate the active frequency multiplier taking into account the transmission line effects. Chapter 5 presents the simulation, design, and measurement of a X7 DHBT active frequency multiplier.

At higher millimeter and submillimeter-wave frequencies, only passive devices such as diodes have sufficient efficiency for frequency multiplication. For example, monolithic broadband balanced doublers have been demonstrated in the literature using varistor diodes [9, 59]. These utilize the nonlinearity of the current-voltage curve to generate harmonic multiplication, and are typically biased near the turn-on of the diode. Page has shown that the conversion efficiency of a varistor multiplier is limited to $1/N^2$ [60]. This means that in a varistor mode, a doubler is limited to 25% efficiency, and a tripler to 11% efficiency. A more efficient multiplier can be made using a varactor diode, which utilizes the nonlinearity of the capacitance-voltage curve. The well-known Manley and Rowe relations prove that the efficiency of an ideal varactor can be 100% [53, 62]. In practice, the series resistance of a diode and the inability to exactly match all the embedding impedances will considerably reduce the conversion efficiency. However, a varactor frequency multiplier will still

have a higher conversion efficiency than a varistor frequency multiplier.

Current varactor designs are either narrowband [16] or have not yet demonstrated a high conversion efficiency [11]. Chapter 6 presents a balanced varactor multiplier which is based on grounded-CPW and slotline transmission media together with Schottky varactor diodes. A balanced structure offers inherent isolation in the output port from all odd harmonics including the fundamental frequency. A novel balun is designed to achieve the necessary grounded-CPW to slotline transition. A 1/10 scale model was implemented on a high dielectric constant substrate ($\epsilon_r$ =10.2), and is presented. A chip was fabricated in GaAs for an output frequency of 60-90 GHz, in which the varactor diodes are monolithically integrated into the circuit. A simple theoretical analysis of the chip is presented, which shows how the position of the airbridge can be used to tune the frequency conversion. The fabrication of the chip is discussed, and the measured I-V and C-V characteristics of the diode are presented. Chapter 6 concludes with a presentation of the measured results, and a comparison with the theory.

## 1.5 Future Work

Chapter 7 concludes the thesis with a discussion of possible future work in the area of frequency multipliers, mixers, and dielectric lenses. First, it would be useful to analyze the operation of the dielectric lens when coupled together with an objective lens. A dielectric lens coupled with an objective lens would be the most likely configuration used in commercial applications, if a larger effective aperture (and thus higher directivity) than that of the dielectric lens is necessary. Then, a novel frequency quadrupler, taking advantage of balanced/unbalanced transitions in transmission lines is presented. This would be useful for higher-frequency LO

radioastronomical applications. Also, novel designs for a quasi-optical frequency doubler and a subharmonic mixer are presented. The quasi-optical frequency doubler combines the technology of the two areas of specialization in this thesis, the frequency multiplier and the double-slot antenna on an extended hemispherical dielectric lens, into a single circuit. Finally, a variety of circuit configurations are considered which exploit the angular separation of beams via spatial separation of antennas in an extended-hemispherical dielectric lens system.

# CHAPTER II

# TERAHERTZ REFLECTOR

The use of thin dielectric membranes for millimeter-wave and terahertz integrated-circuit antennas is a well established technique for high-efficiency designs [37, 66]. The membranes are very thin compared to a free-space wavelength, and the antennas do not suffer from dielectric and substrate-mode losses. Measurements on integrated-horn and corner-reflector antennas show well behaved patterns and main-beam efficiencies greater than 80% at 100 GHz, 800 GHz, and 2.5 THz [5, 33]. However, the corner-cube antenna has non-equal E and H-plane patterns and a relatively high cross-polarization component (-16 dB) in the 45°-plane. Also, all of these antennas require a controlled process of anisotropic etching of silicon or GaAs wafers. A competitive design at terahertz frequencies is to use a radiating structure consisting of two dipole antennas on a dielectric membrane and backed by a ground plane. The structure results in a rotationally symmetric pattern and a very low cross-polarization component (Fig. 2.1). The double-dipole antenna is very simple to fabricate, resulting in similar directivities to the integrated-horn antenna (10-13 dB), and has a high coupling efficiency to f/.7-f/1 reflector systems (80-90%).

For high resolution tracking, or for efficient coupling to long focal length antenna systems, a much higher gain antenna is needed. This can be readily accomplished by

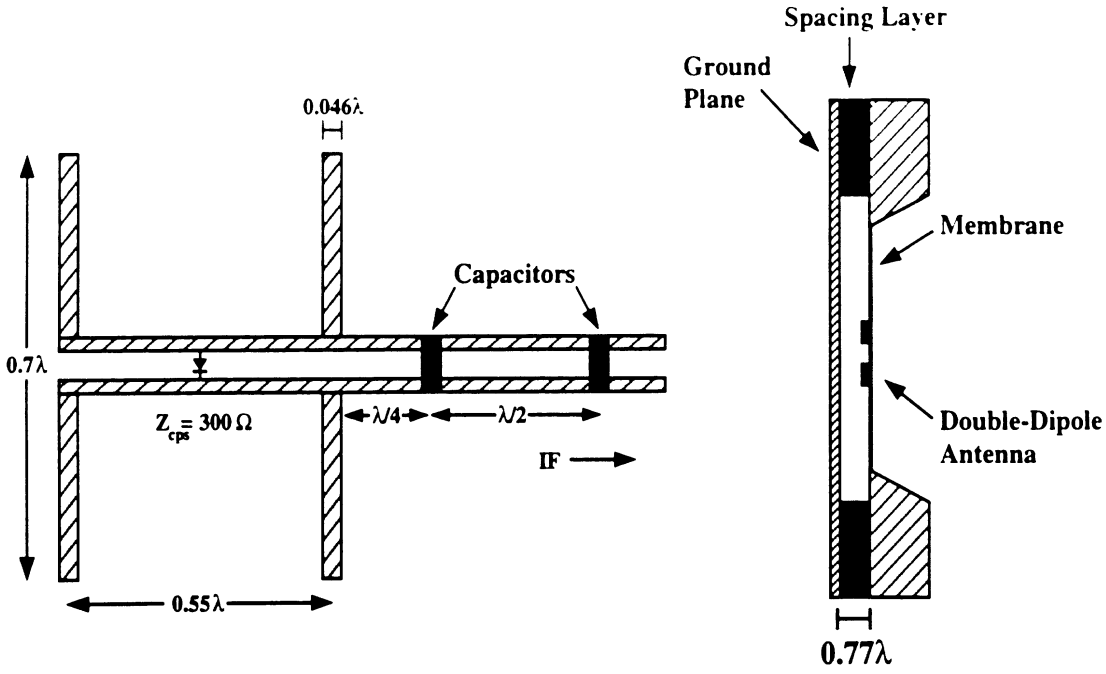


Figure 2.1: Top view and side view of double-dipole antenna on a membrane.

combining a reflector with the double-dipole design described above (Fig. 2.2). The design is similar to the dielectrically filled parabola investigated by Siegel et. al. [73]. However, it requires no dielectric filling and the associated matching layer which may be difficult to fabricate at submillimeter-wave and terahertz frequencies. The design exhibits high-coupling efficiency to Gaussian beams and can be easily arrayed for imaging systems applications. The imaging may be accomplished by fabricating an array of multiple reflectors or by using multiple double-dipole antennas in the focal region of a single reflector (Fig. 2.3).

## 2.1 Double-Dipole Antenna Design & Measurement

Double-dipole antennas have been previously investigated at millimeter-wave frequencies and have showed promise for high-efficiency applications [28, 61, 75]. The design consists of a double-dipole antenna integrated on a dielectric membrane and

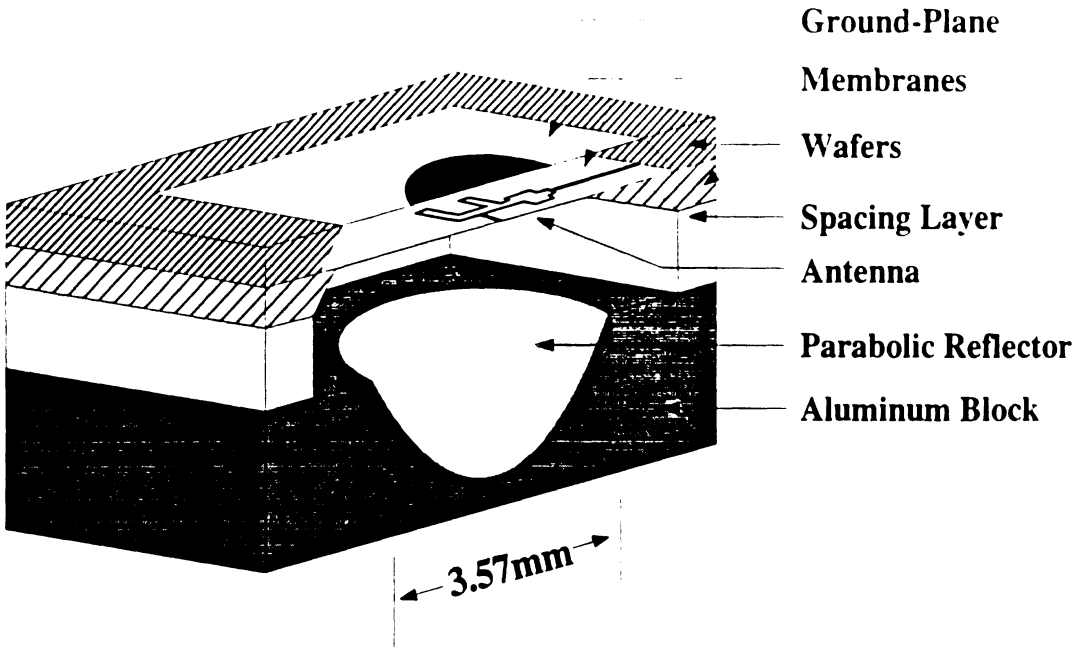


Figure 2.2: Perspective of reflector antenna with double-dipole and ground plane.

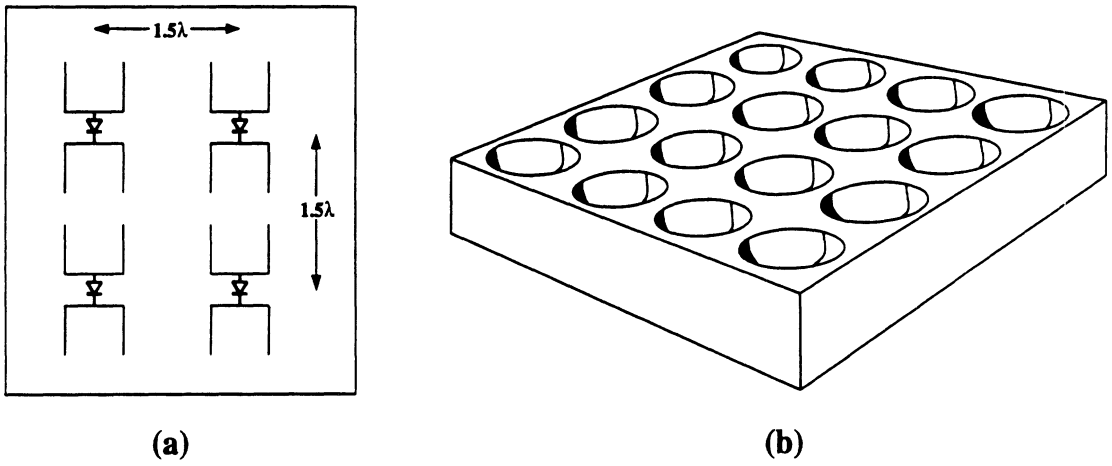


Figure 2.3: Methods of arraying. (a) Arraying the feed in the focal plane of the reflector. and (b) Arraying the reflector with a simple feed in the focal plane of the imaging system.

backed by a ground plane. The detector is integrated at the center of the coplanar stripline. A low-pass filter is used to isolate the IF/bias lines from the antenna, and consists of an RF capacitor located $\lambda/4$ away from the antenna. At RF frequencies the capacitor appears as a short, which translates to an open at the antenna. For far-field pattern calculations, the antenna current distribution is given by the standing-wave current on an open-circuited transmission line. The method of images is used to account for the ground plane [8]. The radiation pattern can be made rotationally symmetric by the choice of the antenna lengths ($l$), the antenna spacing ($d$) and the ground-plane distance from the membrane ($h$).

**Antenna #1:** ($l = 0.7\lambda, d = 0.55\lambda, h = 0.77\lambda$, $Z_{cps} = 300\Omega$)

| Frequency | $Z_{ant}$ | Gain | X-pol | $\epsilon_{mb}(-20dB)$ | $\epsilon_{Gauss}(\theta_0=30°)$ | $\epsilon_{Gauss}(\theta_0=27°)$ |
|---|---|---|---|---|---|---|
| $0.90f_0$ | $52 - j15\Omega$ | - | - | - | 64.7% | 66.5% |
| $0.95f_0$ | $39 + j2\Omega$ | 11.8 dB | -27 dB | 82% | 77.4% | 77.1% |
| $1.00f_0$ | $43 + j13\Omega$ | 11.7 dB | -26 dB | 88% | 83.4% | 81.1% |
| $1.05f_0$ | $55 + j10\Omega$ | 11.2 dB | -25 dB | 91% | 84.8% | 80.9% |
| $1.10f_0$ | $60 + j20\Omega$ | - | - | - | 82.7% | 77.3% |

**Antenna #2:** ($l = 0.9\lambda, d = 0.59\lambda, h = 0.73\lambda$, $Z_{cps} = 200\Omega$)

| Frequency | $Z_{ant}$ | Gain | X-pol | $\epsilon_{mb}(-20dB)$ | $\epsilon_{Gauss}(\theta_0=27°)$ | $\epsilon_{Gauss}(\theta_0=24°)$ |
|---|---|---|---|---|---|---|
| $0.90f_0$ | $23 + j30\Omega$ | - | - | - | 66.5% | 67.9% |
| $0.95f_0$ | $30 + j25\Omega$ | 13.4 dB | -28 dB | 85% | 82.1% | 80.9% |
| $1.00f_0$ | $50 + j50\Omega$ | 13.2 dB | -29 dB | 91% | 88.1% | 84.9% |
| $1.05f_0$ | $80 + j60\Omega$ | 12.8 dB | -30 dB | 93% | 88.7% | 84.1% |
| $1.10f_0$ | $100 + j70\Omega$ | - | - | - | 86.3% | 80.9% |

Table 2.1: Impedance and Radiation Properties of Two Double-Dipole Designs.

Two sets of double-dipole antennas with rotationally symmetric patterns were designed (see Table 2.1). The first design had parameters $(l, d, h, Z_{cps})$ of $(0.7\lambda, 0.55\lambda, 0.77\lambda, 300\Omega)$ and a measured input impedance on a 2 GHz microwave model around $50\Omega$ for a $\pm 5\%$ bandwidth (Fig. 2.4). The calculated main-beam efficiency [18] (to -20 dB) is 88% and the coupling-efficiency to a Gaussian beam with

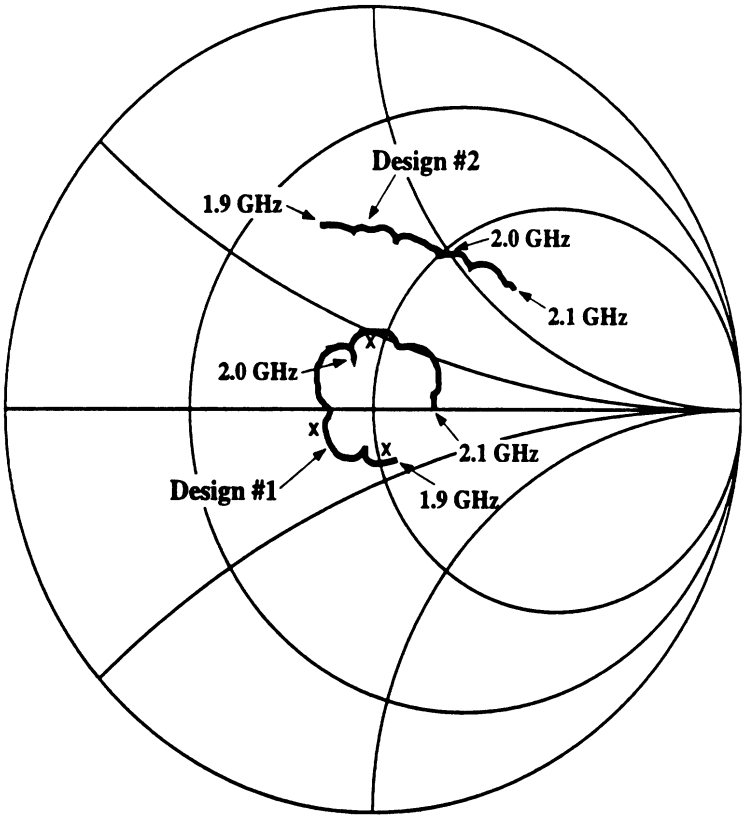


Figure 2.4: Measured input impedance of feed with a 2 GHz model. The x's represent the theoretically predicted input impedances.

$\theta_0$=30° is 84%. The design has a 10-dB beamwidth of 78° and a directivity of 11.7 dB. The second design included a short stub off the detector and had parameters $(l, d, h, Z_{cps})$ of $(0.9\lambda, 0.59\lambda, 0.73\lambda, 200\Omega)$ and a measured input impedance around $50 + j50\Omega$ for a ±5% bandwidth. Here, the calculated main-beam efficiency [18] (to -20 dB) is 91% and the coupling-efficiency to a Gaussian beam with $\theta_0$=27° is 84%. This design has a 10-dB beamwidth of 70° and a directivity of 13.2 dB. Table 2.1 shows that the two designs maintain good efficiencies for at least a ±5% bandwidth. Both feed antennas can illuminate a reflector uniformly in phase with a -10 dB to -20 dB taper depending on the size of the reflector. Therefore both designs are ideal as feeds for paraboloidal reflectors with an f/D between 0.7 and 1.0.

The measured electromagnetic coupling between two double-dipole antennas (for either design) in the H-plane was lower than -20 dB and -30 dB for a center-to-center spacing of $1\lambda$ and $1.5\lambda$, respectively. The coupling in the E-plane was negligible for center-to-center spacing greater than $1.25\lambda$. It is therefore possible to array the antennas for diffraction-limited imaging.

The first design $(0.7\lambda, 0.55\lambda, 0.77\lambda, 300\Omega)$ was built for 246 GHz applications (Fig. 2.5). The antenna was fabricated on a 1.2 $\mu$m-thin membrane and the metalization was 4000 Å thick evaporated gold. The capacitors were a 1 $\mu$m-thick layer of polymide on top of which was another 4000 Å of gold metalization. For measurement purposes, a bismuth bolometer was integrated at the center of the coplanar stripline, with dimensions of 15 $\mu$m by 20 $\mu$m. The bolometer impedance is 80Ω with a responsivity of 10 V/W at a 100 mV bias. The pattern was measured at 246 GHz using an 82 GHz Gunn source, and a wideband (220-270 GHz) tripler. The Gunn source was then modulated at 300 Hz, and the output from the bolometer was fed to a PAR-124A lock-in amplifier. The signal-to-noise ratio was better than 20 dB.

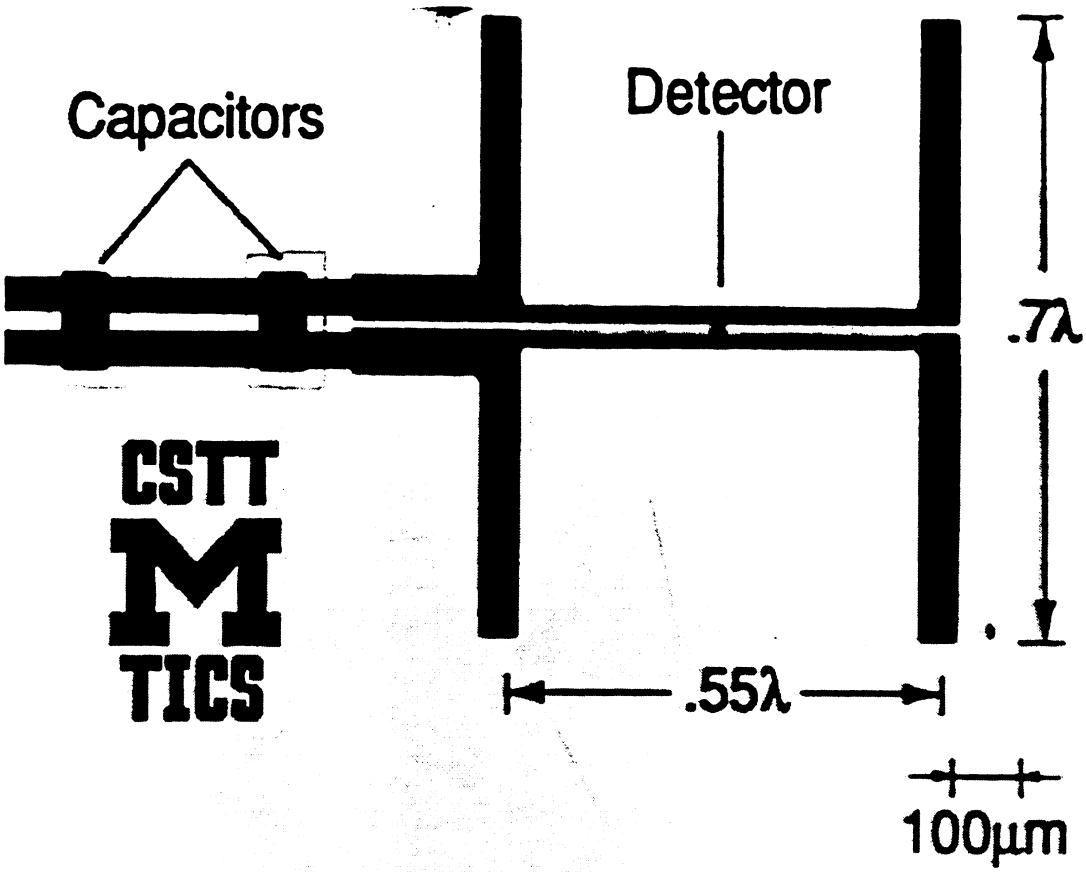


Figure 2.5: Photograph of the double-dipole antenna for 246 GHz. The two rectangles to the left of the antenna are metal-insulator-metal capacitors for the IF-filter.

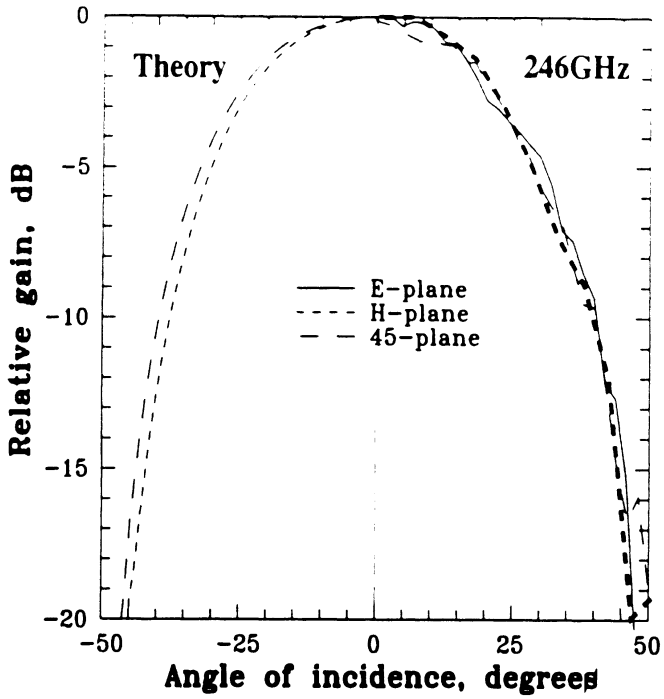


Figure 2.6: Theoretical (left) and measured (right) double-dipole patterns at 246 GHz.

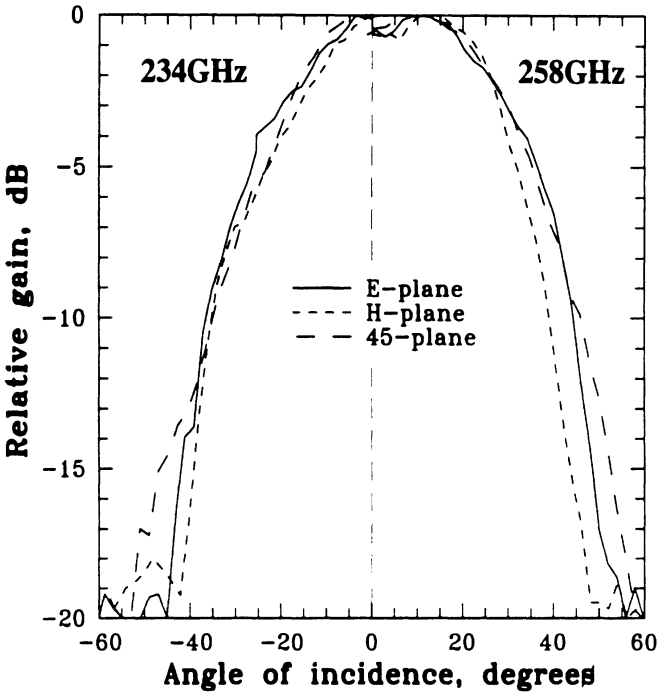


Figure 2.7: Measured double-dipole patterns at 234 GHz (left) and 258 GHz (right).

The measured patterns agree very well with theory up to 45° (Fig. 2.6) where diffraction effects from the measurement set-up dominate. The theory predicts a sidelobe level lower than -13 dB and a -27 dB cross-polarization component in the 45°-plane. The sidelobe level could not be confirmed due to the measurement set-up, but a cross-polarization component of less than -22 dB was measured at 30 – 35°. Pattern measurements at $0.95f_0$ (234 GHz) and $1.05f_0$ (258 GHz) agree well with theory and result in symmetric patterns (Fig. 2.7). The slight dip of 1 dB at normal incidence at 254 GHz is not predicted by theory and could be due to standing waves in the pattern measurement setup.

## 2.2 The Terahertz Reflector Antenna

### 2.2.1 Theory

The far-field patterns of a parabolic reflector with a double-dipole feed are found by computing the Fourier integral of the fields in the aperture plane. The aperture plane is chosen to be the focal plane of the reflector [8, 69]. The reflector is assumed to be in the far field of the feed antenna, and a ray optics approach is used to find the fields on the aperture plane. For a 30$\lambda$-diameter reflector with a f/D of 0.65 illuminated by the double-dipole feed considered above, the 3-dB and 10-dB beamwidths are 4.4° and 8°, respectively, resulting in a 39 dB gain. The cross-polarization was also computed and found to be below -30 dB.

When the feed is displaced from the focus as in the case of a focal plane imaging system, a search is needed to find the specular point for any given observation point in the aperture plane (see Fig. 2.8). The specular point must be found in order to determine the phase (since the phase is no longer uniform across the focal plane) and the amplitude (resulting from the angle the ray is emitted from the feed). One way to

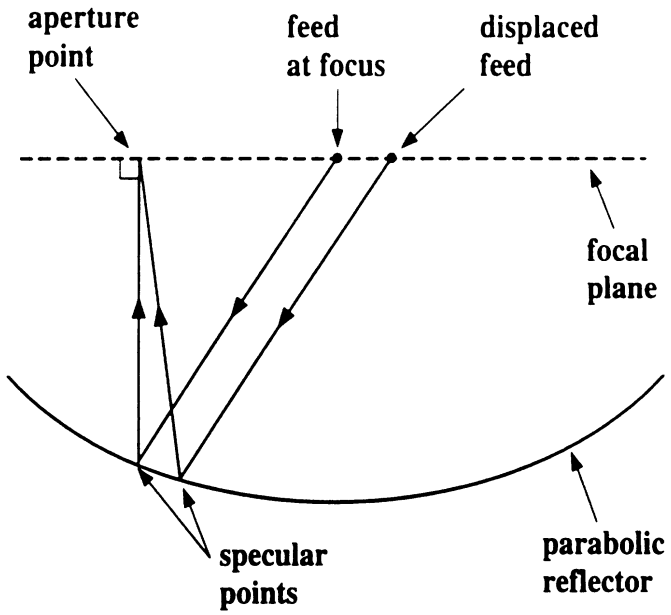


Figure 2.8: A diagram of the ray-tracing method. Notice that for a feed displaced from the focus, the ray is not collimated.

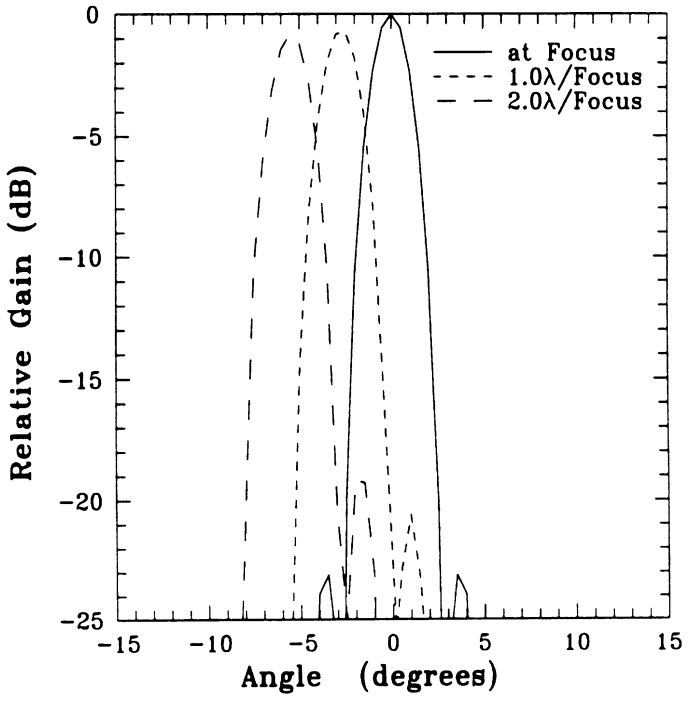


Figure 2.9: Theoretical E-plane patterns for an on-axis and for a displaced double-dipole feed.

find the specular points is to use Fermat's principle of stationary optical path length. It is a particularly useful technique since it can be used with any arbitrary position of feed and any arbitrary surface [75]. For a given aperture point, the specular point is found by minimizing the optical path length. Fermat's principle is a well known variational expression and thus the program always converges. Figure 2.9 shows the resulting E-plane patterns for a lateral displacement of the feed from the focus. One can see that for a one wavelength feed displacement, the main beam shifted by about 3 degrees and the sidelobes remain below -20 dB.

### 2.2.2 Experiment

A double-dipole antenna with $(l, d, h, Z_{cps})$ of $(0.7\lambda, 0.55\lambda, 0.77\lambda, 300\Omega)$ was built at 119 $\mu$m on a 1 $\mu$m-thin membrane with dimensions of 4x4 mm (Fig. 2.10). The ground-plane was built on a similar membrane and consisted of a circular patch of evaporated gold 1000 Å thick with a diameter of $2.5\lambda$. The ground-plane was aligned and attached to the antenna wafer using spacers made of silicon wafers polished to approximately 92 $\mu$m thickness. It was later realized that the spacers were too thick, and the resulting measured H-plane feed patterns were not optimal. Fortunately, the Fourier transform property of the reflector is forgiving and good reflector patterns were obtained. The double-dipole antenna and ground-plane are very small compared to the reflector aperture, thus negligible power is lost due to aperture blockage. Also, the IF/bias lines are orthogonal to the polarization of the received wave resulting in minimal scattering loss.

In order to measure the reflector patterns at 119 $\mu$m, the reflector was mounted on an x-y-z-tilt positioner and moved around until finding the point where maximum power is received and symmetrical patterns are measured. The parabolic reflector

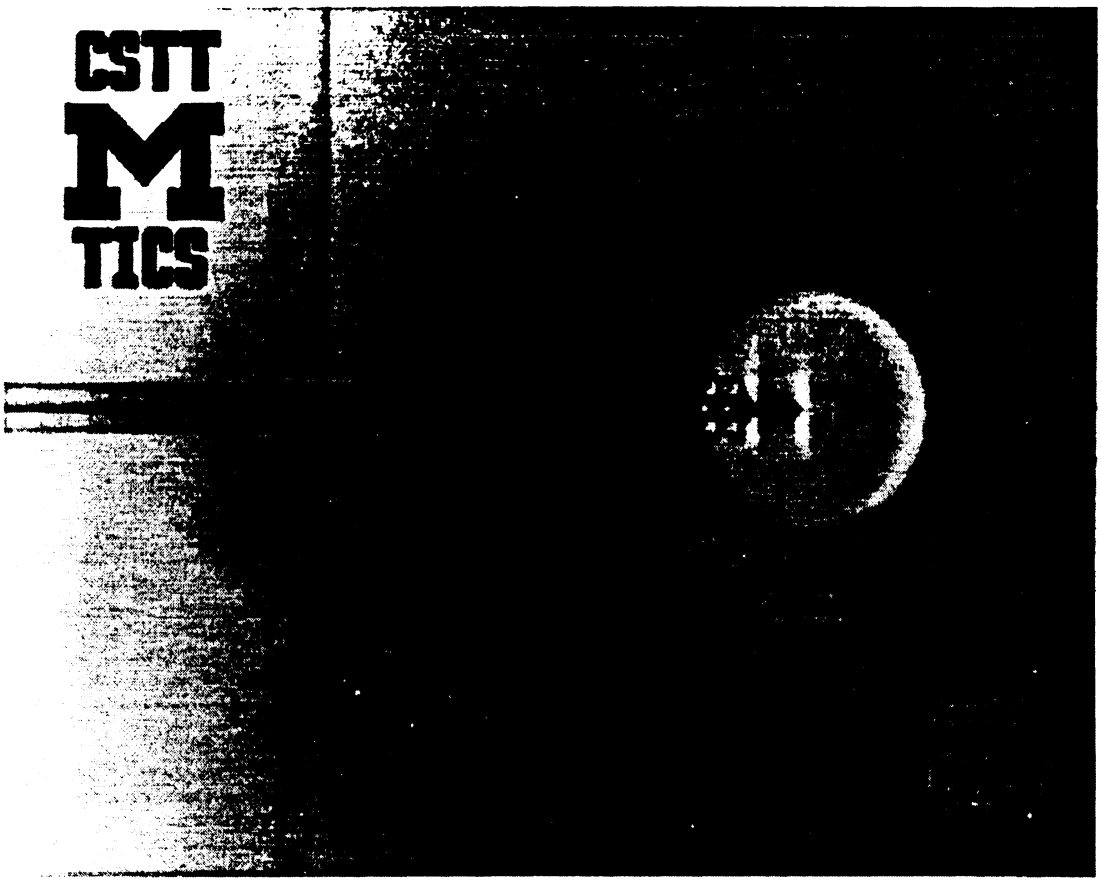


Figure 2.10: Photograph of the double-dipole antenna suspended above a circular ground-plane for 119 $\mu$m applications.

was machined out of aluminum to a surface accuracy of around 100 Å and is 30λ (3.57 mm) in diameter with a f/D of 0.65. Figure 2.11 shows the measured E, H, and 45°-plane patterns at 119 $\mu$m. The calculated directivity from the measured data is 37 dB ±0.3 dB, the uncertainty being due to the signal-to-noise ratio. Figure 2.12 shows the measured E-plane compared with theory, which predicts a directivity of 39 dB. The pattern disagreement below -15 dB and the directivity disagreement is likely due to the improperly assembled feed structure. The H-plane pattern was wider than the design, and we believe that this is due to the H-plane feed pattern being narrower than expected. Measured patterns at 119 $\mu$m also confirmed the shift in the main lobe for a displaced feed, but were not included due to the misaligned feed structure. The measurements corresponded well with the position of the main lobe in the theoretical patterns (Fig. 2.9), and thus verify the option of arraying the antennas for diffraction-limited imaging. In conclusion, the measurements show that high-gain antenna patterns are easily obtainable at submillimeter frequencies.

## 2.3 Conclusion

A high-efficiency submillimeter-wave antenna has been presented. It is a double-dipole design backed by a ground plane which results in a nearly rotationally symmetric pattern with a gain of 12-13 dB, and a high coupling efficiency to a Gaussian-beam. The input impedance is around 50Ω for a ±5% bandwidth, and will match well to a Schottky diode or SIS detector. A 246 GHz design showed very good agreement with the theoretical patterns and a measured cross-polarization level below -22 dB. The electromagnetic coupling between two sets of dipoles is below -20 dB (-30 dB) for 1λ (1.5λ) separation, thus allowing the antenna to be arrayed for diffraction-limited imaging. Measured patterns with the double-dipole antenna illuminating a

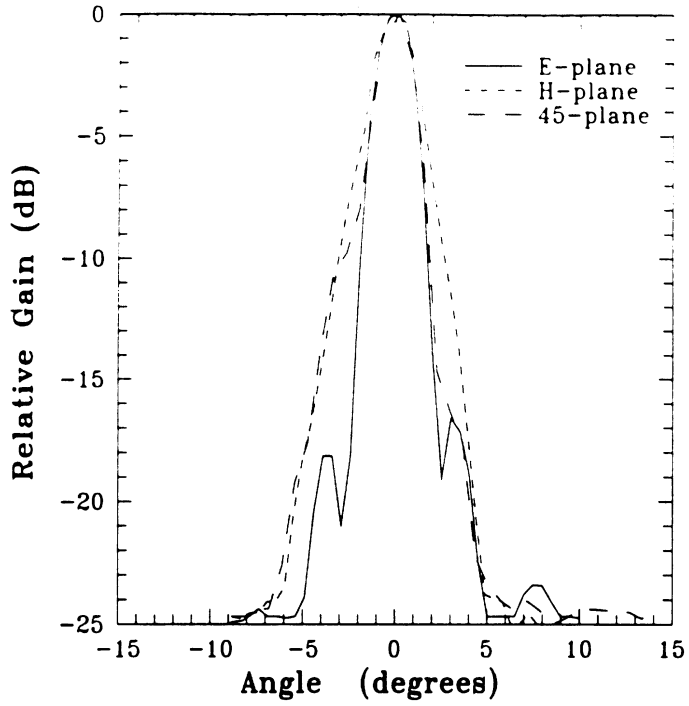


Figure 2.11: Measured reflector patterns at 119 $\mu$m.

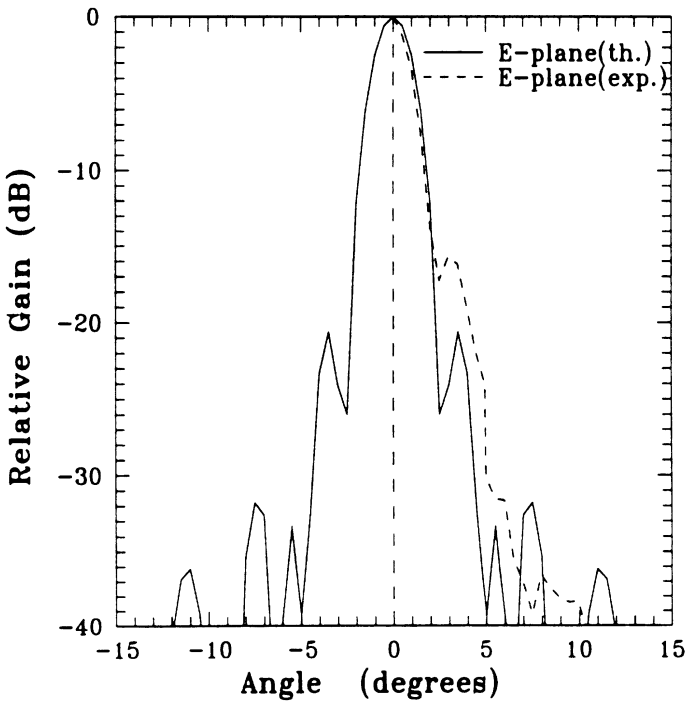


Figure 2.12: Comparison of theoretical and measured E-plane reflector patterns at 119 $\mu$m.

small machined parabolic reflector at 119 $\mu$m showed a directivity around 37 dB, and confirmed the theoretically predicted reflector E-plane patterns to the -15 dB level, in spite of the double-dipoles being poorly aligned to the backing ground-plane. This makes the double-dipole antenna ideally suited as a submillimeter-wave feed for high resolution tracking or for long focal length cassegrain antenna systems

# CHAPTER III

# EXTENDED HEMISPHERICAL AND ELLIPTICAL DIELECTRIC LENSES

In this chapter the far-field patterns and Gaussian-beam coupling efficiencies are investigated for extended hemispherical lenses with varying extension lengths (see Chapter 1). Lenses with two types of dielectric constant, silicon ($\epsilon_r$=11.7) and fused quartz ($\epsilon_r$=3.8), are analyzed. The radiation patterns of the lens are found by using ray-tracing inside the dielectric lens and electric and magnetic field integration on the spherical dielectric surface.

The planar feed antenna chosen for the analysis is a double-slot antenna. If the dimensions are chosen properly, the double-slot antenna will launch a nearly perfect fundamental Gaussian-beam into the dielectric lens. Therefore, a simple way to measure the abberations introduced by the extended hemispherical lens is to measure the pattern-to-pattern coupling value of the far-field patterns of the lens to a fundamental Gaussian-beam (Gaussicity). The total power coupling into the antenna, termed the Gaussian-coupling efficiency, is the product of the Gaussicity and all the losses (reflection loss, dielectric loss, backside loss, etc.). The double-slot antenna design was chosen since it is experimentally realizable, and an experimental verification of the theory is presented in this thesis. Since the properties of the main

beam are determined by the dielectric lens, and to a lesser extent by the feed antenna, the results of this work are equally valid for slot-ring, double-dipole, log-periodic and spiral feed antennas.

## 3.1 Synthesis of an Elliptical Lens

An elliptical lens can be synthesized from an extended hemispherical lens by carefully choosing a particular extension length. The analysis is done in two dimensions since the geometry is rotationally symmetric. The defining equation for an ellipse is:

$$(\frac{x}{a})^2 + (\frac{y}{b})^2 = 1 \tag{3.1}$$

where the foci are at $\pm c$ and $c = \sqrt{b^2 - a^2}$. It is also known from optics that for a given index of refraction n, the eccentricity of the ellipse such that the geometric focus becomes the optical focus is [39]:

$$\text{eccentricity} = \frac{\sqrt{b^2 - a^2}}{b} = \frac{1}{n} \tag{3.2}$$

From this one can derive that:

$$b = \frac{a}{\sqrt{1 - \frac{1}{n^2}}} \tag{3.3}$$

$$c = \frac{b}{n} \tag{3.4}$$

A hemisphere of unit radius is defined by $x^2 + y^2 = 1$, choosing only positive y-values. The distance from the circular tip of an extended hemisphere to the end of its extension is equal to $1 + L$, where L is the extension length. The distance from the tip of an ellipse to its more distant focus is equal to $b + c$. These distances must be equal in order to superimpose the two lenses, which yields $L = b + c - 1$. The ellipse must be shifted down by a value $y_0 = L - c$ so that the focus of the ellipse has the same coordinates as the focus of the extended hemisphere. Thus given the index

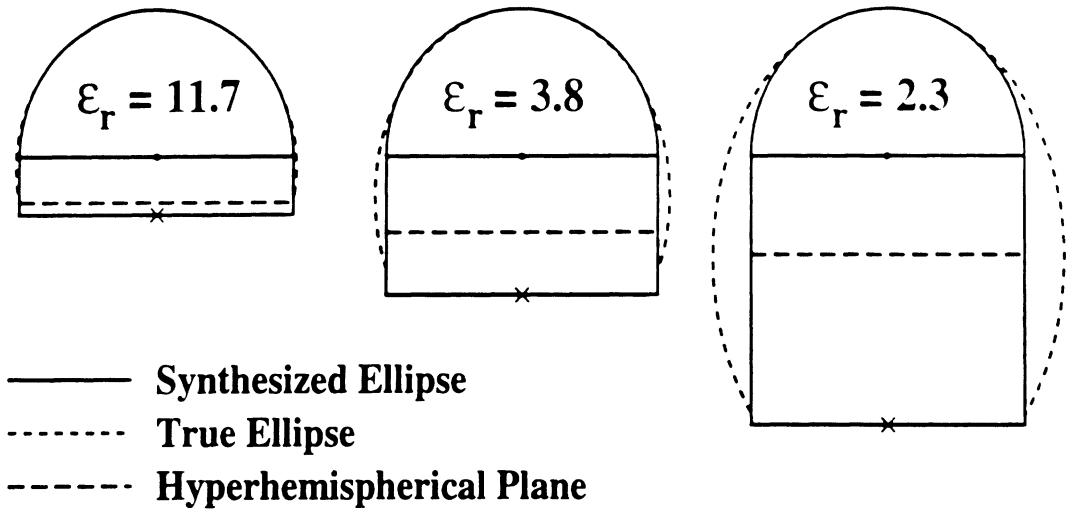


Figure 3.1: The synthesis of an elliptical lens from a hyperhemispherical lens and planar wafers. The extended hemisphere is a very good geometrical approximation to an elliptical lens at high dielectric constants.

of refraction, the parameter b is varied until the extended hemisphere appears to have the closest geometrical match to an ellipse (b will lie within a narrow range no matter how this is defined). This has been done for a dielectric constant of $\epsilon_r$ =2.3 (polyethylene), 4.0 (quartz), and 11.7 (silicon), and is shown in Fig. 3.1. It is obvious that the higher dielectric constant yields a more exact geometrical approximation. For a silicon lens, the fitted ellipse values are a=1.03 and b=1.07691, and this yields an extension length of L=2670 $\mu$m for a 13.7 mm diameter lens. There are many ways to synthesize an ellipse [13] and it will be shown later that the synthesized silicon ellipse presented above is a very good appoximation to a true elliptical lens.

## 3.2 Theoretical Analysis

A double-slot antenna is chosen as the feed antenna for the extended hemispherical lenses. Double-slot antennas have been previously used by Kerr et al. in a 100 GHz receiver [44] and Zmudzinas in a 492 GHz SIS receiver on a quartz hyperhemispherical lens [87]. Recently, Zmudzinas has developed a SIS receiver with

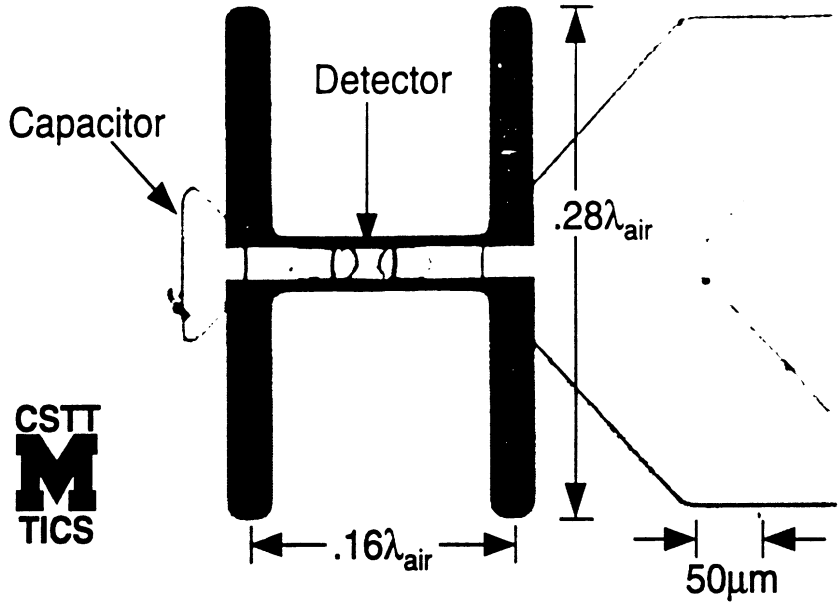


(a)

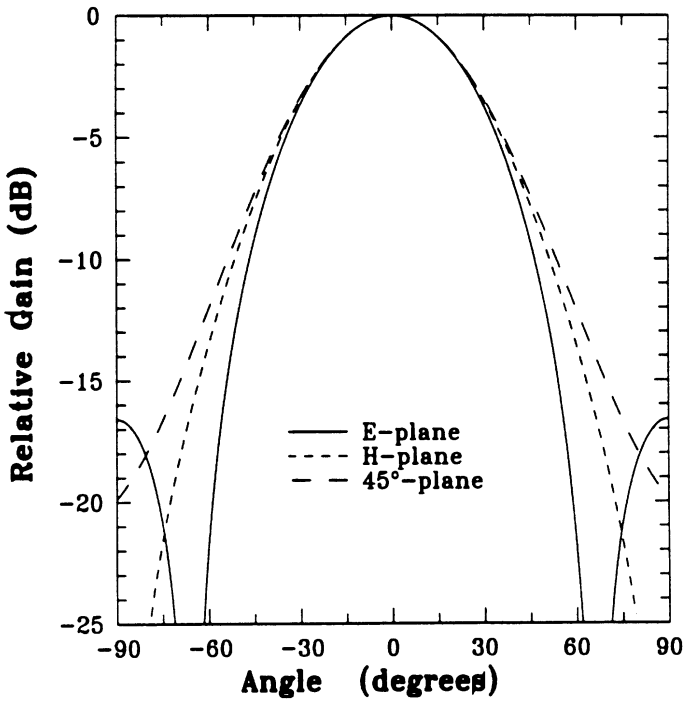


(b)

Figure 3.2: The double-slot antenna (a) and its radiation patterns into a silicon ($\epsilon_r$=11.7) dielectric (b). The cross-polarization level is below -30 dB in the 45°-plane.

a double-slot antenna on a silicon hyperhemispherical lens [55]. The double-slot antenna patterns are calculated assuming a sinusoidal magnetic current distribution on the slot and using an array factor in the E-plane direction [23]. The double slots lie in the x-z plane, and the slots point in the direction of the z-axis. The wavelength of the sinusoidal current distribution in the slot is approximately the geometric mean wavelength [47] given by $\lambda_m = \lambda_0/\sqrt{\epsilon_m}$ and $\epsilon_m = (1+\epsilon_r)/2$. The current in the slot is given by :

$$I = I_{max}\sin[k_m(l-|z|)], \qquad -l \le z \le l, \qquad 2l_{max} = 0.28\lambda_{air} \tag{3.5}$$

where $k_m = 2\pi/\lambda_m$. The corresponding normalized H-plane field pattern is:

$$\frac{\sin\theta[\cos(k_e l\cos\theta) - \cos(k_m l)]}{k_m^2 - k_e^2\cos^2\theta} \tag{3.6}$$

where $k_e = k_{diel} = 2\pi/\lambda_{diel}$ for the dielectric side, $k_e = 2\pi/\lambda_{air}$ for the air side, and $\theta$ is the angle with respect to the z-axis. The element pattern is a constant in the E-plane. The E-plane array factor is given by:

$$\cos(k_e\frac{d}{2}\sin\theta\cos\phi) \tag{3.7}$$

where $\phi$ is the angle from the x-axis in the x-y plane, $k_e$ is defined as above, and d is the spacing between the two slots.

Figure 3.2 shows the calculated radiation patterns at 246 GHz of a double-slot antenna with length $2l = 0.28\lambda_{air}$ and spacing $d = 0.16\lambda_{air}$ into a dielectric with a relative dielectric constant of $\epsilon_r = 11.7$. The double-slot antenna results in symmetrical patterns in the infinite dielectric half space with a -10 dB beamwidth of around 48° and a cross-polarization level lower than -30 dB in the 45°-plane (using Ludwig's third definition of cross-pol [52, 18]). The phase is constant across the main-beam, and the power radiated in the main-beam illuminates the whole spherical

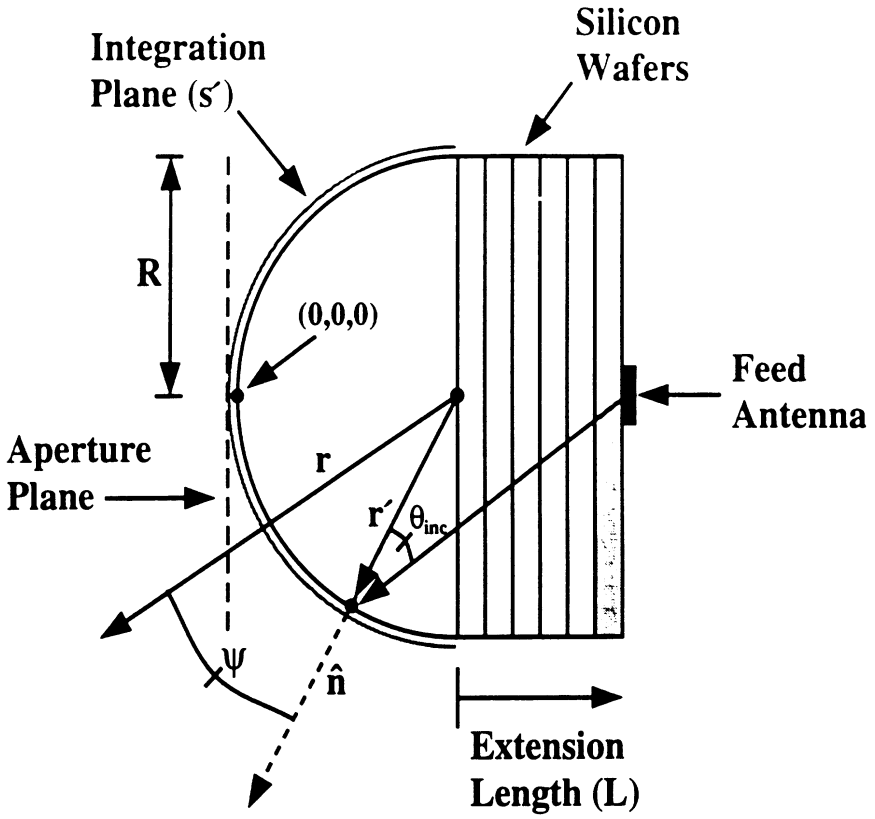


Figure 3.3: The extended hemispherical lens and the ray-tracing/field-integration technique.

surface of the extended hemispherical lenses considered in this thesis. The pattern has an almost perfect fundamental Gaussian distribution (98%), and therefore the abberations introduced by the extended hemispherical lens can be characterized by the amount which the Gaussicity drops from this 98% value. The patterns radiated to the air-side are broader with a -10 dB beamwidth of 70° in the H-plane and a nearly uniform E-plane, and contain 9.0% of the radiated power.

The radiation patterns from the extended hemispherical lenses are computed using a ray-tracing technique [18]. The double-slot antenna patterns into the dielectric are used to calculate the distribution of the electric and magnetic fields across the spherical surface of the extended hemispherical lenses (Fig. 3.3). It is important to note that this analysis is not limited to double-slot antennas and is applicable

to any planar antenna designed to yield similar patterns in the dielectric: for example, the slot-ring, double-dipole and spiral/log-periodic antennas. For a given ray, the fields are decomposed into parallel/perpendicular components at the lens/air interface, and the appropriate transmission formulas are used for each mode [8]:

$$\Gamma_{\|} = \frac{n\sqrt{1 - n^2 \sin^2\theta_i} - \cos\theta_i}{n\sqrt{1 - n^2 \sin^2\theta_i} + \cos\theta_i} \tag{3.8}$$

$$\tau_{\|} = (1 + \Gamma_{\|}) \frac{\cos\theta_i}{\sqrt{1 - n^2 \sin^2\theta_i}} \tag{3.9}$$

$$\Gamma_{\perp} = \frac{n\cos\theta_i - \sqrt{1 - n^2 \sin^2\theta_i}}{n\cos\theta_i + \sqrt{1 - n^2 \sin^2\theta_i}} \tag{3.10}$$

$$\tau_{\perp} = 1 + \Gamma_{\perp} \tag{3.11}$$

where n is the dielectric constant, $\theta_i$ is the angle of incidence from the normal to the spherical lens (Fig. 3.3), and $\Gamma$ and $\tau$ are the reflection and transmission coefficients for the parallel ($\|$) and perpendicular ($\perp$) polarizations. Once the electric and magnetic fields have been found, equivalent electric and magnetic current densities [8] are calculated just outside the spherical surface using:

$$\mathbf{J_S} = \hat{n} \times \mathbf{H} \tag{3.12}$$

$$\mathbf{M_S} = -\hat{n} \times \mathbf{E} \tag{3.13}$$

where $\hat{n}$ is the normal to the interface, and $\hat{n} = \hat{a}_r$ when the origin of the coordinate system is defined to be the center of the spherical surface. In the far-field, the transverse electric field is equal to:

$$\mathbf{E}_\theta \cong -\frac{jke^{-jkr}}{4\pi r}(\mathbf{L}_\phi + \eta \mathbf{N}_\theta) \tag{3.14}$$

$$\mathbf{E}_\phi \cong +\frac{jke^{-jkr}}{4\pi r}(\mathbf{L}_\theta - \eta \mathbf{N}_\phi) \tag{3.15}$$

where $\mathbf{N}$ and $\mathbf{L}$ are defined by:

$$\mathbf{N} = \iint_S \mathbf{J_S} e^{jkr'\cos\psi} ds' \tag{3.16}$$

$$\mathbf{L} = \iint_S \mathbf{M_S} e^{jkr'\cos\psi} ds' \tag{3.17}$$

where $s'$ is the closed surface just outside the lens, $r'$ is the distance from the center of the sphere to the equivalent electric and magnetic currents, $r$ is the distance from the center of the sphere to the far-field point, and $\psi$ is the angle between $r$ and $r'$. The integrals are evaluated with respect to a coordinate system having its origin at the tip of the lens. Thus, in subsequent calculations, the far-field phase, or the near-field radius of curvature, is always referenced to the tip of the lens.

## 3.3 Case 1: Silicon

### 3.3.1 Theoretical Results

The computed E and H-plane power patterns and the phases of the electric field in the E-plane of a 13.7 mm diameter silicon ($\epsilon_r = 11.7$) lens fed by a double-slot antenna at 246 GHz are shown for extension lengths of 1600 $\mu$m, 1800 $\mu$m, 2000 $\mu$m, 2200 $\mu$m, 2400 $\mu$m, 2600 $\mu$m, 2800 $\mu$m, and 3000 $\mu$m (Fig. 3.4). It is seen that the patterns become progressively narrower resulting in higher directivity up to 2600 $\mu$m and then the mainlobe widens and the sidelobe levels begin to increase. It is important to note that the phase of the field is not constant in the mainlobe except around the synthesized elliptical position (determined to be L = 2670 $\mu$m). This is seen on the 2600 $\mu$m plot where the phase is nearly constant in the mainlobe and then shifts 180° in the first sidelobe. The corresponding peak directivity and the Gaussicity (pattern coupling efficiency; see App. A) as a function of the extension length are shown in Figure 3.5. The Gaussicity is computed using an overlap integral between

the far-field patterns and the far-field Gaussian-beam expression (see Appendix A). The directivity has a broad peak of 30.2 dB centered at $L_{pk}$ = 2550 $\mu$m and remains within 1.0 dB of the peak between 2400 $\mu$m and 2800 $\mu$m. The corresponding aperture efficiency (coupling to a plane wave) peaks at 84% and is above 68% between 2400 $\mu$m and 2800 $\mu$m. This peak position agrees well with Büttgenbach's formulation on the diffraction-limit of a lens (see [13] for more detail). In the far-field, the decrease in Gaussicity at the larger extension lengths can be interpreted as the result of the formation of out-of-phase sidelobes whose level progressively increases as the extension length is increased. It is seen that the Gaussicity is very high up to 2200 $\mu$m (above 95%) and drops to 88-86% at the peak directivity and synthesized elliptical positions.

The near-field waist and radius of curvature are found from an inverse Fourier transform of the far-field Gaussian-beam [18] (Fig. 3.6). These are referenced to the aperture plane at the tip of the lens (Fig. 3.3). As expected, the radius of curvature is infinity at the synthesized elliptical position (L=2670 $\mu$m) and changes sign immediately afterwards. This means that the synthesized elliptical lens is a good approximation to a true elliptical lens and couples best to a Gaussian-beam at its minimum waist. The Gaussian-beam radius of curvature approaches the lens radius (6.858 mm) when the extension length is small, as expected. The beam waist is nearly constant at 5.6$\pm$0.3 mm for extension lengths between 1000 $\mu$m and 2700 $\mu$m and 5.8$\pm$0.1 mm between 1800 $\mu$m and 2300 $\mu$m. It is mainly the radius of curvature that is changing from -13 mm to -$\infty$ between 1000 $\mu$m and 2700 $\mu$m. Therefore, the converging Gaussian-beam must be very well characterized on the lens aperture for optimal Gaussian-coupling efficiency.

In order to gain a more intuitive understanding of the optimal radius of cur-

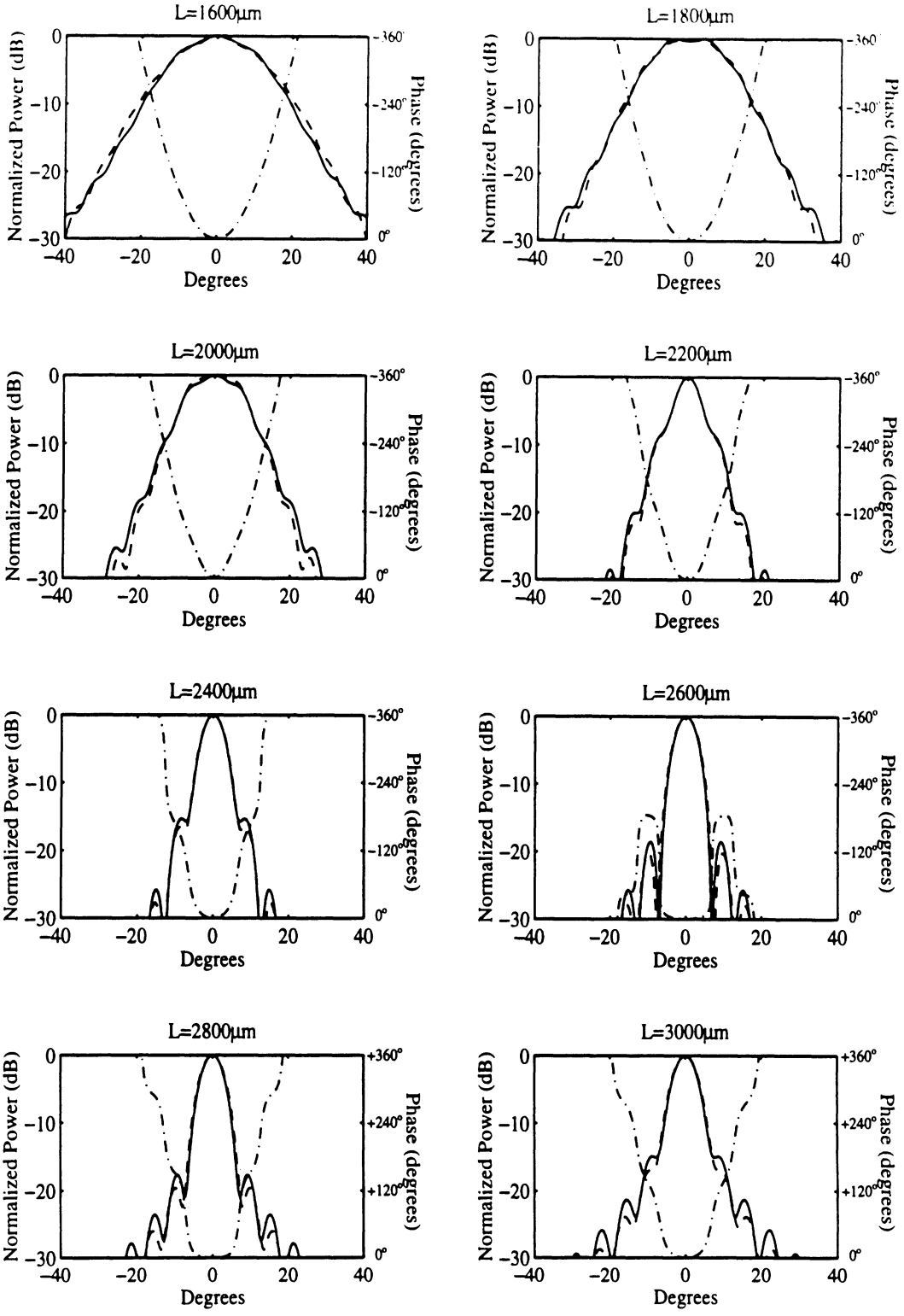


Figure 3.4: E and H-Plane power patterns and phase in the E-plane at 246 GHz for extension lengths of 1600 $\mu$m, 1800 $\mu$m, 2000 $\mu$m, 2200 $\mu$m, 2400 $\mu$m, 2600 $\mu$m, 2800 $\mu$m, and 3000 $\mu$m ($\epsilon_r$=11.7). The ($- \cdot - \cdot -$) line corresponds to the phase.

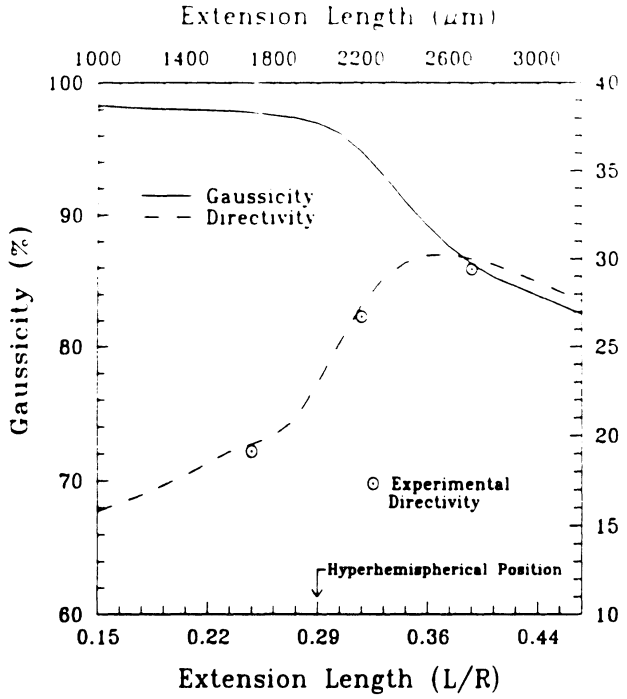


Figure 3.5: Directivity and maximum Gaussicity (pattern coupling efficiency) as a function of extension length at 246 GHz ($\epsilon_r$=11.7).

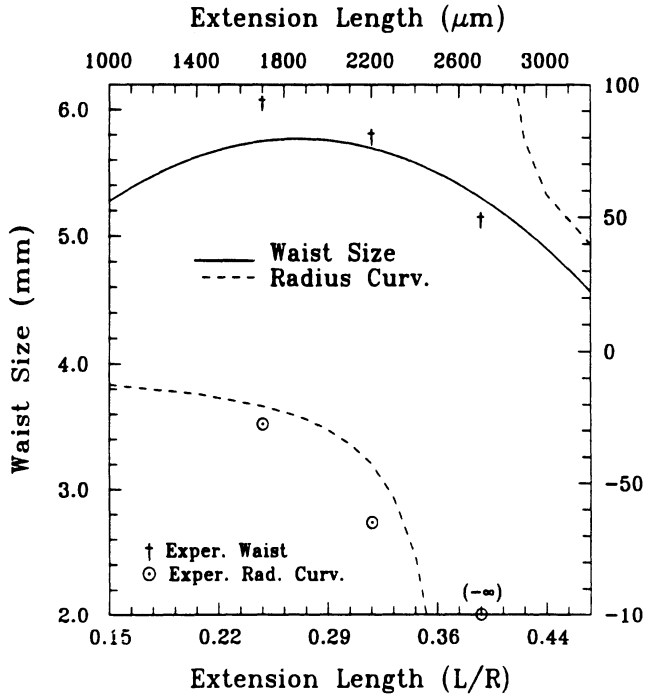


Figure 3.6: Waist and radius of curvature as a function of the extension length at 246 GHz. The dots and crosses indicate values obtained from the experimental set-up ($\epsilon_r$=11.7).

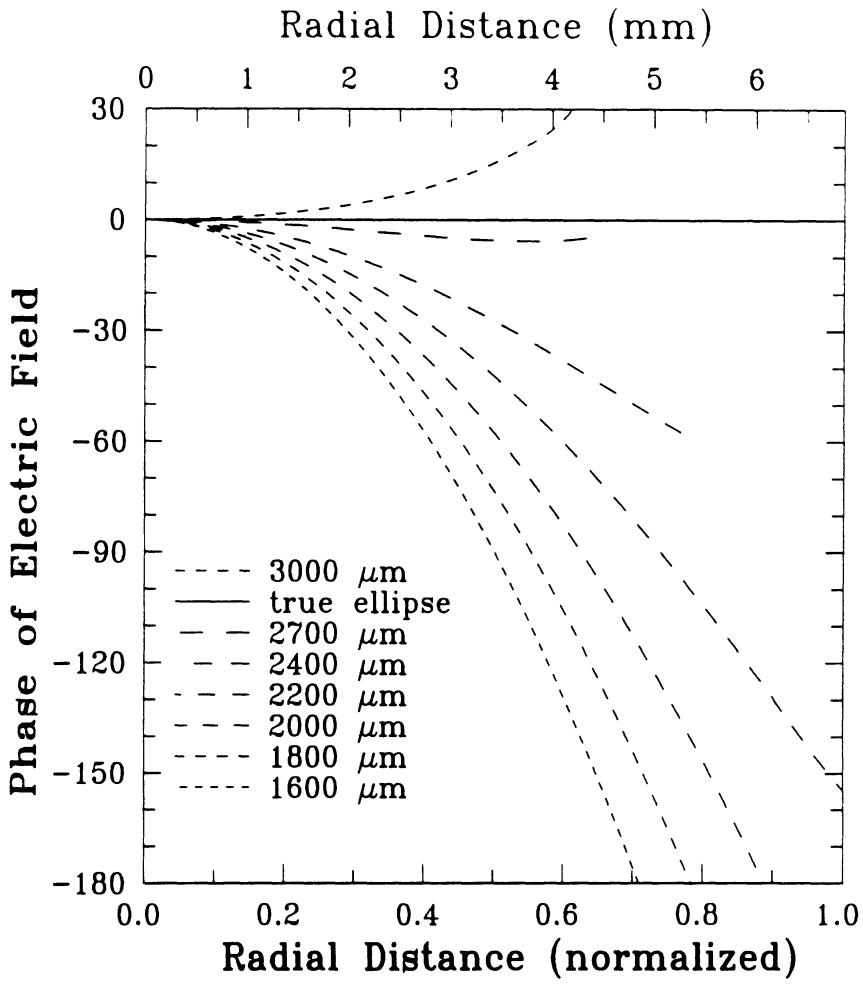


Figure 3.7: Phase of the aperture electric field at 246GHz for extended hemispherical lenses with different extension lengths with the double-slot antenna as the feed ($\epsilon_r$=11.7).

vature, the phase of the electric field on the aperture plane is presented in Fig. 3.7 for the lens system at 246 GHz. The phase is calculated using a ray-optics approach all the way to the aperture-plane. This method has proven to result in a caustic with the extended lens system and is not used for far-field pattern and Gaussian-beam calculations (a caustic is a region where an infinite number of rays converge together and therefore results in a singularity in the field). However, the method does yield a physical understanding of the problem. The phase of the electric fields on the planar aperture is seen to follow a near quadratic behaviour with varying curvature depending on the extension length. For larger extension lengths (L=2200 $\mu$m and above) the phase is plotted up to the caustic region. For low extension lengths, the aperture fields extend significantly beyond the diameter of the lens due to the weak refraction of the wide angle rays, and this contributes to the high Gaussicity (since the fields are not truncated). This is not shown in Figure 3.7 since the phase is only plotted to 180°. At L=2700 $\mu$m (just near the synthesized elliptical postion) the phase is nearly constant, and then begins to increase positively for increasing extension length.

A similar analysis of a 13.7 mm diameter lens was performed at 100 GHz and 500 GHz, assuming the same radiation patterns of the feed antenna. Figure 3.8 shows the patterns and phases for extension lengths of 1600 $\mu$m, 1800 $\mu$m, 2000 $\mu$m, 2200 $\mu$m, 2400 $\mu$m, 2600 $\mu$m, 2800 $\mu$m, and 3000 $\mu$m at 500 GHz. The directivity and Gaussicity calculations at 100 GHz, 246 GHz and 500 GHz are shown in Figure 3.9. The corresponding waists and radii of curvature are shown in Figure 3.10. At 100 GHz, the peak in the directivity curve occurs at 2480 $\mu$m and is very broad. The corresponding Gaussicity is very smooth with a drop of 10% at the synthesized elliptical position. On the other hand, at 500 GHz, the directivity curve shows a dis-

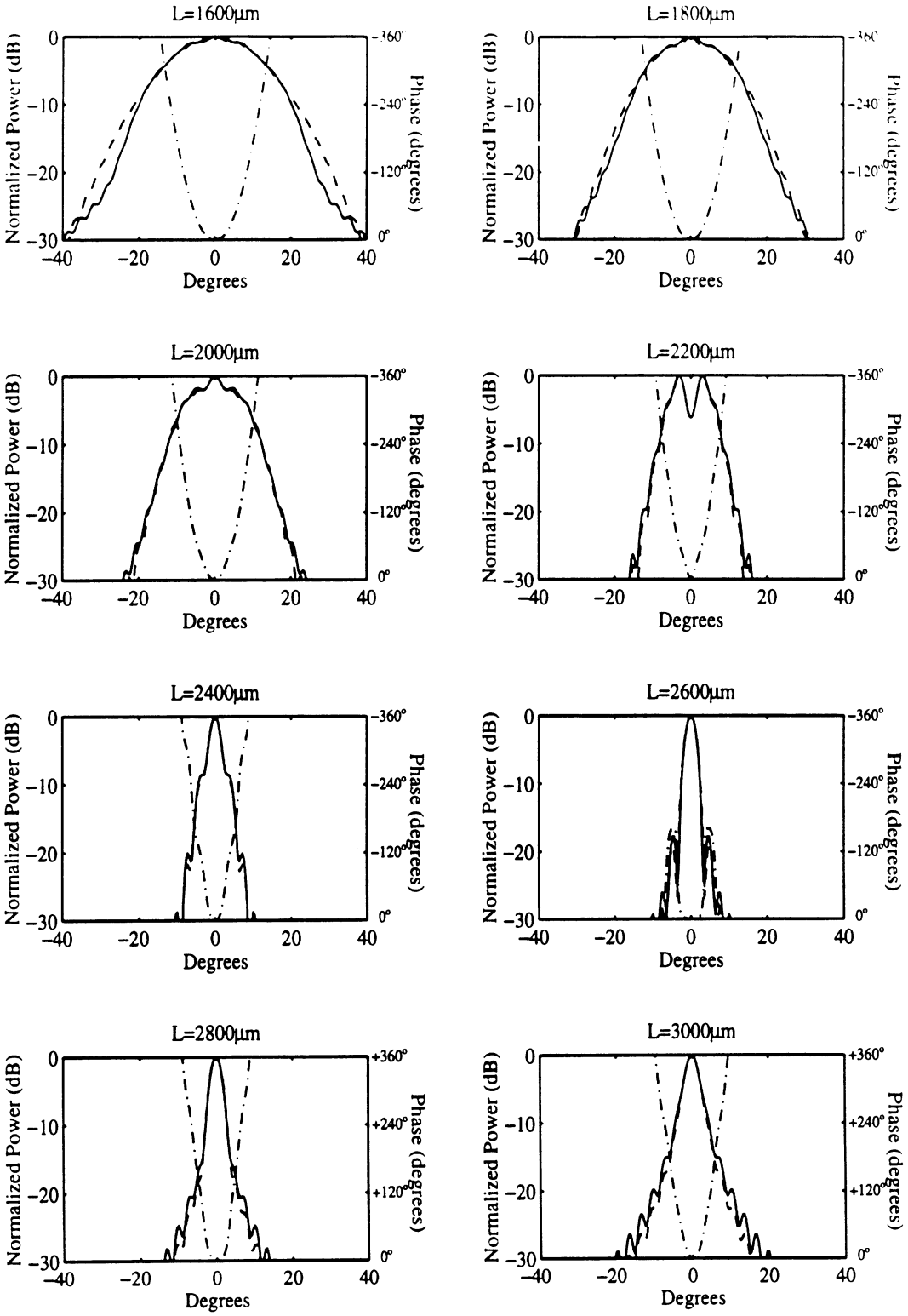


Figure 3.8: E and H-Plane power patterns and phase in the E-plane at 500 GHz for extension lengths of 1600 $\mu$m, 1800 $\mu$m, 2000 $\mu$m, 2200 $\mu$m, 2400 $\mu$m, 2600 $\mu$m, 2800 $\mu$m, and 3000 $\mu$m ($\epsilon_r$=11.7) The ($- \cdot - \cdot -$) line corresponds to the phase.

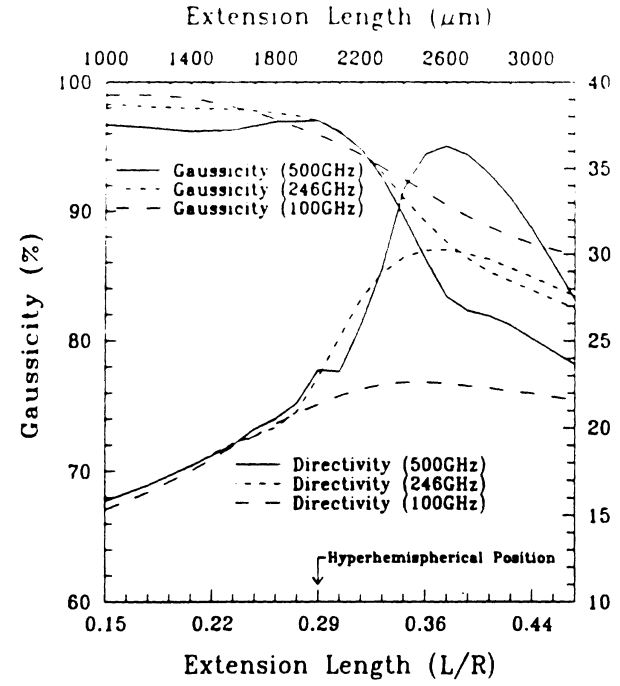


Figure 3.9: Directivity and maximum Gaussicity (pattern coupling efficiency) as a function of extension length at 100 GHz, 246 GHz, and 500 GHz ($\epsilon_r$=11.7).

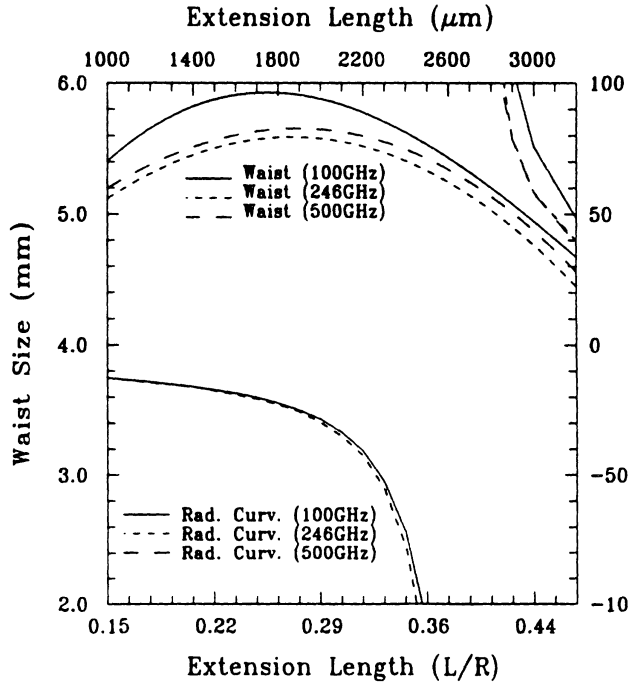


Figure 3.10: Waist and radius of curvature as a function of extension length at 100 GHz, 246 GHz, and 500 GHz ($\epsilon_r$=11.7).

tinct peak of 36.3 dB centered at 2600 $\mu$m (with a corresponding aperture efficiency of 72%) and drops by 0.5 dB at the synthesized elliptical position. This position agrees well with Büttgenbach's diffraction method (see [13] for more detail). Note that at higher frequencies, the peak directivity is closer to the synthesized elliptical position, which is the result of the geometrical optics approximation becoming more accurate. The Gaussicity peaks at 500 GHz at the hyperhemispherical position of 2000 $\mu$m with a value of 97% and then drops to 82% at the 2600 $\mu$m-2700 $\mu$m position. Again, as the frequency increases, the ray-optics approximation becomes more valid, and this explains the peak in Gaussicity at the hyperhemispherical position.

The directivity and Gaussicity are calculated for a true elliptical lens using the same approach for the extended hemispherical lens at 246 GHz. The true elliptical lens is defined such that the minor axis (perpendicular to boresight) is equal to the radius of the extended hemispherical lens, so that the physical area on the aperture plane is the same for both lenses. The E and H-plane mainlobes are slightly narrower than those of the synthesized elliptical lens and have 0.5 dB higher sidelobes. The directivity is 30.6 dB which is 0.6 dB higher than the synthesized ellipse. The elliptical lens Gaussicity is 88% and is the same to within $\pm 1\%$ for the synthesized elliptical lens. The corresponding minimum waist at the aperture plane is 5.6 mm (the radius of curvature is infinite, of course).

### 3.3.2 Reflection Loss Calculations

The ray-tracing technique presented earlier (Sec. 3.2) also results in a full characterization of the reflection loss at the lens-air interface as a function of the extension length (Figure 3.11). The reflection loss is calculated by using equations 8 and 10 and integrating the reflected power over the entire surface of the lens.

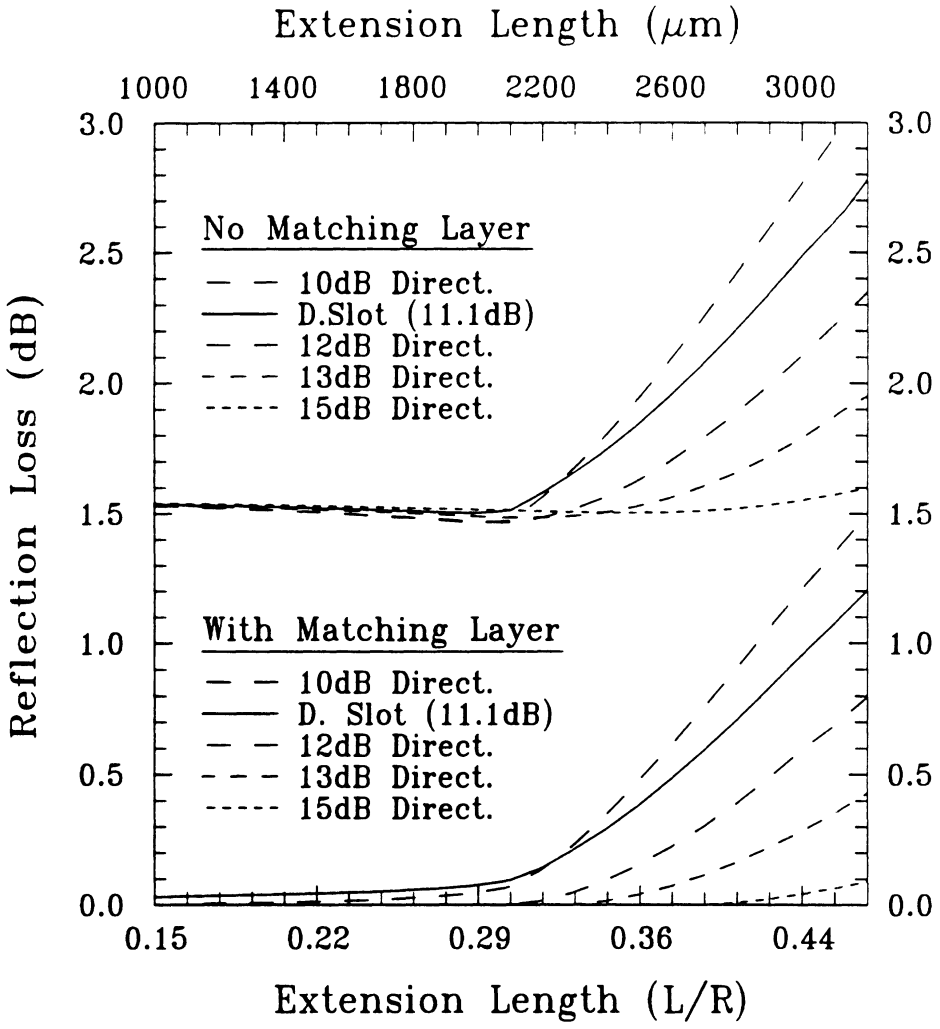


Figure 3.11: Reflection loss at the lens/air interface as a function of the extension length for different feed antenna directivities with and without a matching layer ($\epsilon_r$=11.7).

At low extension lengths, the calculated loss is 1.52 dB which is close to the 1.55 dB predicted from simple transmission-line theory (between silicon and air). The reflection loss increases to 2.1 dB at the synthesized elliptical position (L=2670 $\mu$m) due to the power loss from the total internal reflection of wide angle rays (above 65°). The Gaussian-coupling efficiency of the extended hemispherical system must include the reflection loss to result in a complete characterization of the system. This results in an *additional* decrease of 13% in the Gaussian-coupling efficiency at the synthesized elliptical positions compared to the Gaussian-coupling efficiency at the hyperhemispherical position. The calculated reflection loss at the synthesized elliptical position is 1.8 dB for an antenna with a symmetrical pattern and a 10 dB-beamwidth of 46° (corresponding to a directivity of 12 dB inside the dielectric lens) and a nearly constant 1.52 dB for antennas with a 10 dB-beamwidth of 40° and 31° (corresponding to a directivity of 13 dB and 15 dB). This means that it is advantageous to use a high gain antenna for a feed into the extended hemispherical lens. This is important at high frequencies (above 500 GHz) where it may be difficult to manufacture an accurate matching layer for the silicon lens. While it is not known accurately, it is expected that the spiral antenna [13] and log-periodic antenna [19] have a pattern directivity into the lens of around 12 dB. As expected, the calculated reflection loss of an elliptical lens is nearly equal to the reflection loss at the sythesized elliptical position.

Figure 3.11 also includes the reflection loss using a $\lambda_m/4$ matching cap layer with dielectric constant equal to $\sqrt{\epsilon_{\text{lens}}}$. This was calculated by expanding the ray-tracing method of Section 3.2 to consider multiple reflections in the matching-cap layer (decomposing into appropriate polarizations at each bounce). The reflection loss for the double-slot antenna (directivity=11.1 dB) is nearly zero up to the hyper-

hemispherical position and increases to 0.6 dB at the synthesized elliptical position. The radiation patterns and the directivities remain essentially the same with the matching cap layer. As expected, the reflection loss for the higher directivity antennas are lower with a loss of 0.3 dB, 0.1 dB, and zero for the 12 dB, 13 dB, and 15 dB pattern directivities at the synthesized elliptical position. No attempt is made to design an optimum matching layer (i.e. non-uniform thickness) for the higher extension lengths.

### 3.3.3 Gaussicity vs. Frequency

A comparison of the directivity and Gaussicity between the true elliptical lens, the synthesized elliptical lens, and an extended hemispherical lens at peak directivity position for 100 GHz-1 THz is shown in Fig. 3.12. The true elliptical lens has a constant Gaussicity of 88% and a quadratic increase in the directivity, as expected from ray-optics calculations. The directivity of the synthesized elliptical lens shows a 1.2 dB drop compared to the elliptical lens at 1 THz due to the residual phase error on the planar aperture. The Gaussicity drops from about 90% at 100 GHz to 78% at 1 THz due to the same effect. As was seen in Fig. 3.9 at 246 GHz and 500 GHz, there exists a distinct peak in the directivity at a specific extension length ($L_{pk}$). Figure 3.13 shows that $L_{pk}$ asymptotically approaches the synthesized elliptical position with increasing radius/wavelength (or increasing frequency for a constant radius). The peak directivity is slightly higher than the synthesized elliptical directivity and is nearly the same above 500 GHz. The Gaussicities for peak directivity positions are the same as those of the synthesized elliptical position to within $\pm 1\%$ above 200 GHz. At 100 GHz, the peak directivity position is close to the hyperhemispherical position, and therefore results in a slightly larger Gaussicity.

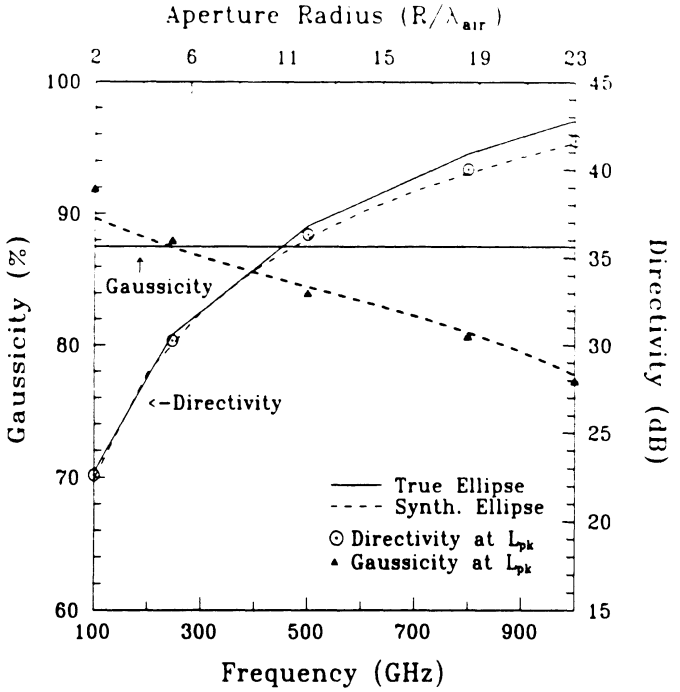


Figure 3.12: Directivity and maximum Gaussicity (pattern coupling efficiency) as a function of frequency (or lens radius) for a true elliptical lens, a synthesized elliptical lens, and an extended hemispherical lens at peak directivity position ($L_{pk}$) for a silicon lens ($\epsilon_r$=11.7).

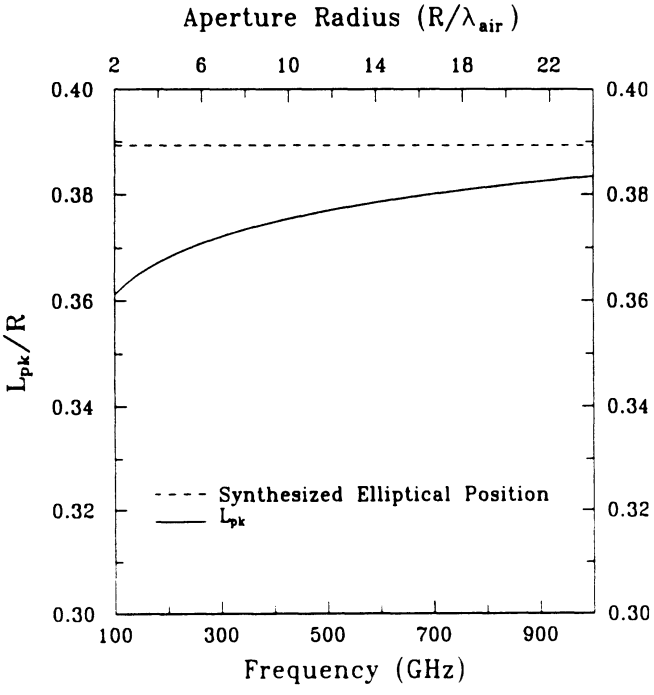


Figure 3.13: Extension length for peak directivity versus frequency (or R/$\lambda$) for a silicon lens ($\epsilon_r$=11.7).

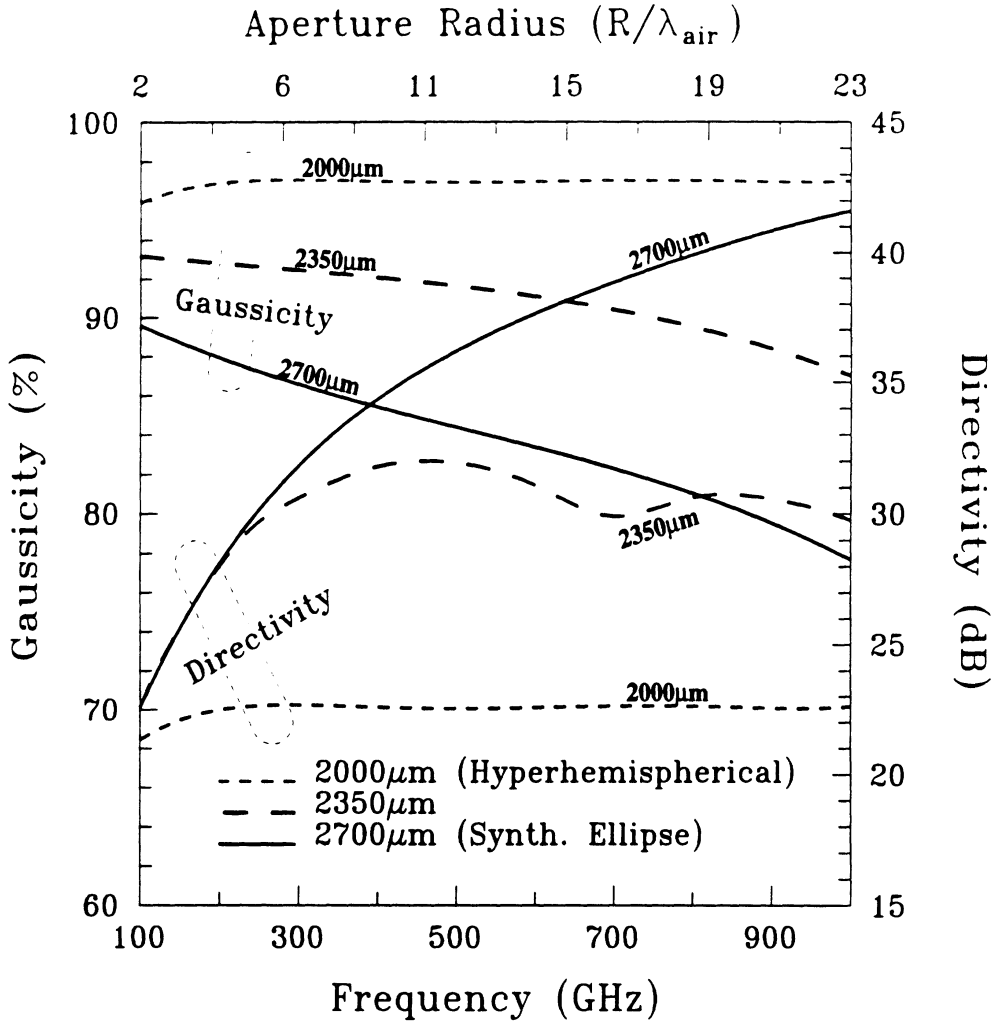


Figure 3.14: Directivity and Gaussicity (pattern coupling efficiency) as a function of frequency (or lens radius) for an extended hemispherical lens at L=2000 $\mu$m, 2350 $\mu$m, and 2700 $\mu$m ($\epsilon_r$=11.7).

The Gaussicity and directivity for extension lengths of 2000 $\mu$m, 2350 $\mu$m, and 2700 $\mu$m are shown in Figure 3.14. The hyperhemispherical lens results in a constant directivity of 22 dB and a constant Gaussicity of 97%. Notice that the directivity is constant with frequency due to the constant $n^2$ magnification of the hyperhemispherical lens. The Gaussicity at 2350 $\mu$m is slightly lower than the hyperhemispherical lens and the directivity increases to around 30 dB at high frequencies. The Gaussicity at 2700 $\mu$m (close to the synthesized elliptical position) is the lowest of all three positions, but results in the largest directivity. The Gaussicity at the synthesized elliptical position (and at $L_{pk}$) drops to 78% at 1 THz while the Gaussicity for the 2350 $\mu$m position drops to 88% at the same frequency. Although the hyperhemispherical position shows the highest theoretical Gaussicity, it is hard to experimentally achieve this efficiency due to the difficulty in aligning to the strongly converging beams needed at the aperture of the lens (see section 3.5). Thus the region between 2200 $\mu$m and 2400 $\mu$m results in the best compromise between alignment, directivity and Gaussian-coupling efficiency.

Since all the calculations were done in terms of wavelength, Figures 3.12 and 3.14 present universal design curves to predict the performance of extended hemispherical silicon lenses for different diameters when using the same antenna feed patterns. These graphs shows that for high gain systems, a 13.7 mm diameter silicon lens can be used in an extended hemispherical configuration up to 1 THz without a significant drop in the Gaussicity. For a matched load, the Gaussian-coupling efficiency is found by multiplying the Gaussicity presented above by the reflection loss at the lens-air interface (shown in Figure 3.11) and by 91.0% to take into account the power radiated by the double-slot antenna to the back-side (air-side). It is important to note that the reflection loss for higher extension lengths (near $L_{pk}$

and the synthesized elliptical position) will have an *additional* loss of about 0.5 dB (10%) over the hyperhemispherical position (2000 $\mu$m) (for the double-slot antenna).

### 3.3.4 Experimental Results: Patterns

The double-slot antenna presented in section 3.2 was fabricated for 246 GHz measurements using standard photolithographic techniques. All the conducting layers are 2000 Å gold deposited on a high-resistivity (4000$\Omega$ – cm) silicon wafer. A bismuth bolometer is placed in series at the center of the double-slot antenna using a coplanar-waveguide transmission line (Fig. 3.2). The series feeding is necessary in order to result in the sum mode of the double-slot antenna. The bolometer is 20 $\mu$m x 15 $\mu$m and is integrated on a 1.2 $\mu$m thick polyimide patch for thermal insulation from the substrate. The measured DC resistance of the bolometer is 60$\Omega$. The left and right ends of the coplanar line are terminated by a polyimide/gold capacitor which acts as an RF short. The center strip of the coplanar waveguide line runs out from the right end to a large pad for DC biasing and low frequency detection. The coplanar waveguide spacing is 15 $\mu$m and the width 10 $\mu$m. This yields a quasi-TEM transmission line impedance of 50$\Omega$ [38]. The measured RF impedance at the bolometer position is $60 + j50\Omega$ on a 4 GHz microwave model, and results in a good match to the bolometer.

Experimental measurements at 246 GHz were performed on a 13.7 mm diameter silicon lens ($\epsilon_r$=11.7) without any type of matching layer and the double-slot antenna as a feed. Three particular values of extension length were chosen for the purpose of experimental verification: 1700 $\mu$m, 2200 $\mu$m, and 2700 $\mu$m. The extension lengths were achieved by adding high-resistivity silicon wafers. These positions were chosen based on their different properties: a phase curvature across their aperture

planes of high, low, and virtually none, respectively; and a radiation pattern that is broad, narrow with nearly no sidelobes, and narrow with low sidelobes, respectively. The position of 2700 $\mu$m represents the extension length where the extended hemispherical lens has effectively synthesized an elliptical lens. The hyperhemispherical position is at 2000 $\mu$m and no measurements were done at this position. However, the 1700 $\mu$m extension has the same features as the 2000 $\mu$m position in terms of Gaussian-coupling efficiency and the small radius of curvature needed to couple well to a Gaussian-beam. No pattern measurements were done on a true elliptical lens.

The patterns were measured at 246 GHz using an 82 GHz Gunn source, and a wideband (220-270 GHz) tripler. The Gunn source was modulated at 1040 Hz, and the output from the bolometer was fed to a lock-in amplifier. Measured patterns at the extension length of 2700 $\mu$m (Fig. 3.15) demonstrate a directivity of 29.4 dB$\pm$0.3dB with relatively low sidelobes (-16 dB). The corresponding aperture efficiency (coupling to a plane wave) is 70%$\pm$5%. Notice that the theoretical analysis predicts a directivity of 29.9 dB (78% aperture efficiency) at the synthesized elliptical position. Good agreement exists between the theoretical and experimental patterns (Fig. 3.16). Measured patterns at 2700 $\mu$m for $\pm$10% of the 246 GHz design frequency result in nearly the same directivity, and therefore the double-slot antenna has good pattern bandwidth. The measured power at broadside is nearly the same from 222-270 GHz, also indicating good impedance bandwidth for the double-slot design. The measured patterns at an extension length of 2200 $\mu$m are slightly broader than the synthesized elliptical lens with a directivity of 26.7 dB$\pm$0.3dB. Again, there is close agreement between theory and experiment (Fig. 3.17). At an extension length of 1700 $\mu$m, the patterns become wide with a peak gain of 19.1 dB$\pm$0.3dB, and it is considerably more difficult to laterally align the feed antenna to the focus, resulting

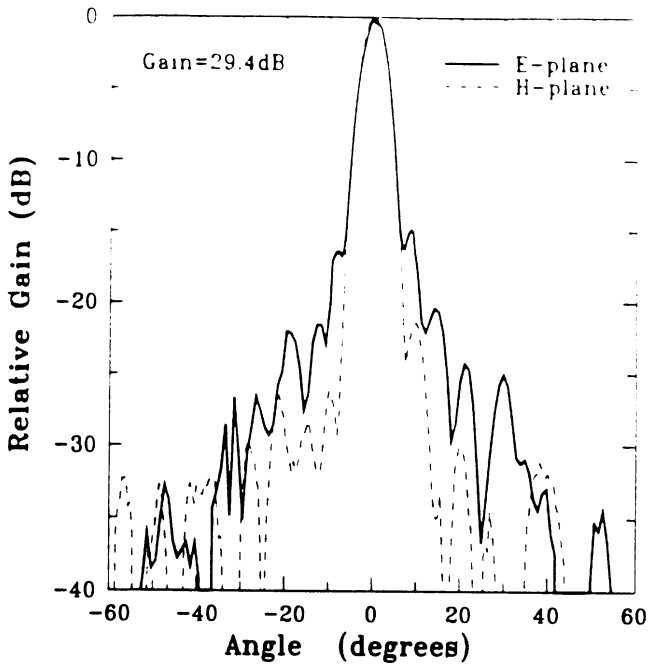


Figure 3.15: Measured patterns for the synthesized elliptical lens (2700 $\mu$m) at 246 GHz. The patterns are diffraction-limited by the size of the aperture. The S/N ratio is better than 40 dB.

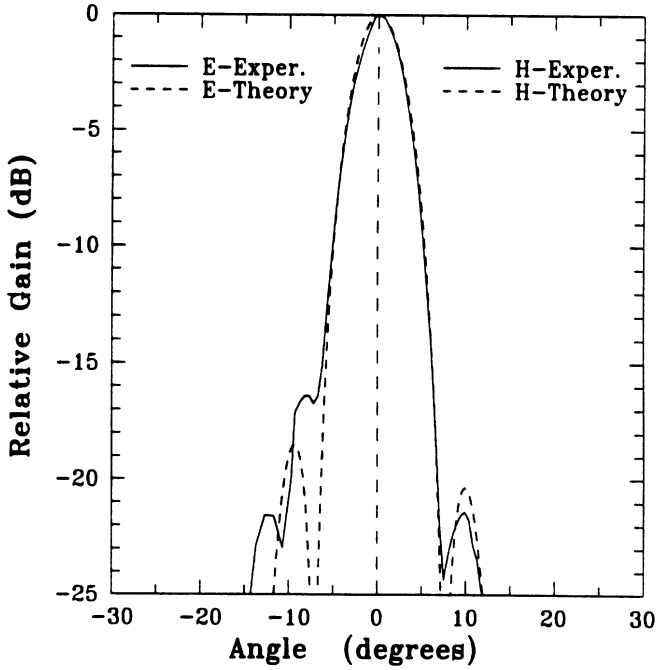


Figure 3.16: Comparison of the calculated patterns versus experiment at 246 GHz for the double-slot antenna on a silicon synthesized elliptical lens (extension length 2700 $\mu$m).

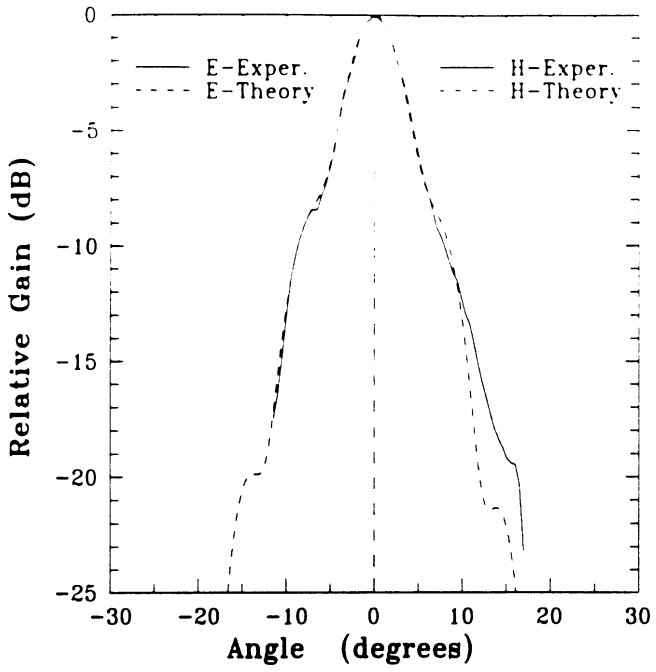


Figure 3.17: Comparison of the calculated patterns versus experiment at 246 GHz for the double-slot antenna on a silicon extended hemispherical lens with 2200 $\mu$m extension length.

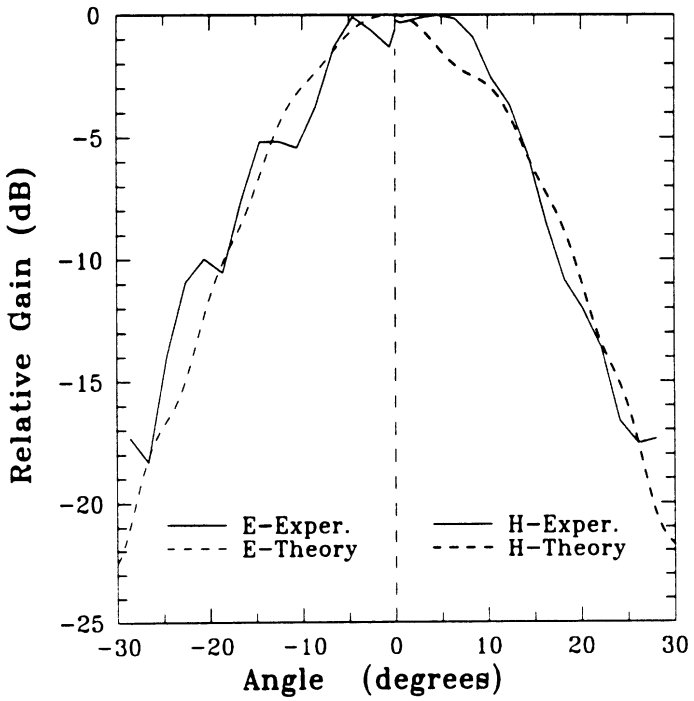


Figure 3.18: Comparison of the calculated patterns versus experiment at 246 GHz for the double-slot antenna on a silicon extended hemispherical lens with 1700 $\mu$m extension length.

in non-symmetric patterns with ripples (Fig. 3.18). As was seen earlier, this wide pattern has no detrimental effect on the coupling efficiency to a converging beam. The ratio of the 246 GHz measured peak received power between the extension lengths of 2700 $\mu$m and 1700 $\mu$m is 10 dB$\pm$0.5dB and this is the same as the difference in the measured directivities (including the effect of the different reflection losses at the lens surface).

### 3.3.5 Experimental Results: Gaussian-Beam Coupling

A Gaussian-beam experiment was performed at 246 GHz with the purpose of coupling all the power radiated by a corrugated horn into the double-slot antenna/lens system. A two-lens quasi-optical system was designed which achieves a wide variety of waist sizes and radii of curvature (Fig. 3.19). The 10-cm Rexolite lenses used were numerically machined using parametric equations and result in no spherical aberrations [42]. The source was a WR-03 corrugated horn having symmetric E, H, and 45° patterns with a computed waist size of $w_0 = 2.1$ mm. The waist can be traced through the lens system using the q-parameters [85]. In Figure 3.19, d1, d2, and d3 are the lens seperation distances, and $f_1$ and $f_2$ are the respective $f/\#$'s ($f/\# =$ f/D, where f is the focal length and D is the diameter of the lens). Care must be taken that the edge illumination of the lens is below the -30 dB level so that the Gaussian-beam does not deform from its ideal shape. The experimental procedure went as follows: the distances d1, d2, and d3 and the $f/\#$'s $f_1$ and $f_2$ are first calculated for maximum coupling between the corrugated horn and the extended hemispherical lens system. Then, the distances d1, d2, and d3 are tuned experimentally to result in peak measured power in the bolometer.

2700 $\mu$m extension length (synthesized ellipse):

An equiphase wavefront is needed for the synthesized ellipse and is obtained at the minimum waist. A quasi-optical system with final values of $d_1$ = 96 mm, $d_2$ = 68 mm, $d_3$ = 312 mm, $f_1/2.0$, and $f_2/1.4$ resulted in a peak received power with a calculated minimum beam-waist of 5.1 mm at the planar lens aperture. The beam waist for optimum Gaussicity calculated from the present theory is 5.2 mm. The final values of d1, d2, and d3 are within ±1 mm of the initially calculated values.

2200 $\mu$m extension length:

A quasi-optical system with final values of $d_1$ = 95 mm, $d_2$ = 122 mm, $d_3$ = 224 mm, $f_1/2.0$, and $f_2/1.4$ resulted in peak received power. The calculated beam waist and radius of curvature were 5.78 mm and −65 mm, respectively. The corresponding minimum waist is 2.8$\lambda$ and is located -35 mm (away from the horn) from the aperture plane. The final values of d1, d2, and d3 are within ±5 mm of the initially calculated values.

1700 $\mu$m extension length:

A quasi-optical system with $d_1$ = 106 mm, $d_2$ = 120 mm, $d_3$ = 86 mm, $f_1/0.9$, and $f_2/2.0$ resulted in peak received power. The calculated beam waist and radius of curvature were 6.07 mm and −27.7 mm, respectively. The corresponding minimum waist is 1.1$\lambda$ (a result of the small radius of curvature necessary at the aperture of the lens). The final values of d1, d2, and d3 differ by as much as ±25 mm from the initially calculated values. We believe that for this extension length, the radius of curvature across the aperture is so strong that the desired aperture field distribution will distort rapidly with misalignments of the feed antenna to the lens. This is commonly seen in optics where it is difficult to align to a lens system with small f/D ratios.

The raw measured powers were 1.03, 1.18 and 1.00 for the 1700 $\mu$m, 2200

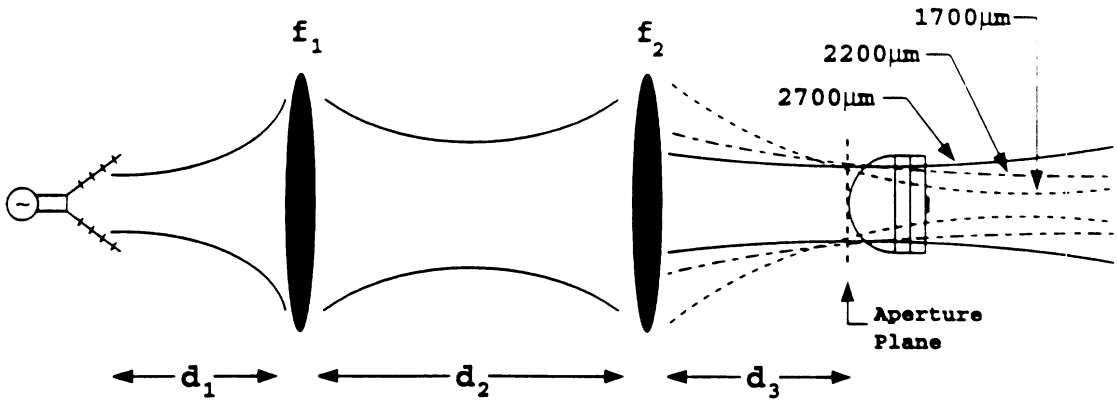


Figure 3.19: The setup for the Gaussian-beam coupling experiment. The waist at the aperture is 5.2-5.9 mm for all three lenses, and only the radii of curvature are different.

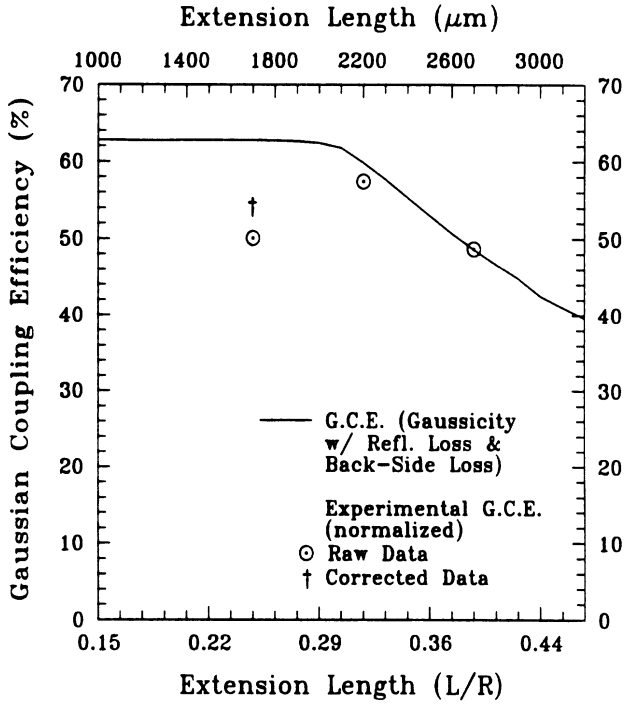


Figure 3.20: Measured and calculated Gaussian-coupling efficiency as a function of extension length. This takes into account reflection at the lens/air interface and power lost to the air side (91%).

$\mu$m, and 2700 $\mu$m positions, respectively. In the experimental setup, the 2200 $\mu$m and 2700 $\mu$m systems used the same set of objective lenses ($f_1/2.0$ and $f_2/1.4$) and therefore have approximately the same reflection and dielectric losses in those lenses. The 1700 $\mu$m experiment required $f_1/0.9$ and $f_2/2.0$ lenses and has approximately an additional 6-10% loss due to the added thickness of the $f/0.9$ lens. The measured power at the 1700 $\mu$m position is therefore multiplied by 1.08 to take into account the excess dielectric loss for the 1700 $\mu$m quasi-optical system, resulting in a corrected power of 1.11 (shown as a cross in Fig. 3.20). The theoretical Gaussicities are multiplied by the different reflection losses at the silicon-air interface (see Fig. 3.11) for the three lens systems, and by the back-side power loss (91%) to yield the actual Gaussian-coupling efficiency. The theoretical Gaussian-coupling efficiencies are presented in Figure 3.20, together with the measured powers which have been normalized to the 2700 $\mu$m position. This position was chosen for the normalization because the experimental waist and radius of curvature at 2700 $\mu$m agree very well with the theoretical values. The normalization is necessary since no absolute power measurements were done at 246 GHz. It is seen that within experimental error, the measured values agree well with the theoretical predictions at extension lengths of 2200 $\mu$m and 2700 $\mu$m. Notice that the 2700 $\mu$m position results in the lowest measured Gaussian-coupling efficiency. Also, the measured Gaussian-coupling efficiency at 2200 $\mu$m is 7% and 18% higher than the measured Gaussian-coupling efficiencies for the 1700 $\mu$m and 2700 $\mu$m positions, respectively. This agrees well with our calculations in section 3.3.3 which state that the 2200 $\mu$m-2400 $\mu$m positions (L/R= 0.32 to 0.35) result in the best compromise between directivity and Gaussian-coupling efficiency.

## 3.4 Case 2: Quartz

Quartz lenses can be hemispherical, hyperhemispherical, or elliptical, and many researchers have placed various antennas on these lenses for receiver applications [70, 83, 41, 12, 87, 76]. In this section, the computed results for an extended hemispherical lens fabricated from fused quartz ($\epsilon_r = 3.8$) are presented.

As was shown in section 3.1, an elliptical lens can be synthesized using a hemispherical lens and attached planar wafers. For the case of a quartz lens with $\epsilon_r = 3.8$ and a diameter of 13.7 mm, the synthesized elliptical position is 6380 $\mu$m (L/R=0.93) behind the hemispherical point, and the hyperhemispherical position is 3520 $\mu$m (L/R=R/n=0.51) behind the hemispherical point.

Again, a double-slot antenna is chosen as the feed antenna for the quartz extended hemispherical lens. Figure 3.21 shows the calculated radiation patterns for a double-slot antenna scaled for $\epsilon_r = 3.8$ with length $l = 0.49\lambda_{air}$ $(0.76\lambda_m)$ and spacing $d = 0.28\lambda_{air}$ $(0.43\lambda_m)$. This design is similar to the one used by Zmudzinas in [87] in which he built a 492 GHz SIS receiver using a double-slot antenna on a quartz hyperhemispherical lens. The double-slot antenna results in symmetrical patterns in the infinite dielectric half space with a corresponding directivity of 11.2 dB and a cross-polarization level lower than -23 dB in the 45°-plane (the directivity quoted is calculated using the pattern radiated in the dielectric only). The patterns radiated to the air-side are broader with a -10 dB beamwidth of 66° in the H-plane and a nearly uniform E-plane, and contain 28.3% of the total radiated power from the double-slot antenna. This is considerable compared to the case of a double-slot antenna on a silicon lens (9% power loss to the air-side). This loss could me eliminated in log-periodic, spiral, and double-dipole antennas with the use of a ground-plane reflector

behind the antenna. For a detailed treatment of log-periodic antennas including their co-polarization and cross-polarization properties, the reader is referred to [48].

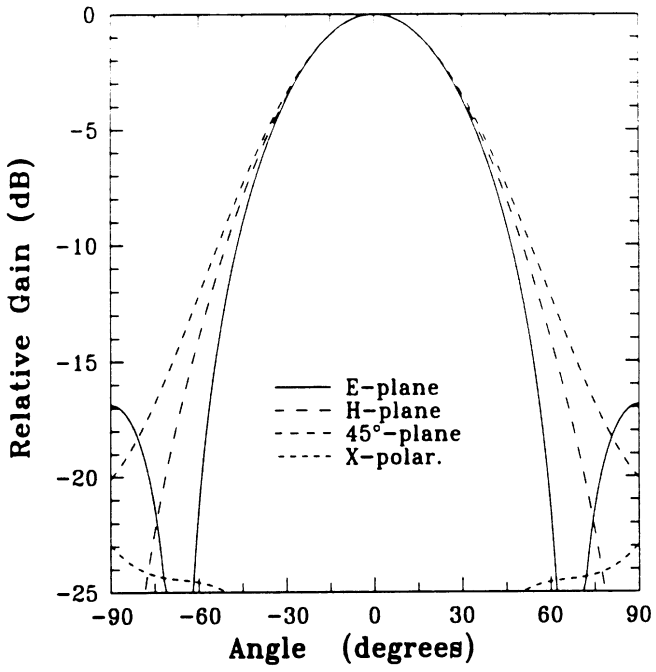


Figure 3.21: The radiation patterns of the double-slot antenna into a quartz ($\epsilon_r$=3.8) dielectric.

### 3.4.1 Theoretical Results

The computed E and H-plane power patterns and the phases of the electric field in the E-plane of a 13.7 mm diameter quartz ($\epsilon_r$ = 3.8) lens fed by a double-slot antenna at 246 GHz are shown for extension lengths of 3000 $\mu$m, 3800 $\mu$m, 4200 $\mu$m, 4800 $\mu$m, 5400 $\mu$m, 6000 $\mu$m, 6600 $\mu$m, and 7200 $\mu$m (Fig. 3.22). It is seen that the patterns become progressively narrower resulting in a higher directivity up to 6000 $\mu$m and then the mainlobe widens and the sidelobe levels begin to increase. The phase of the field is not constant in the mainlobe except around the synthesized elliptical position (6380 $\mu$m). This is seen on the 6000 $\mu$m plot where the phase is nearly constant in the mainlobe and then shifts 180° in the first sidelobe. The corresponding

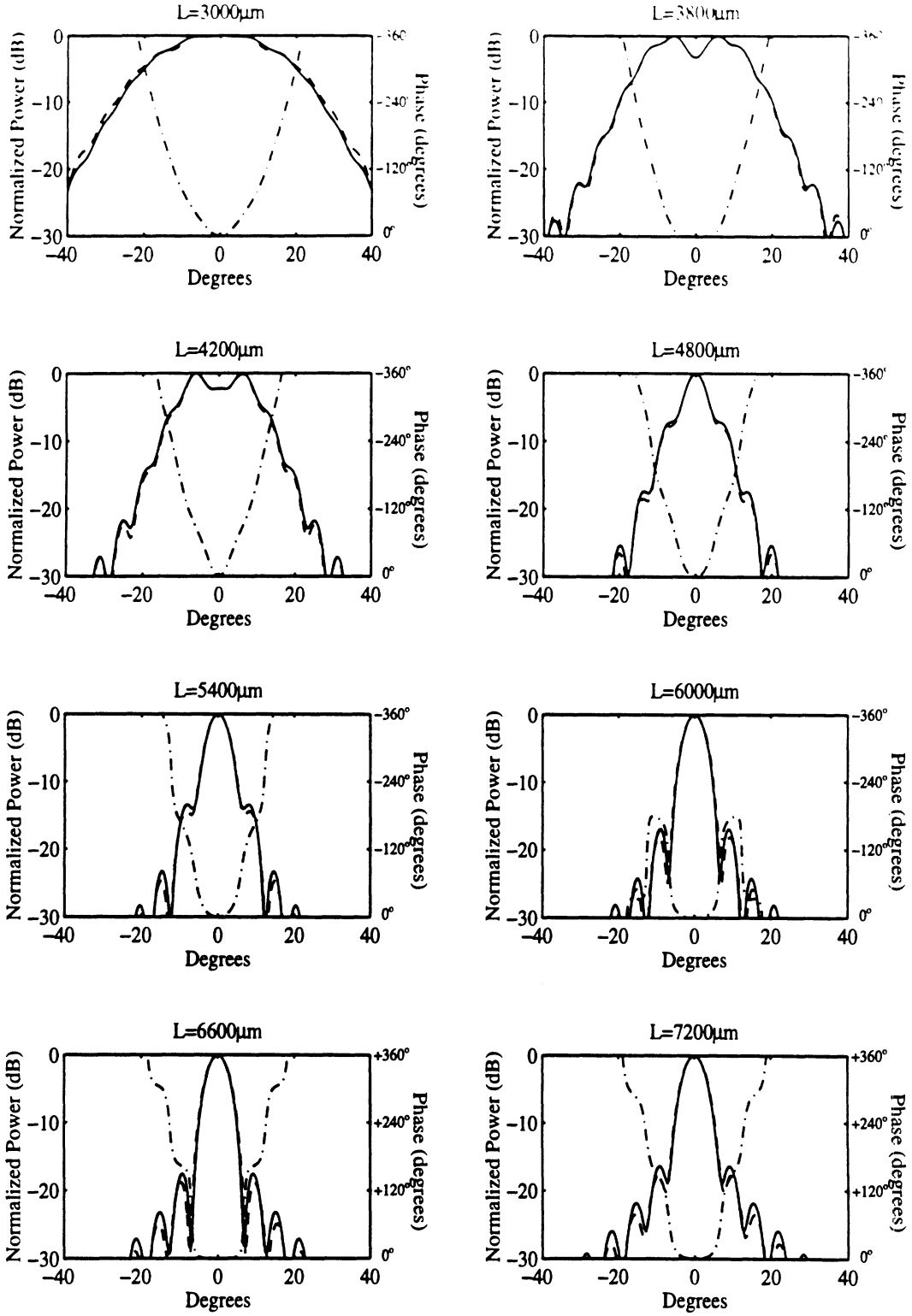


Figure 3.22: E and H-Plane power patterns and phase in the E-plane at 246 GHz for extension lengths of 3000 $\mu$m, 3800 $\mu$m, 4200 $\mu$m, 4800 $\mu$m, 5400 $\mu$m, 6000 $\mu$m, 6600 $\mu$m, and 7200 $\mu$m ($\epsilon_r$=3.8). The ($- \cdot - \cdot -$) line corresponds to the phase.

peak directivity and the Gaussicity as a function of the extension length is shown in Figure 3.23. The directivity has a broad peak of 30.3 dB centered at 6000 $\mu$m (L/R=0.87) and remains within 0.5 dB of the peak between 5500 $\mu$m (L/R=0.80) and 6900 $\mu$m (L/R=1.01). The corresponding aperture efficiency (coupling to a plane wave) peaks at 86%. It is seen that the Gaussicity is above 92% up to 4600 $\mu$m (L/R=0.67) and drops to 84-82% at the peak directivity and synthesized elliptical positions.

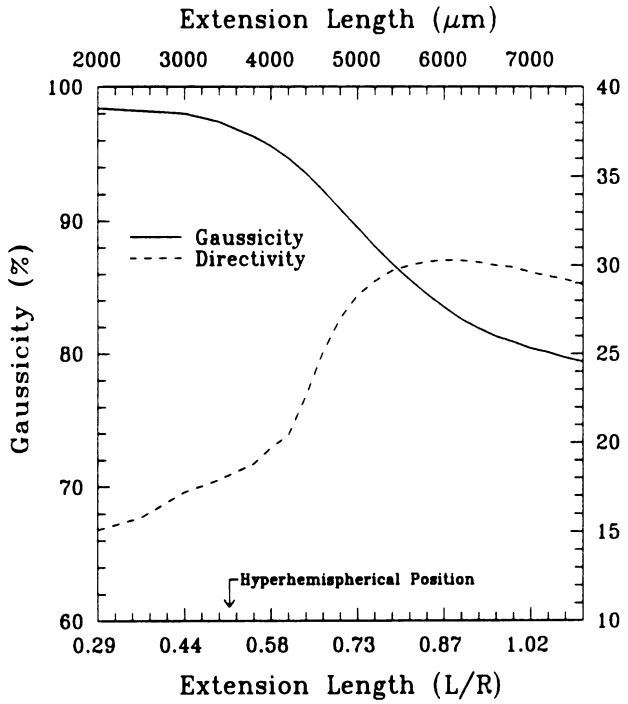


Figure 3.23: Directivity and maximum Gaussicity (pattern coupling efficiency) as a function of extension length at 246 GHz ($\epsilon_r$=3.8).

An analysis of a 13.7 mm diameter fused quartz lens was also performed at 100 GHz and 500 GHz, assuming the same radiation patterns of the feed antenna. Figure 3.24 shows the patterns and phases for extension lengths of 3000 $\mu$m, 3800 $\mu$m, 4200 $\mu$m, 4800 $\mu$m, 5400 $\mu$m, 6000 $\mu$m, 6600 $\mu$m, and 7200 $\mu$m at 500 GHz. The peak directivity (not the directivity at boresight) and Gaussicity calculations at 100 GHz, 246 GHz and 500 GHz are shown in Figure 3.25. It is important to note that the

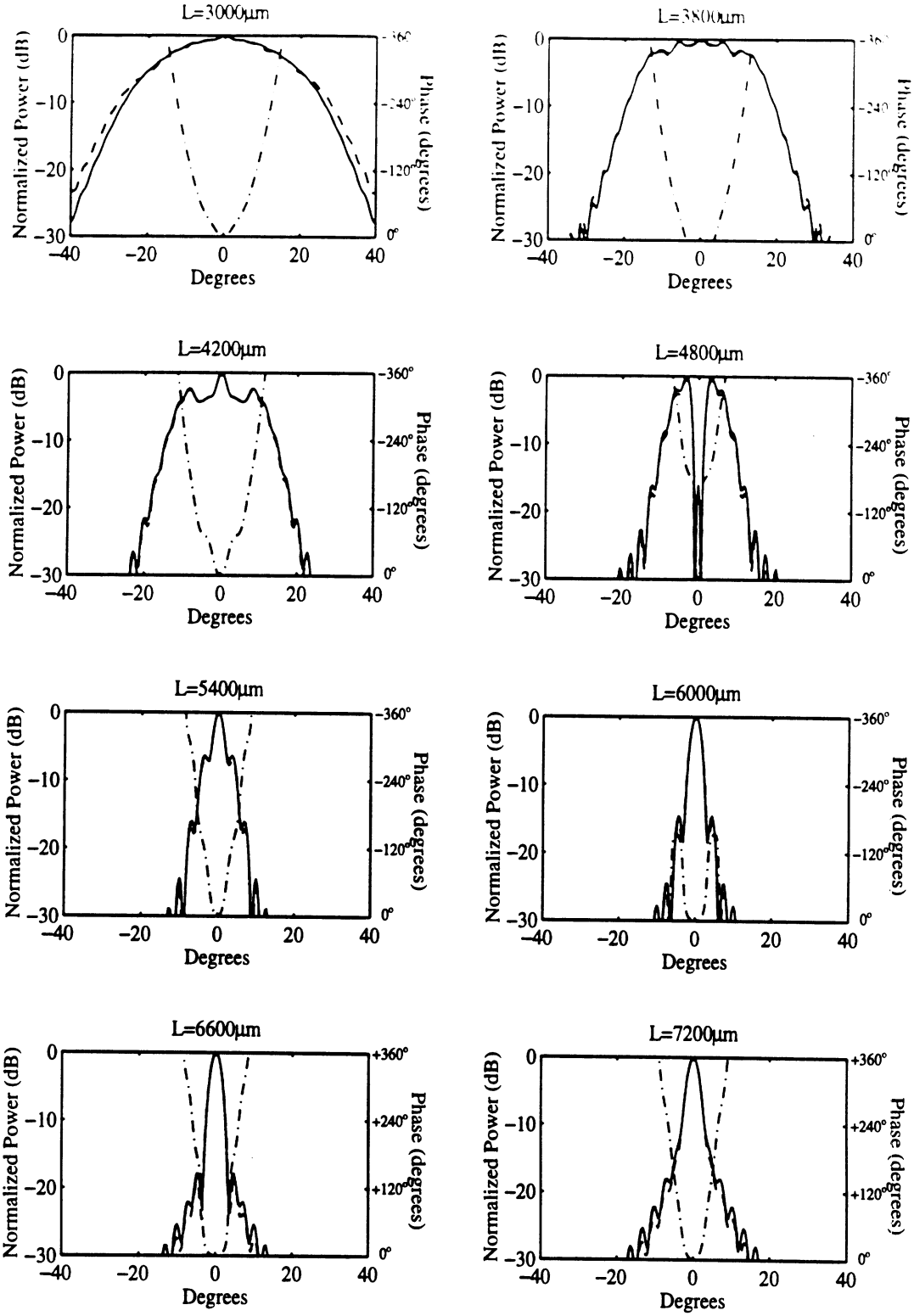


Figure 3.24: E and H-Plane power patterns and phase in the E-plane at 500 GHz for extension lengths of 3000 $\mu$m, 3800 $\mu$m, 4200 $\mu$m, 4800 $\mu$m, 5400 $\mu$m, 6000 $\mu$m, 6600 $\mu$m, and 7200 $\mu$m ($\epsilon_r$=3.8). The ($- \cdot - \cdot -$) line corresponds to the phase.

500 GHz patterns at positions of 4200 $\mu$m (L/R=0.61) and 4800 $\mu$m (L/R=0.70) do yield a high Gaussicity. This is counter-intuitive, especially at 4800 $\mu$m (L/R=0.70) where a dip of -20 dB exists at $\theta = 0$. The reason for the high Gaussicity is that the phase is quadratic and that there is very little power in a pattern around $\theta = 0$ (per steradian). The quadratic phase matches well to a converging Gaussian-beam. Patterns with dips and peaks around $\theta = 0$ have been judged before by researchers to be "quite bad". This example shows that *both* the amplitude and the phase of the far-field pattern are important to completely judge a pattern and its coupling efficiency to Gaussian-beams. At 100 GHz, the peak in the directivity curve occurs at 5600 $\mu$m (L/R=0.82) and is very broad. The corresponding Gaussicity is very smooth with a drop of 9% at 5600 $\mu$m and 12% at the synthesized elliptical position. On the other hand, at 500 GHz, the directivity curve shows a distinct peak of 36.2 dB centered at 6200 $\mu$m (L/R=0.90), with a corresponding aperture efficiency of 81%. Note that at higher frequencies, the peak directivity is closer to the synthesized elliptical position, which is the result of the geometrical optics approximation becoming more accurate. The Gaussicity peaks at 500 GHz at the hyperhemispherical position (3520 $\mu$m) with a value of 97% and drops to 76% at the 6200-6400 $\mu$m position. Again, as the frequency increases, the ray-optics approximation becomes more valid, and this explains the peak in Gaussicity at the hyperhemispherical position.

The near-field waist and radius of curvature are found from an inverse Fourier transform of the far-field Gaussian-beam [28] (Fig. 3.26), and are referenced to the aperture at the tip of the lens (Fig. 3.2). As expected, the radius of curvature is infinity at the synthesized elliptical position (6380 $\mu$m) and changes sign immediately afterwards. This means that the synthesized elliptical lens is a good approximation to a true elliptical lens and couples best to a Gaussian-beam at its minimum

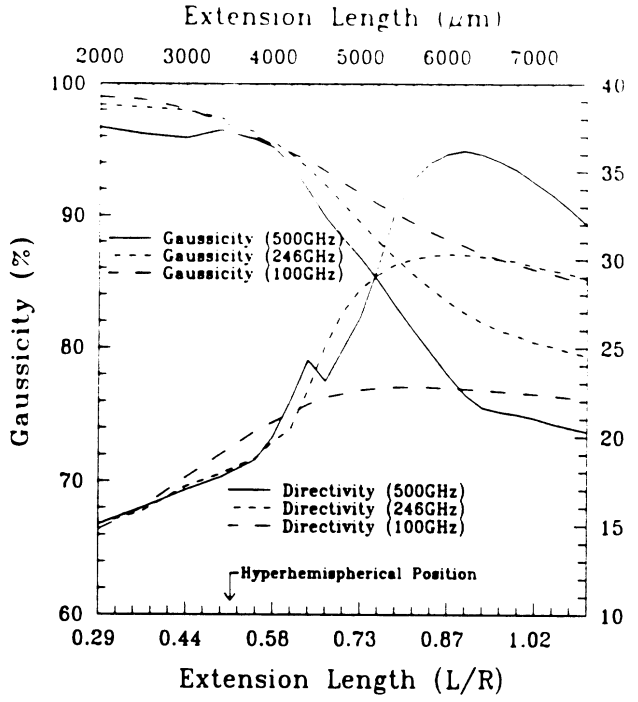


Figure 3.25: Directivity and maximum Gaussicity (pattern coupling efficiency) as a function of extension length at 100 GHz, 246 GHz, and 500 GHz ($\epsilon_r$=3.8).

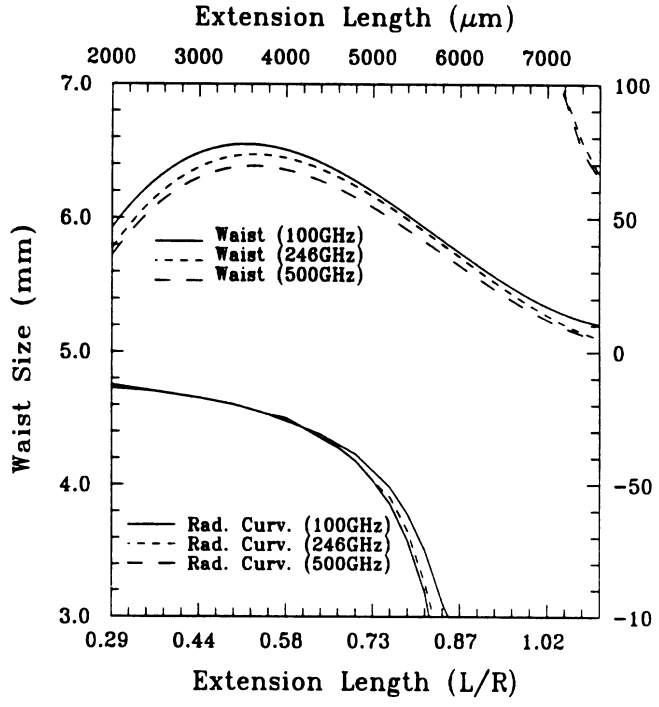


Figure 3.26: Waist and radius of curvature as a function of extension length at 100 GHz, 246 GHz, and 500 GHz ($\epsilon_r$=3.8).

waist. As expected, the Gaussian-beam radius of curvature approaches the lens radius (6.858 mm) when the extension length is small. The beam waist is nearly constant at 6.1±0.4 mm for extension lengths between 2000$\mu$m (L/R=0.29) and 6000 $\mu$m (L/R=0.87) for 100 GHz, 246 GHz, and 500 GHz. It is mainly the radius of curvature that is changing from -12 mm to -$\infty$ between 2000 $\mu$m and 6380 $\mu$m for all three frequencies. Therefore, the converging Gaussian-beam must be very well characterized on the lens aperture for optimal Gaussian-coupling efficiency.

The directivity and Gaussicity are calculated for a true elliptical lens using the same approach as for the extended hemispherical lens at 246 GHz. The true elliptical lens is defined such that the minor axis (perpendicular to boresight) is equal to the radius of the extended hemispherical lens, so that the effective area on the aperture plane is the same for both lenses. The E and H-plane mainlobes are slightly narrower than those of the synthesized elliptical lens and have 0.5 dB higher sidelobes. The directivity is 30.7 dB which is 0.5 dB higher than the synthesized ellipse. The elliptical lens Gaussicity is 83% and is independent of frequency. The corresponding minimum waist at the aperture plane is 5.7 mm, which is 0.2 mm more than that of the synthesized elliptical position.

### 3.4.2 Reflection Loss Calculations

The ray-tracing technique presented earlier also results in a full characterization of the reflection loss at the lens-air interface as a function of the extension length (Fig. 3.27). At low extension lengths or for high directivity feed antennas, the calculated loss is 0.5 dB which is the same as that predicted from simple transmission-line theory, $[(n-1)/(n+1)]^2$, where n is the index of refraction of the fused quartz lens. For a double-slot antenna, with a directivity of 11.2 dB, the loss increases to 2.7-3.2

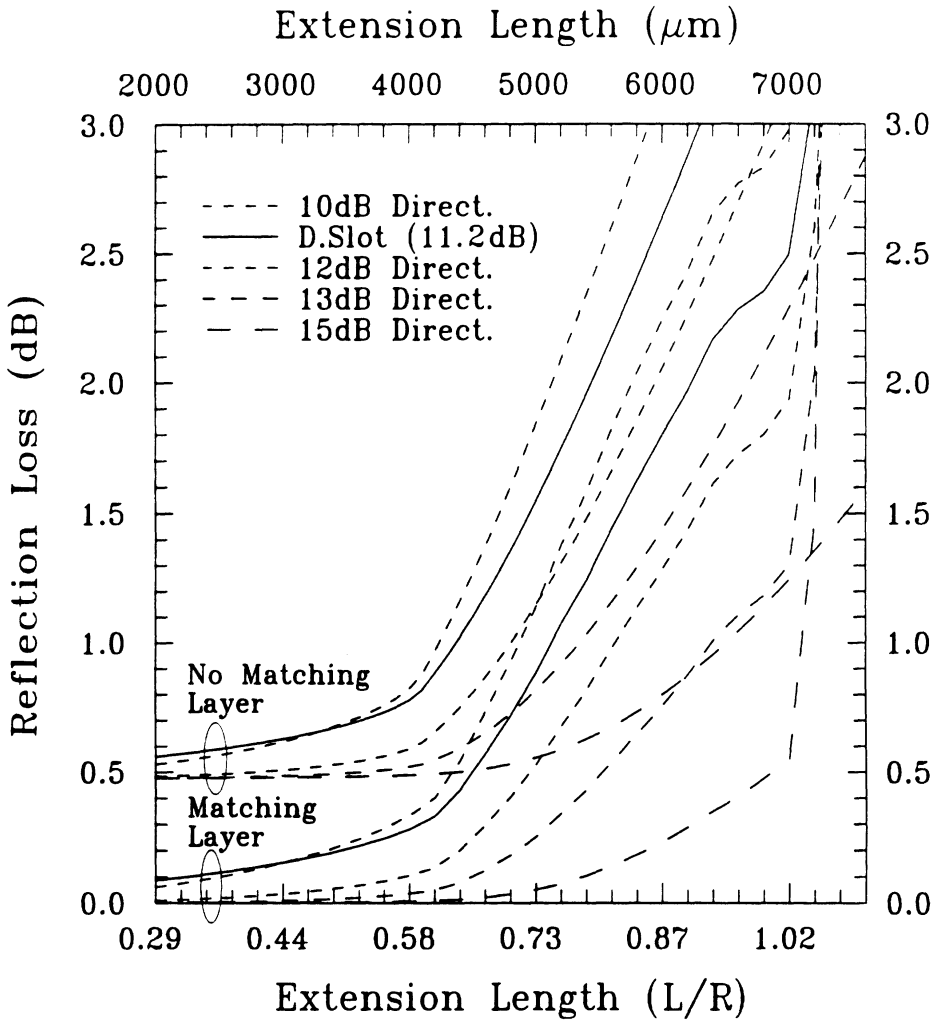


Figure 3.27: Reflection loss of a quartz lens at the lens/air interface as a function of the extension length for different feed antenna directivities: (a) without a matching layer and (b) with a $\lambda_m/4$ matching cap layer.

dB at the peak-position and synthesized elliptical position. This is due to the unfocused power lost in the rectangular extension section and from the total internal reflection of wide angle rays (above 57°). This is a considerable amount of reflected power which will appear in the sidelobe structure and the back-side power pattern of the extended hemispherical lens antenna. This power is assumed in this paper as a total loss in terms of Gaussian-coupling efficiency. The power lost to the rectangular extension section is considerable for extension lengths near the synthesized elliptical position. This presents a serious limitation for using low index of refraction lenses which require long extension lengths. On the other hand, a quartz elliptical lens has a reflection loss of only 0.65 dB, since the whole surface of the lens is properly curved.

The Gaussian-coupling efficiency of the extended hemispherical system must be multiplied by the reflection loss to result in a complete characterization of the system. Note that for feed antennas with greater than 13 dB directivity, the reflection loss does not increase as much since most of the radiated power of the feed antenna is near normal incidence to the lens. The directivities of spiral and log-periodic antennas on a quartz dielectric and backed by a ground-plane reflector are not known but are expected to be between 12 dB and 13 dB. The directivity of a double-dipole antenna inside the dielectric (as presented by Skalare [76] is also around 12 dB. Therefore, these three antennas present a lower reflection loss at the quartz-air interface at large extension lengths. This is very important at high frequencies (above 500 GHz) where it is difficult to manufacture an accurate matching layer for the quartz lens. For a quartz elliptical lens, the reflection losses decrease to less than 0.48 dB for antenna directivities greater than 13 dB.

Figure 3.27 also includes the reflection loss using a uniformly thick $\lambda_m/4$

matching cap layer with dielectric constant equal to $\sqrt{\epsilon_{lens}}$. The reflection loss for the double-slot antenna (directivity=11.2 dB) is 0.2 dB at the hyperhemispherical position, and increases to 2.2 dB at the synthesized elliptical position. Again, this is primarily due to power lost in the rectangular extension section. The radiation patterns and the directivities remain essentially the same with the matching cap layer. As expected, the reflection loss for the higher directivity antennas (12-15 dB) are lower (Fig. 3.27). No attempt is made here to design an optimum matching layer by varying the thickness of the matching dielectric across the surface of the lens. It is expected that an elliptical lens with a $\lambda_m/4$ matching layer will result in a reflection loss of less than 0.2 dB for all antenna directivities (11-15 dB).

### 3.4.3 Gaussicity vs. Frequency

A comparison of the directivity and Gaussicity for the true elliptical lens, the synthesized elliptical lens, and an extended hemispherical lens at peak directivity position for 100 GHz-1 THz is shown in Fig. 3.28. The true elliptical lens has a constant Gaussicity of 83% and a quadratic increase in the directivity, as expected from ray-optics calculations. The directivity of the synthesized elliptical lens shows a 1.7 dB drop at 1 THz compared to the elliptical lens due to the residual phase error on the planar aperture. Similarly, the Gaussicity drops to 70% at 1 THz due to the same effect. The directivities at extension lengths resulting in peak directivity ($L_{pk}$) for 100 GHz, 246 GHz, 500 GHz, 800 GHz, and 1 THz are also presented in Figure 3.28. Figure 3.29 shows that $L_{pk}$ asymptotically approaches the synthesized elliptical position with increasing radius/wavelength (or increasing frequency for a constant radius). The directivity at $L_{pk}$ is always slightly higher (0.1-0.2 dB) than the synthesized elliptical directivity and shows a 1.5 dB drop at 1 THz from the

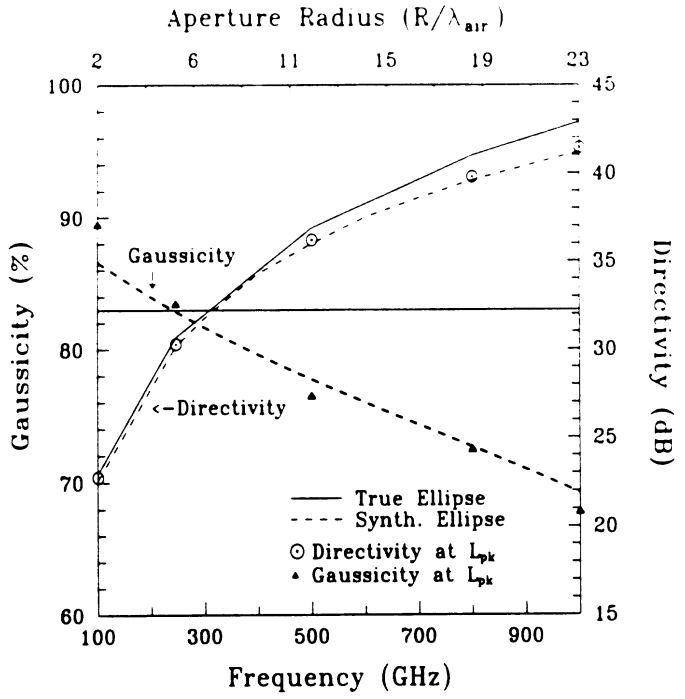


Figure 3.28: Directivity and maximum Gaussicity (pattern coupling efficiency) for a quartz lens as a function of frequency (or lens radius) for a true elliptical lens, a synthesized elliptical lens, and an extended hemispherical lens at peak directivity position ($L_{pk}$).

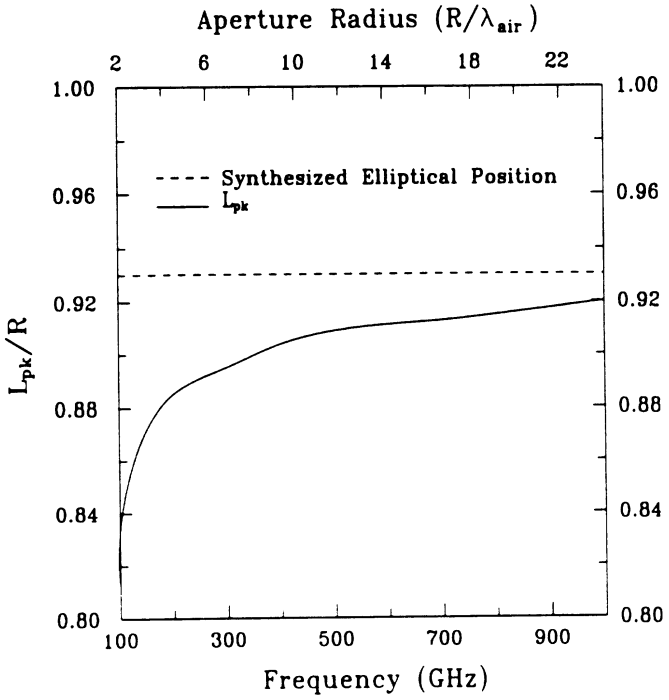


Figure 3.29: Extension length for peak directivity versus frequency (or $R/\lambda$) ($\epsilon_r$=3.8).

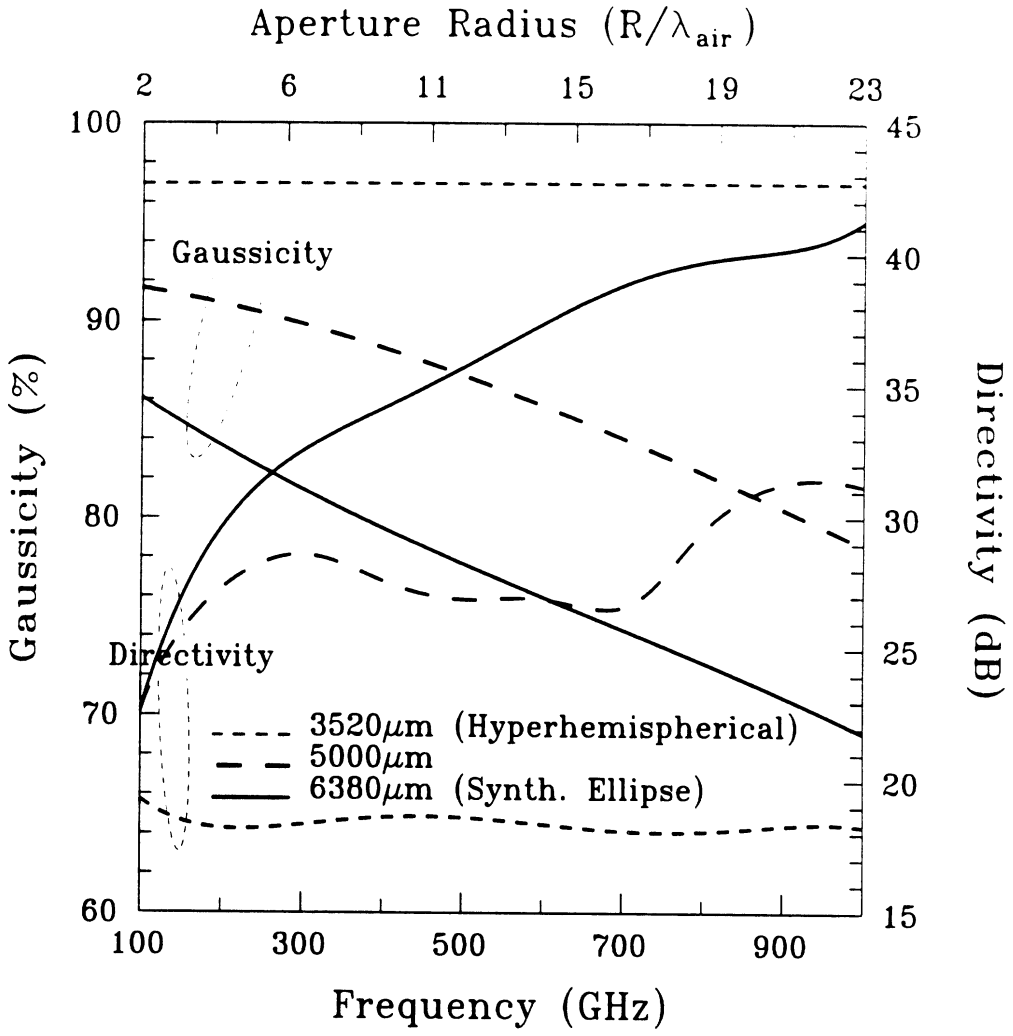


Figure 3.30: Directivity and Gaussicity (pattern coupling efficiency) as a function of frequency (or lens radius) for an extended hemispherical lens at L=3520 $\mu$m, 5000 $\mu$m, and 6380 $\mu$m ($\epsilon_r$=3.8).

true elliptical lens. The Gaussicities at $L_{pk}$ are the same as those of the synthesized elliptical position, except at 100 GHz, where the peak directivity position is closer to the hyperhemispherical position.

The Gaussicity and directivity for extension lengths of 3520 $\mu$m (hyperhemispherical), 5000 $\mu$m (an intermediate position), and 6380 $\mu$m (synthesized ellipse) are shown in Figure 3.30. The hyperhemispherical lens results in a nearly constant directivity of 18 dB and Gaussicity of 97%. Notice that the directivity is constant with frequency due to the constant $n^2$ magnification of the hyperhemispherical lens. The Gaussicity at 5000 $\mu$m is slightly lower than the hyperhemispherical lens and the directivity increases to around 30 dB at high frequencies. The Gaussicity at 6380 $\mu$m (close to the synthesized elliptical position) is the lowest of all three positions, but results in the largest directivity. The Gaussicity at the synthesized elliptical position (and at $L_{pk}$) drops to 70% at 1 THz while the Gaussicity for the 5000 $\mu$m position drops to 80% at the same frequency. The hyperhemispherical position shows the highest theoretical Gaussicity. However, it is hard to experimentally achieve this efficiency at the hyperhemispherical position due to the difficulty in aligning to the strongly converging beams needed at the aperture of the lens [28]. Thus the region between 4200 $\mu$m and 5200 $\mu$m (L/R=0.61 to 0.76) results in the best compromise between alignment, directivity and Gaussian-coupling efficiency.

## 3.5 Discussion

In this chapter, a ray-optics/field-integration approach has been used to fully characterize an extended hemispherical lens system with a double-slot antenna feed. The theoretical results were presented in extension length/radius (L/R) and radius/$\lambda$ (R/$\lambda$) and therefore result in universal design curves for silicon and quartz lenses of

different diameters and at different frequencies. The theoretical results are equally valid for slot-ring, double-dipole, log-periodic and spiral antennas. The only constraint is that the planar feed antenna produces a nearly circularly symmetrical beam into the dielectric lens. Also presented was a geometrical technique for synthesizing an elliptical lens from an extended hemispherical lens.

The results show that the directivity is strongly dependent on the extension length (especially at high frequencies). The results also show that the Gaussicity of an extended hemispherical lens is very high up to an intermediate position between the hyperhemispherical and synthesized elliptical lengths, and then begins to drop gradually.

The question arises over what extension length to choose for the best possible performance. The answer, according to the calculations, depends on the specific application (for example, a single unit or a unit in an imaging array). For *single units*, the hyperhemispherical position is not the best place since it results in a low directivity, and requires small $f/\#$ systems that are difficult to align. This was well demonstrated by our quasi-optical experiment and we found that it was very difficult to choose the position of the lenses for best Gaussian-coupling efficiency at the 1700 $\mu$m extension length. One should therefore use an extension length that results in an acceptably high directivity and therefore a large $f/\#$ for the objective lens. This also yields an easy-to-align quasi-optical system. However, the high directivity is achieved at the expense of a reduction in the Gaussian-coupling efficiency. Therefore, a suitable compromise between the increase in directivity and the decrease in Gaussian-coupling efficiency is achieved at an position intermediate between the hyperhemispherical and synthesized elliptical lengths. A summary of the optimum values for silicon and quartz lenses is now presented:

Silicon Lens:

The calculated Gaussicity (pattern coupling efficiency) is very high up to approximately 2200 $\mu$m and then drops gradually by about 10-15% at the synthesized elliptical position (depending on frequency). The corresponding beam waist on the aperture-plane is nearly constant (5.6$\pm$0.3 mm) and the radius of curvature ranges from -13 mm to -$\infty$. Thus the incident Gaussian-beam should be well characterized on the planar aperture for optimum coupling efficiency. In fact, we have built a lens system with a 10 dB difference in directivity and still succeeded in achieving nearly the same Gaussian-coupling efficiency for the low and high directivity systems. Our calculations also show that a 13.7 mm diameter silicon lens can be used up to about 1 THz without a significant drop in the Gaussian-coupling efficiency (maximum 20%) and has an associated directivity greater than 40 dB. The Gaussian-coupling efficiency for a double-slot antenna at a position between 2200 $\mu$m to 2400 $\mu$m (L/R= 0.32 to 0.35) is approximately 60-50%, which includes the reflection loss and the back-side power loss. This is expected to increase to about 90-80% when a matching cap layer is used.

For a 13.7 mm diameter silicon lens, we believe that a good compromise between the high directivity and the decrease in Gaussian-coupling efficiency is achieved at 2200-2400 $\mu$m extension length (L/R= 0.32 to 0.35). The corresponding Gaussicity is very high being always above 90% for frequencies below 1 THz. This was well demonstrated in our experimental setup at 246 GHz where the 2200 $\mu$m positions resulted in a 7% and 18% higher coupling efficiency than either the 1700 $\mu$m or 2700 $\mu$m positions, respectively.

Quartz Lens:

Our calculations also show that a 13.7 mm diameter fused quartz lens at the

synthesized elliptical position can be used up to about 1 THz (or R/λ=2.3) with an associated directivity greater than 40 dB, but with a drop in the Gaussicity to 70%.

We believe that a good compromise between the increase in directivity and the decrease in Gaussian-coupling efficiency for a fused quartz lens is achieved at 4200-5200 $\mu$m extension length (L/R= 0.61 to 0.76). The corresponding Gaussicity is very high being always above 80% for frequencies below 1 THz. Also, the corresponding dielectric reflection loss with a matching-cap layer is acceptable (0.3-1.0 dB). The Gaussian-coupling efficiency for a double-slot antenna at a position between 4200 $\mu$m to 5200 $\mu$m (L/R= 0.61 to 0.76) is 55-40%, which includes the reflection loss (1.8-2.2 dB) and the back-side power loss (28%). This is expected to increase to 60-50% when a matching cap layer is used. The Gaussian-coupling efficiency for double-dipole and spiral antennas is expected to be higher than double-slot antennas due to the absence of power loss to the air-side and lower reflection loss at the lens-air interface (see Fig. 3.27).

As seen from our calculations, double-slot antennas on quartz dielectrics suffer from two major loss factors. One is the power loss to the air side (28%), which can be eliminated with the use of a double-dipole, spiral, or log-periodic antenna and a back reflector. The other is the high reflection loss at larger extension lengths ($L_{pk}$ or synthesized elliptical positions). The reflection loss calculations in Fig. 3.27 are also applicable to double-dipole, spiral, and log-periodic antennas, and may not be as high as the double-slot antenna. The only way to eliminate the reflection losses is through the use of a high dielectric constant lens (silicon, alumina, etc.) with short extension lengths.

Comparison between Silicon and Quartz Lenses

A summary of the silicon and quartz data is presented in Figure 3.28. In this

figure, the efficiencies are presented for the optimum extension lengths described earlier. The absorption losses are for a 13.7 mm diameter lens (as used in the experiments of sections 3.3.4), and the attenuation data is found in [2]. Note that in a cryogenic system, the absorption losses would be eliminated, increasing the coupling efficiency for both lenses by about 10%. As can be seen, without a $\lambda/4$ matching cap, the fused quartz and silicon lenses have nearly the same coupling efficiency to a Gaussian-beam (48-50%). However, with the addition of a $\lambda/4$ matching cap layer, the silicon lens clearly has an increased coupling efficiency (71%) over a quartz lens (54%) (or 80% for silicon and 59% for quartz in a cryogenic system). Therefore, for radioastronomical applications, where the coupling efficiency is critical for maximizing the signal received, a silicon lens would be the preferred dielectric lens of choice.

Other Dielectric Constant Lenses

Finally, it should be mentioned that any dielectric constant could be used to realize the extended hemispherical dielectric lens system. In particular, one material is noteworthy to mention: alumina ($\epsilon_r = 9.8$). Its high dielectric constant gives it nearly the same radiation properties as a silicon lens, although it is a bit more lossy [2], and therefore not optimum for radioastronomical applications. However, it is ideal for commercial applications, since it can be manufactured by a molding process and therefore inexpensively mass-produced.

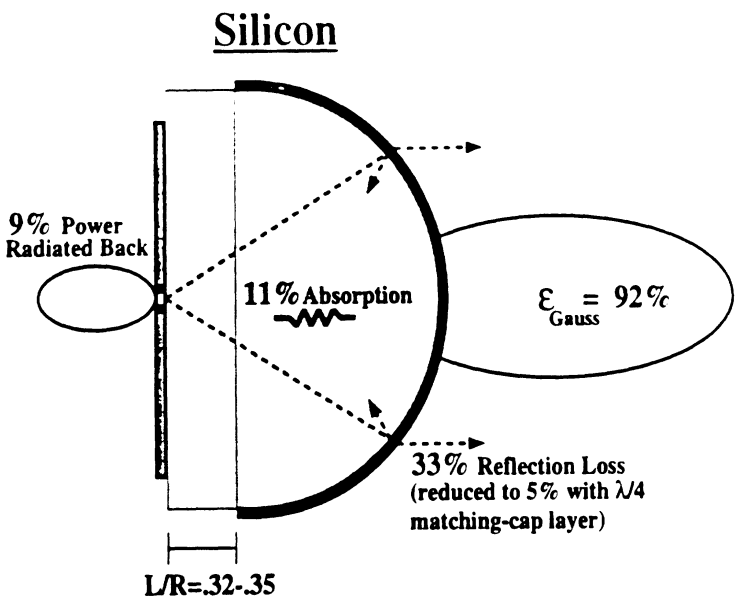


**Total Coupling Efficiency = ($\varepsilon_{\text{Back Loss}}$) ($\varepsilon_{\text{Absorption}}$) ($\varepsilon_{\text{Reflection}}$) ($\varepsilon_{\text{Gaussicity}}$)**
**No matching layer ≅ (1 - 0.09) (1 - 0.11) (1 - 0.33) (0.92) ≅ 50% (56% Cryogenic)**
**With matching layer ≅ (1 - 0.09) (1 - 0.11) (1 - 0.05) (0.92) ≅ 71% (80% Cryogenic)**

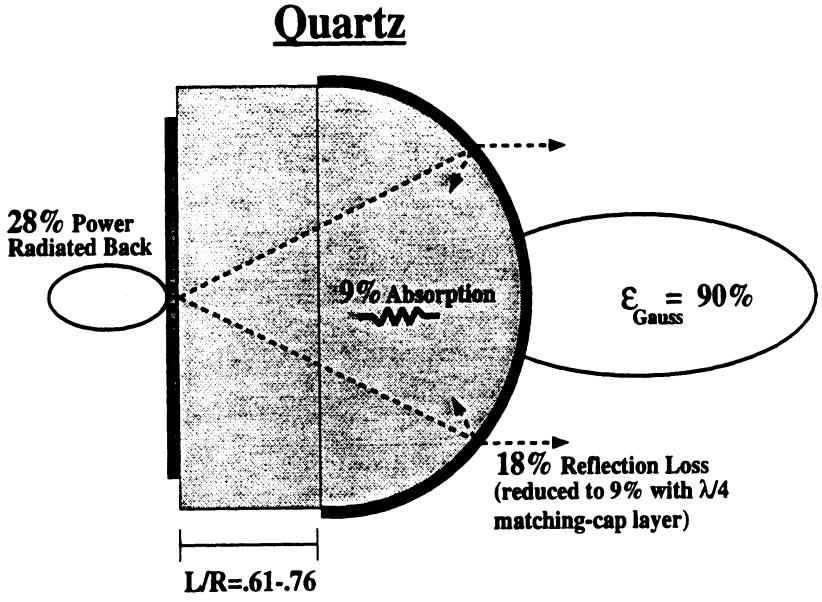


**Total Coupling Efficiency = ($\varepsilon_{\text{Back Loss}}$) ($\varepsilon_{\text{Absorption}}$) ($\varepsilon_{\text{Reflection}}$) ($\varepsilon_{\text{Gaussicity}}$)**
**No matching layer ≅ (1 - 0.28) (1 - 0.09) (1 - 0.18) (0.90) ≅ 48% (53% Cryogenic)**
**With matching layer ≅ (1 - 0.28) (1 - 0.09) (1 - 0.09) (0.90) ≅ 54% (59% Cryogenic)**

Figure 3.31: A breakdown of the losses for a silicon (top) and quartz (bottom) dielectric lens.

# CHAPTER IV

# OFF-AXIS PROPERTIES OF SILICON AND QUARTZ DIELECTRIC LENS ANTENNAS

In this chapter, the theoretical far-field patterns and Gaussian-beam coupling efficiencies are investigated for a double-slot antenna placed off-axis on extended hemispherical silicon and quartz lenses. Measured off-axis radiation patterns at 250 GHz agree well with the theory. Results are presented which show important parameters versus off-axis displacement: scan angle, directivity, Gaussicity, and reflection loss. Directivity contour plots are also presented and show that near diffraction-limited performance can be achieved at off-axis positions at non-elliptical extension lengths. Some design rules are discussed for imaging arrays on dielectric lens antennas.

## 4.1 Introduction

This chapter characterizes the off-axis performance of extended hemispherical dielectric lenses (Fig. 4.1). A ray-optics/field-integration formulation similar to that described in [28] is used to solve for the radiation patterns and Gaussian-coupling efficiencies. Briefly, the radiation of the feed antenna is ray-traced to find the fields immediately exterior to the lens surface. For a given ray, the fields are decomposed

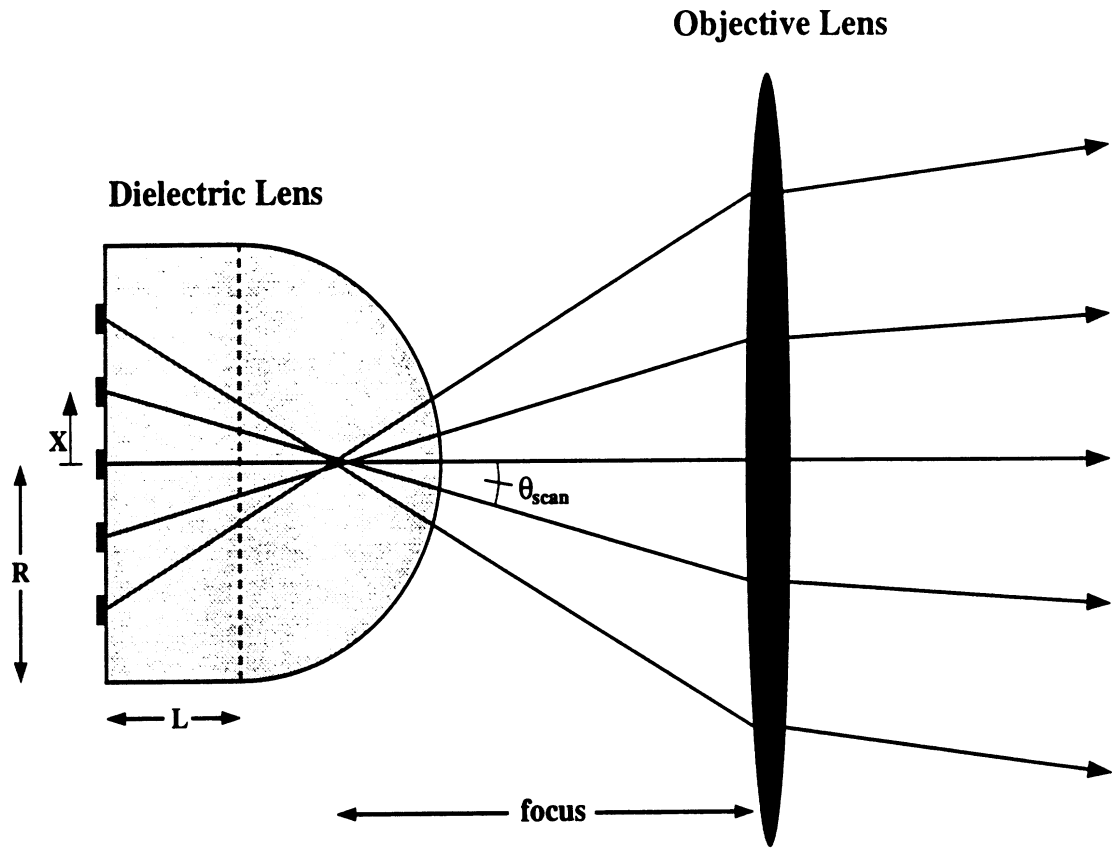


Figure 4.1: A linear imaging array on an extended hemispherical dielectric lens, coupled to an objective lens. The rays in this figure are not optically correct, and are only meant for illustrative purposes.

into TE/TM components at the lens-air interface, and the appropriate transmission formulas are used for each mode. The equivalent electric and magnetic currents are found directly from the fields, and a standard diffraction integral results in the far-field lens patterns [8]. This results in a general treatment that can find the far-field lens patterns for any extension length, displacement, and orientation of the feed antenna with respect to the center of the lens. The characteristics for differing positions of the feed antenna are similar, and this chapter considers displacements for two cases: an E-plane scan, in which the feed is displaced in the direction of the E-plane, and an H-plane scan, in which the feed is displaced in the direction of the H-plane.

In most applications the dielectric lens will be coupled with a quasi-optical system, and Figure 4.1 shows the dielectric lens coupled to an objective lens. If the Gaussian-beams emanating from the dielectric lens are well characterized, then one can easily trace through these beams through a quasi-optical system (see Section 3.3.5). Or, for greater accuracy, the patterns emanating from the dielectric lens could be used with EM ray-tracing techniques (as was done to calculate the dielectric lens patterns) to find the fields across the aperture of the objective lens, and then a Fourier transform will yield the far-field patterns from the objective lens/dielectric lens system.

## 4.2 Theoretical Calculations

All calculations are performed assuming a double-slot antenna as the feed antenna for the extended hemispherical dielectric lens. However, note that any antenna which illuminates the lens surface with a nearly symmetrical, equal-phase beam will produce similar results. The dimensions of the double-slot antenna are a length of

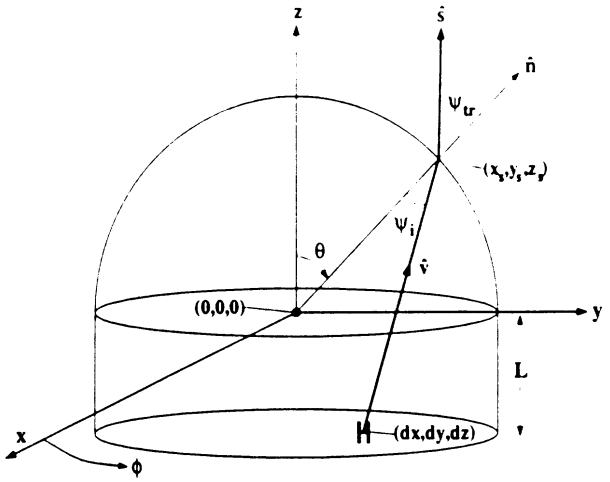


Figure 4.2: The geometry used for the off-axis theoretical computations.

$0.28\lambda_{air}$ and spacing of $0.16\lambda_{air}$ for a silicon lens ($\epsilon_r = 11.7$), and a length of $0.49\lambda_{air}$ and spacing of $0.28\lambda_{air}$ for a quartz lens ($\epsilon_r = 3.8$), which are the same designs used in Chapter 3 (see Fig. 3.2 and Fig. 3.21). These dimensions have been scaled according to the square root of the dielectric constant and yield nearly the same radiation patterns into the respective lenses. The double-slot antennas produce symmetrical patterns into the infinite dielectric half-space with a corresponding directivity of 11.2 dB and a cross-polarization level lower than -23 dB in the 45°-plane (the directivity quoted is calculated using the pattern radiated in the dielectric only). The radiation patterns are 98% Gaussian, and therefore the radiation patterns from the dielectric lens should also have a Gaussicity of 98% if no abberations are introduced. Note that the patterns radiated to the air-side are broader, and contain 9.0% of the total radiated power for a silcon lens, and 28.3% of the total radiated power for a quartz lens.

The theoretical technique for analyzing the lens radiation patterns is an expanded version of the electromagnetic ray-tracing technique presented in Section 3.2. The geometry of the problem is shown in Figure 4.2. First, define the surface normal

to be:

$$\hat{n} = \cos\theta\cos\phi\hat{x} + \cos\theta\sin\phi\hat{y} + \sin\theta\hat{z} \tag{4.1}$$

Define the ray path inside the lens to be:

$$\mathbf{v} = (x_s - dx)\hat{x} + (y_s - dy)\hat{y} + (z_s - dz)\hat{z} \tag{4.2}$$

$$\hat{v} = \mathbf{v}/|\mathbf{v}| \tag{4.3}$$

where $(x_s, y_s, z_s)$ are the surface coordinates and (dx,dy,dz) are the feed location coordinates. The basis vectors that defines the fields that lie in the perpendicular and parallel planes of incidence are:

$$\mathbf{P}_\perp = \hat{n} \times \hat{v} \tag{4.4}$$

$$\hat{P}_\perp = \mathbf{P}_\perp/|\mathbf{P}_\perp| \tag{4.5}$$

$$\hat{P}_{||} = \hat{P}_\perp \times \hat{v} \tag{4.6}$$

Then the perpendicular and parallel values of electric field inside the sphere are:

$$E_{\phi d} = \mathbf{E_d} \cdot \hat{P}_\perp \tag{4.7}$$

$$E_{\theta d} = \mathbf{E_d} \cdot \hat{P}_{||} \tag{4.8}$$

where $\mathbf{E_d}$ is the electric field on the lens surface *inside* the sphere, as found from equations 3.6 and 3.7. The electric field outside the sphere can then be derived to be:

$$E_x = E_{\phi d}T_\perp(\hat{x} \cdot \hat{P}_\perp) + E_{\theta d}T_{||}[(\hat{x} \cdot \hat{P}_{||})\cos(\psi_{tr} - \psi_i) - (\hat{x} \cdot \hat{v})\sin(\psi_{tr} - \psi_i)] \tag{4.9}$$

$$E_y = E_{\phi d}T_\perp(\hat{y} \cdot \hat{P}_\perp) + E_{\theta d}T_{||}[(\hat{y} \cdot \hat{P}_{||})\cos(\psi_{tr} - \psi_i) - (\hat{y} \cdot \hat{v})\sin(\psi_{tr} - \psi_i)] \tag{4.10}$$

$$E_z = E_{\phi d}T_\perp(\hat{z} \cdot \hat{P}_\perp) + E_{\theta d}T_{||}[(\hat{z} \cdot \hat{P}_{||})\cos(\psi_{tr} - \psi_i) - (\hat{z} \cdot \hat{v})\sin(\psi_{tr} - \psi_i)] \tag{4.11}$$

where $T_\perp$ and $T_{||}$ are the perpendicular and parallel transmission coefficients defined previously in equations 3.9 and 3.11, and $\psi_i$ and $\psi_{tr}$ are the angles of incidence and transmission. The ray path vector outside the lens can be found by:

$$s_x = v_x \cos(\psi_{tr} - \psi_i) + (\hat{x} \cdot \hat{P}_{||}) \sin(\psi_{tr} - \psi_i) \tag{4.12}$$

$$s_y = v_y \cos(\psi_{tr} - \psi_i) + (\hat{y} \cdot \hat{P}_{||}) \sin(\psi_{tr} - \psi_i) \tag{4.13}$$

$$s_z = v_z \cos(\psi_{tr} - \psi_i) + (\hat{z} \cdot \hat{P}_{||}) \sin(\psi_{tr} - \psi_i) \tag{4.14}$$

and therefore the magnetic field outside the sphere is simply:

$$\mathbf{H} = \hat{s} \times \mathbf{E} \tag{4.15}$$

As before, once the electric and magnetic fields have found just outside the sphere, the equivalent electric and magnetic current densities [8] are calculated using:

$$\mathbf{J} = \hat{n} \times \mathbf{H} \tag{4.16}$$

$$\mathbf{M} = \hat{n} \times \mathbf{E} \tag{4.17}$$

and equations 3.14-3.17 are used to find the far-field radiation patterns.

### 4.2.1 Scan Angle

The resulting scan angle for an off-axis displacement X/R (where X is the distance off-axis and R is the radius of the lens) is shown in Figure 4.3 at three different extension lengths L/R (where L is the extension length): hyperhemispherical, intermediate, and synthesized elliptical (diffraction-limited position), and for both silicon ($\epsilon_r = 11.7$) and quartz ($\epsilon_r = 3.8$) dielectric lenses. As expected, for a given X/R off-axis displacement, the silicon dielectric lens will have a larger scan angle than the quartz lens due to its higher dielectric constant. Note that the off-axis

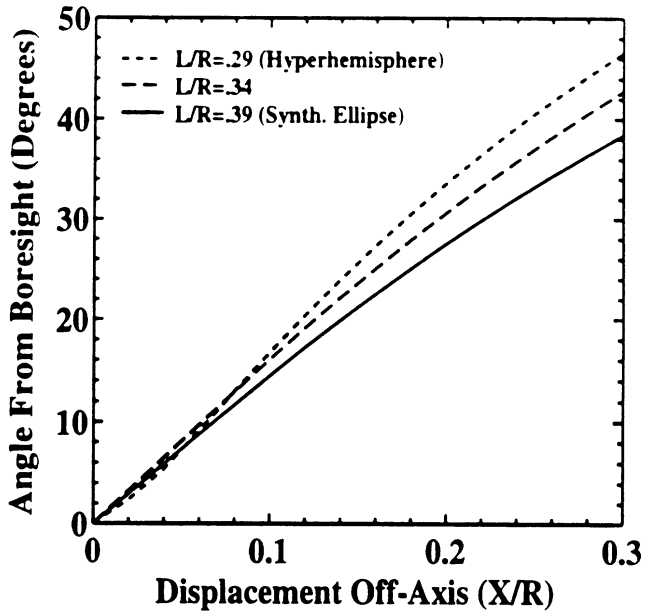


(a)

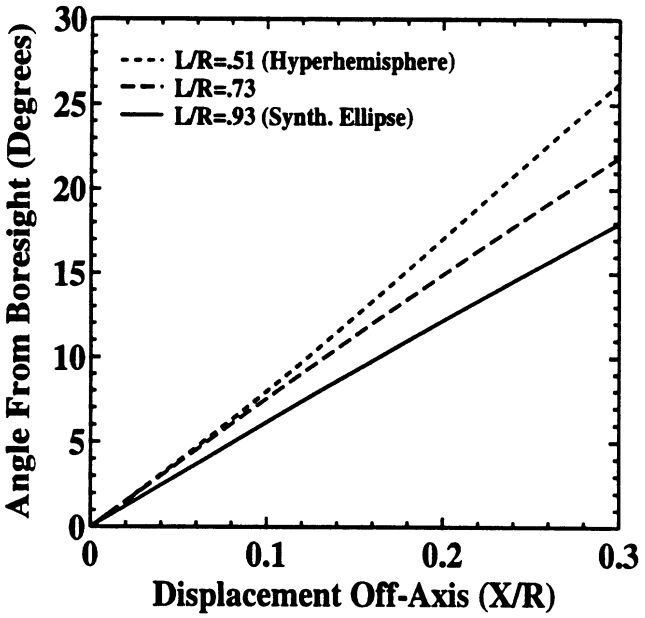


(b)

Figure 4.3: Scan angle versus off-axis displacement at fixed extension lengths for a silicon (a) and a quartz (b) lens.

positions are neither dependent on the lens size nor on the wavelengths away from the center, but on the percentage of the lens radius away from the center. Also, the scan angle is independent of the direction of the displacement (i.e. E or H-plane scan).

### 4.2.2 Directivity

The effect of an off-axis displacement (in the H-plane) on the radiation patterns at the hyperhemispherical position (L/R = 0.29) for a 12$\lambda$-diameter silicon lens is shown in Figure 4.4. In this plot, the z-axis has been re-oriented along the peak of the main beam, and the peak is always centered at $\theta$ = 0 degrees. It is interesting to see that the patterns become sharper and achieve a maximum directivity of 29.6 dB at X/R = 0.24. This indicates that the diffraction-limited performance can be nearly achieved by either increasing the extension length on-axis past the hyperhemispherical position, or by moving the feed antenna position off-axis in the hyperhemispherical plane. This can best be seen by the directivity contour plots for silicon and quartz extended hemispherical dielectric lenses in Figure 4.5. The contour plot for a quartz lens shows less variation in directivity off-axis since lower dielectric constants require longer extension lengths, and thus lessen the effect of off-axis displacements. Note that in the case of the silicon lens in the hyperhemispherical plane, moving off-axis does not achieve the full diffraction limited performance possible, as it is 1.2 dB lower than the maximum possible on-axis directivity of 30.8 dB at L/R = 0.38.

### 4.2.3 Gaussicity

Figure 4.6 shows the Gaussicity plots for a 24$\lambda$-diameter silicon and quartz lens. Two types of Gaussicity are presented. The first set of curves represent the

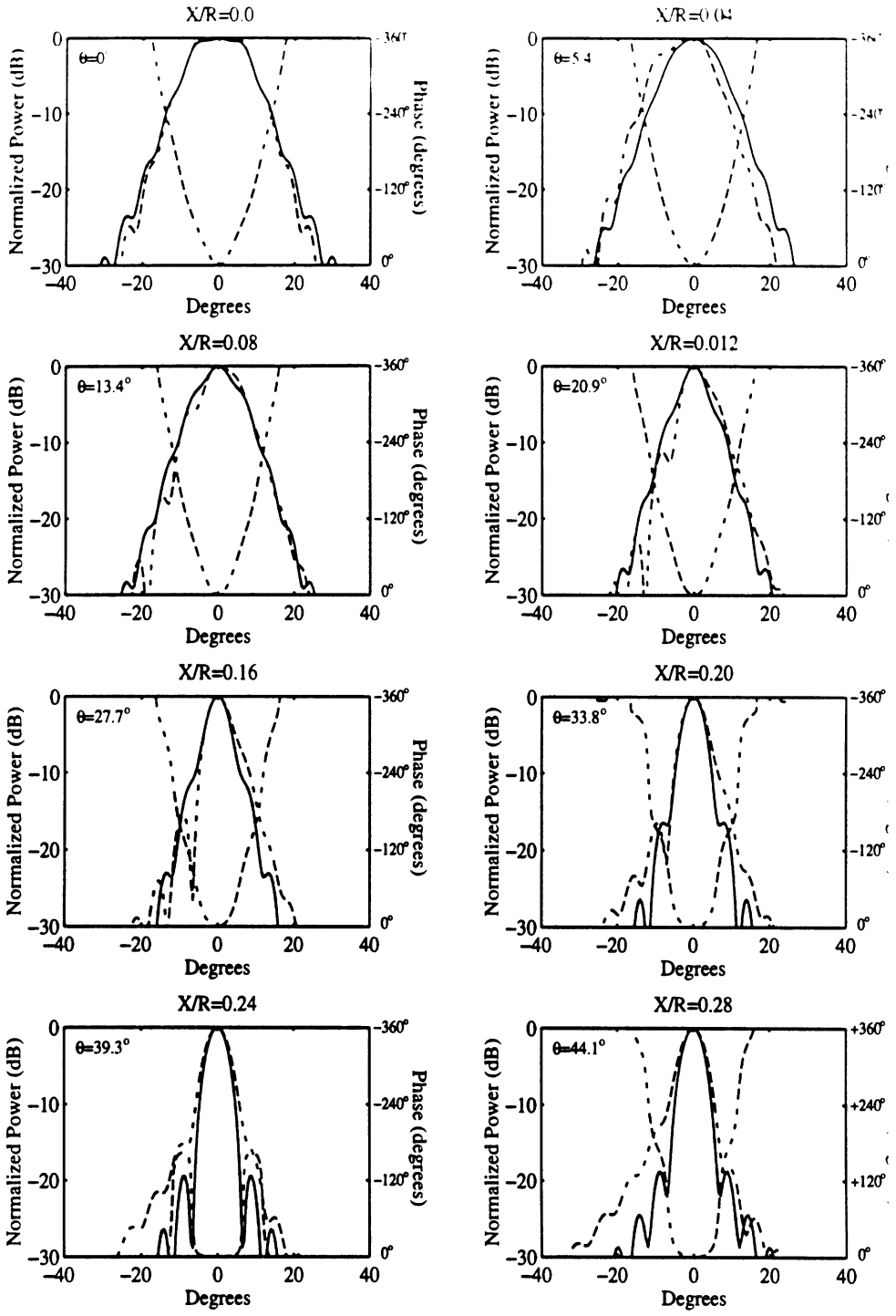


Figure 4.4: E and H-plane power patterns and H-plane phase for off-axis displacements in the H-plane at the hyperhemispherical extension length (L/R = 0.29) for a 12$\lambda$-diameter silicon lens. The dashed/dotted line corresponds to the phase.

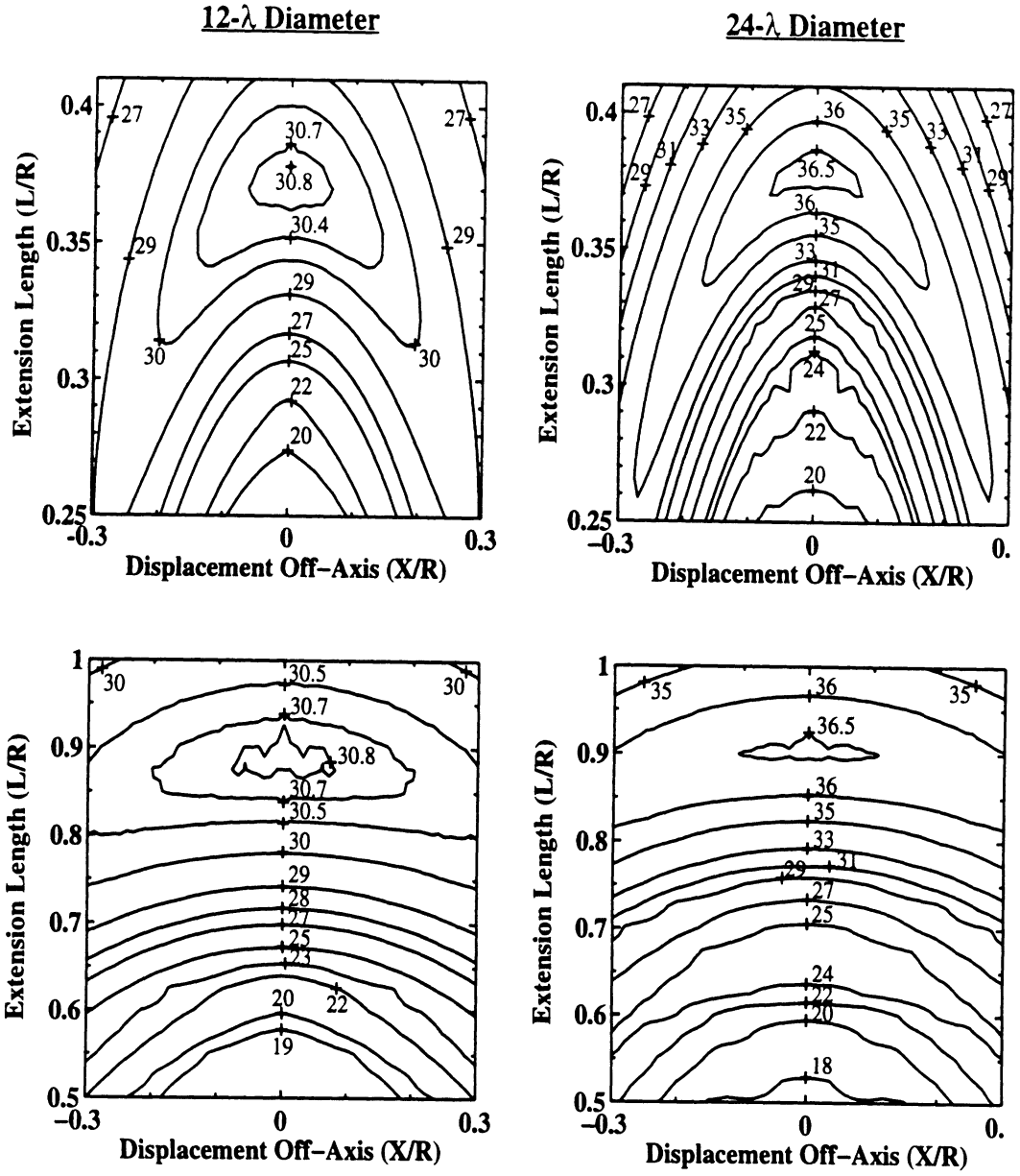


Figure 4.5: Directivity contour plots of silicon (top) and quartz (bottom) versus extension length and off-axis displacement, for a 12$\lambda$-diameter lens (left) and a 24$\lambda$-diameter lens (right).